

Charge Transfer between Semiconductor Nanocrystals and a Metal

Aboriginal Art,
Western Australia

Charge Transfer between Semiconductor Nanocrystals and a Metal

Ladingsoverdracht tussen Halfgeleider Nanokristallen en een Metaal

(met een samenvatting in het Nederlands)

PROEFSCHRIFT

ter verkrijging van de graad van doctor aan de Universiteit Utrecht op gezag van de Rector Magnificus, Prof. Dr. H.O. Voorma, ingevolge het besluit van het College voor Promoties in het openbaar te verdedigen op maandag 25 september 2000 des namiddags te 14:30 uur

door

Erik Petrus Antonius Maria Bakkers

geboren op 18 december 1972 te Kaatsheuvel

Promotor : Prof. Dr. J.J. Kelly
Co-promotor : Dr. D. Vanmaekelbergh

Faculteit Scheikunde, Universiteit Utrecht

Charge Transfer between a Semiconductor Quantum Dot and a Metal /

Erik Bakkers, Utrecht : Universiteit Utrecht, Faculteit Scheikunde, Debye Instituut

Proefschrift Universiteit Utrecht. Met een samenvatting in het Nederlands

ISBN 90-393-2451-4

Trefwoorden: Quantum Dots / Halfgeleiders / Foelectrochemie / Tunneling Spectroscopie

Contents

1	Semiconductor Quantum Dots	7
2	Excited State Dynamics in CdS Quantum Dots Adsorbed on a Metal Electrode	27
3	Time-Resolved Photoelectrochemistry with PbS Quantum Dots Adsorbed on Gold	49
4	Distance Dependent Electron Transfer in Gold/Spacer/Q-CdSe Assemblies	65
5	Scanning Tunneling Spectroscopy with Symmetrical and Asymmetrical Tip/Quantum Dot/Gold Configurations	83
6	Single Electron Tunneling through a CdSe Quantum Dot	99
	Samenvatting	115
	List of Publications	121
	Dankwoord	123
	Curriculum Vitae	125

Semiconductor Quantum Dots

This thesis deals with electron tunneling between semiconductor nanocrystals (quantum dots) and a metal. In this chapter, we discuss the confinement of the electron wave functions in a nanocrystal (size quantisation) and the basic principles of electron tunneling. The importance of surface atoms and the corresponding surface electron levels for the optical and electronic properties of quantum dots is discussed. To study their (opto)electronic properties we have attached the quantum dots to a conducting substrate. A metal electrode with a monolayer of semiconductor quantum dots has been investigated in a photoelectrochemical cell. Photoinduced electron tunneling between the nanocrystals and the metal electrode or a redox system in the electrolyte was investigated by a time-resolved photoelectrochemical technique (Intensity-Modulated Photocurrent Spectroscopy). Alternatively, the electronic properties of individual quantum dots were studied by Scanning Tunneling Spectroscopy. The principle of these two techniques is described.

1.1 Introduction

A crystalline material which is size-restricted in three dimensions such that the electron wave functions are confined within its volume is called a quantum dot (QD). Due to this confinement the electronic properties of quantum dots depend on their size in the nanometer regime.^{1,2} This effect, now called 'size-quantisation', was first observed in 1926 with CdS colloids³, but was only properly recognized in the 1980's.^{4,5} Chemists and physicists have studied nanostructures extensively in the past two decades in order to understand the size-quantisation effects in semiconducting and metal quantum dots.

Due to their extremely small sizes and their interesting electronic properties, quantum dots are promising building blocks for the fabrication of electronic and optoelectronic solid state devices. Integrated circuits (ICs) might be further miniaturised by using nanocrystallites. The II–VI nanocrystals have a bandgap which can be tuned in a broad range (up to 4 eV) by changing either their size or chemical composition; this makes them suitable candidates for applications as a Light Emitting Diode (LED)^{6,7}, a Single Electron Transistor (SET)⁸⁻¹⁰, chromophores in solar cells¹¹⁻¹⁵, or as a 'building block' for photonic crystals.¹⁶ Recently, a LED with an efficiency of 10 %, based on CdSe nanocrystals in a semiconducting polymer matrix, was fabricated.^{17,18} The output colour could be tuned in the entire visible range. A critical parameter for the performance of a SET, the principle of which is based on the Coulomb blockade effect, is the capacitance of the quantum dot, which is determined by its size. Quantum dots can be applied as stable fluorescent indicators in biological research; core-shell quantum structures of CdSe/ZnS have a very high luminescence quantum yield (up to 100%). Since they can easily be attached to DNA¹⁹ or proteins by a sulphide bond they can act as a luminescing label to monitor biological reactions. Semiconductor colloids can also be employed in photocatalysis; TiO₂ colloids irradiated with UV-light can photo-oxidize organic contaminants.²⁰

Methods for the preparation of large quantities of well-defined nanoparticles have been developed in order to study the size-quantisation effect. A technique to grow low-dimensional structures, Molecular Beam Epitaxy (MBE), was developed at the end of the 1960's.^{22,23} Arrays of quantum dots on substrates can be prepared by MBE or lithographic dry-etching.²⁴⁻²⁵ Alternatively, quantum dots can be formed in the gas phase by laser vaporisation²⁵ or as colloids in suspension.^{27,28} Chemists have succeeded in greatly improving the monodispersity in size and shape of colloidal semiconductor quantum dots in the past decade.²⁹ High-quality suspensions can now be synthesised and the size distribution can be further narrowed by size-selective precipitation or photoetching.³⁰⁻³²

Optical absorption and photoluminescence were first used to study the electronic structure of nanometer-sized semiconductor colloids. However, these techniques only provide information about the collective properties of large numbers of QDs and, due to a distribution in particle size, the luminescence signals are inhomogeneously broadened. With Scanning Probe Techniques such as Scanning Tunneling Spectroscopy (STM) and Scanning Near-field Optical Microscopy (SNOM), electrical and optical measurements on individual particles can be performed, avoiding problems arising from polydispersity.

In the work described in this thesis the optoelectronic properties of semiconductor quantum dots, and charge transfer between such structures and a conducting substrate were studied in a novel way. For this purpose, metal substrates were provided with a (sub)monolayer of quantum dots; the optoelectrical properties of the systems were investigated with time-resolved photoelectrochemistry. The electronic structure of individual nanocrystals was investigated by Scanning Tunneling Spectroscopy at room temperature and at 4 K. This chapter presents an introduction to the size-quantisation effect in semiconductors and electron transfer between a metal and a semiconductor quantum dot. In the latter sections the principles of the measuring techniques are explained and an outline of this thesis is given.

1.2 Size-quantisation in Semiconducting Nanocrystals

1.2.1 Energy Bands in Bulk Semiconductor Crystals

To discuss the origin of energy bands in bulk semiconductors and electron tunneling between two systems, a single electron in a crystal is considered.³³ The time-independent Schrödinger equation for an electron can be written as,

$$-\frac{\hbar^2}{2m_e} \nabla^2 \Psi(x, y, z) + U(x, y, z) \Psi(x, y, z) = E \Psi(x, y, z) \quad (1.1)$$

where m_e is the mass of the free electron, E is the kinetic energy, and $\nabla^2 = \left(\frac{\partial^2}{\partial x^2} + \frac{\partial^2}{\partial y^2} + \frac{\partial^2}{\partial z^2} \right)$. In the free-electron approach, the potential energy of the electron due to the crystal lattice of core ions $U(x, y, z)$ is neglected, and is taken as a constant (e.g. $U(x, y, z) = 0$). In that case the solution of equation (1.1) for $\Psi(x, y, z)$ can be denoted as,

$$\Psi_{\vec{k}}(\vec{r}) = \frac{1}{\sqrt{V}} e^{i\vec{k}\cdot\vec{r}} \quad (1.2)$$

where \vec{r} is the position vector (x, y, z) , and \vec{k} is the wave-vector (k_x, k_y, k_z) ; the plane periodic wave, $e^{i\vec{k}\cdot\vec{r}}$, has a constant amplitude in any plane perpendicular to \vec{k} , and is periodic along lines parallel to \vec{k} , with a wavelength $\lambda_e = \frac{2\pi}{k}$. The prefactor $\frac{1}{\sqrt{V}}$ is due to the normalisation condition, which requires that the particle must be present in the sample volume V . The linear momentum of the electrons is $\vec{p} = \hbar\vec{k}$ and the kinetic energy is given by,

$$E(\vec{k}) = \frac{\hbar^2 k^2}{2m_e} \quad (1.3)$$

The occupation of the electron levels is in accordance with the Pauli exclusion principle. At 0 K, all energy levels below the Fermi-energy (E_F) are occupied by two electrons of opposite spin. The occupation of electron energy levels under thermal equilibrium at $T > 0$ K can be derived from statistical thermodynamics. The probability that an energy level, E , is occupied by an electron is given by the Fermi-Dirac function,

$$f(E) = \frac{1}{1 + e^{(E - \mu_e)/k_B T}} \quad (1.4)$$

in which μ_e is the electrochemical potential (Fermi-level) and k_B the Boltzmann constant. The free electron model can be refined by taking the scattering of the electron waves by the periodic lattice potential energy $U(x, y, z)$ into account. The distance between the centres of the core ions in the x-direction is denoted as d_x . The electrons with low energy have wavelengths much longer than d_x ; however, at higher energy there are free electrons with wavelengths obeying the condition for Bragg reflection,

$$\frac{\lambda_e}{2} \cong \frac{d_x}{q} \quad (q = \pm 1, \pm 2, \dots) \quad (1.5)$$

Due to Bragg scattering on the periodic lattice potential, propagation of these electrons will be prohibited in the x-direction and standing waves are formed. Two standing waves can be constructed by a linear combination of the waves travelling in the positive and negative

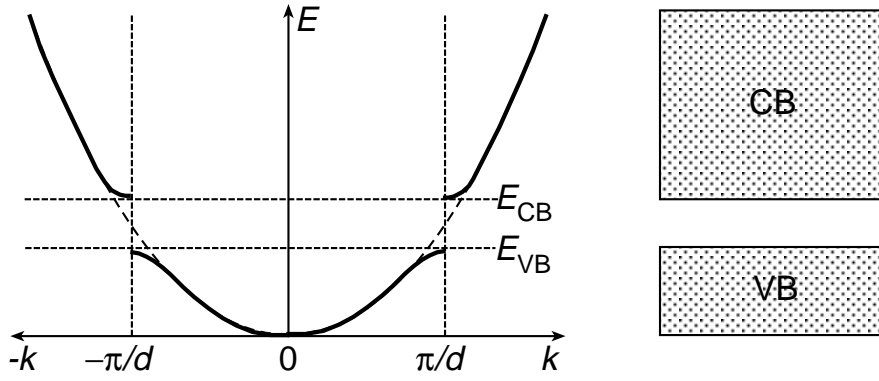


Figure 1.1 The formation of energy bands in a macroscopic semiconductor due to Bragg reflection of the electrons on the periodic lattice of the crystal.

x-directions. The electron density corresponding to the first standing wave is centered at the core ions, that of the second wave between the core ions. The two standing waves correspond to considerably different energies. The energy difference can be estimated by a perturbation method; it is equal to the periodic lattice potential in the x-direction. The scattering of the free electrons by the periodic lattice leads to discontinuities in the $E(k)$ relationship for k values at around $k = q \frac{\pi}{d}$. These discontinuities lead to the formation of energy bands, separated by energy gaps, as presented in Figure 1.1. This derivation for the x-direction can be used in a similar way for the y and z-directions. The $E(k)$ relationship for free electrons is a good approximation for most of the electrons in a band, except for those near the edge of the Brillouin zones.

1.2.2 Quantum Size Effects

A (Wannier) exciton can be defined as the bound state of an electron-hole pair, which is due to a Coulomb interaction between the charge carriers.¹ The distance between the electron and the hole is the Bohr radius of the exciton, a_B , and is given by,

$$a_B = \frac{4\pi\epsilon_0\epsilon_\infty\hbar^2}{m_0 e^2} \left(\frac{1}{m_e^*} + \frac{1}{m_h^*} \right) \quad (1.6)$$

in which m_e^* and m_h^* are the effective electron and hole masses, respectively, and ϵ_∞ is the high-frequency relative dielectric constant of the medium. The resulting Bohr radius is much larger than that of a hydrogen atom, since the effective masses are considerably smaller than the mass of

the electron at rest, m_0 , and ϵ_∞ is considerably larger than 1. Values for a_B for the common semiconductors are in the range 10-100 Å.

Nanocrystals have crystalline order and dimensions corresponding to some tens of a lattice constant in each direction. Electron scattering with the lattice leads to band formation, as for macroscopic crystals. However, the free electron wavelength and the Bohr radius can be comparable to or even larger than the crystal dimensions. This means that the nanocrystal acts as a quantum box for quasiparticles. The symmetry of the box is important for the solution of the Schrödinger equation. In the literature, a spherical symmetry is often used. For simplicity, we consider a rectangular box of dimensions L_x , L_y , and L_z surrounded by infinitely high energy walls. Stable solutions of the Schrödinger equation are standing waves. For instance in the x-direction, the free-electron and free-hole standing waves must fulfill,

$$L_x = n_e \times \frac{\lambda_e}{2} \quad (n_e = \pm 1, \pm 2, \dots) \quad (1.7)$$

$$L_x = n_h \times \frac{\lambda_h}{2} \quad (n_h = \pm 1, \pm 2, \dots) \quad (1.8)$$

From equations (1.5), (1.7) and (1.8) it follows that size quantisation in the x-direction gives discrete k_x values for the electrons and holes. The total number of discrete states depends on the well width and depth. In the case of walls with a finite height, the wave function does not vanish at the edge of the well, but decays exponentially in the classically forbidden region. Therefore, the probability of finding a particle inside the well is always less than unity and decreases with increasing E_n . As a result of the reduced number of states and the confinement of the electron wave functions, a part of the $E(k)$ curve is replaced by discrete points as shown in Figure 1.2. We return to this model in chapter 6.

Brus has modelled electron confinement in a spherical box by using the effective mass approximation^{5,34} When $R \ll a_B$ the confined electron and hole have no bound state as in the definition of an exciton given above and the Coulomb interaction may be ignored to a first approximation. The mathematical treatment is similar to that for an electron in the spherical potential well of a nucleus.³⁵ The state of the system is characterized by three quantum numbers, namely the principal number n , the orbital number l , and the magnetic number m . The states corresponding to different l values are denoted as s -, p -, d -, and f - states. Each state with a given l value has a $(2l+1)$ degeneracy, corresponding to $m = 0, \pm 1, \pm l$. For a spherically symmetrical potential box with an infinite barrier, the resulting energy of the exciton can be written as follows,

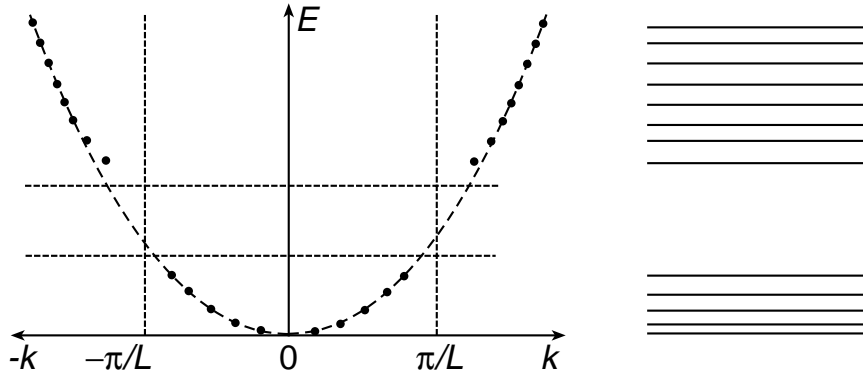


Figure 1.2 Due to the size-confinement of the semiconductor nanocrystal only the electron wave functions obeying $R=n\lambda/2$ can form standing waves; this and the reduced number of states lead to the formation of discrete energy levels instead of energy bands.

$$E_{nl} = E_g + \frac{\hbar^2 \chi_{nl}^2}{2m_0 R^2} \left(\frac{1}{m_e^*} + \frac{1}{m_h^*} \right) \quad (1.9)$$

in which E_g is the bandgap of the macrocrystalline semiconductor, defined as the energy needed to excite an electron from the top of the valance band to the bottom of the conduction band. χ_{nl} is the n^{th} root of the spherical Bessel function and l the order of the function; for $l=0$ (so-called s -states) $\chi_{n0} = \pi n$.

Weakly quantised quantum dots (with $R \sim a_B$) contain a large number of atoms and unit cells; therefore Bragg reflection at the periodic lattice will lead to the formation of continuous energy bands. Only the levels at the top of the valence band and at the bottom of the conduction band, which correspond to the most delocalised electron wave function, will be discrete (see Figure 1.3 (b)). Highly quantised semiconductor quantum dots are sometimes called artificial atoms because they exhibit a discrete optical spectrum determined by their size (see Figure 1.3 (c)).

The electron and hole, confined in a space with dimensions smaller than the Bohr radius of the exciton, cannot however be considered as independent particles; the Hamiltonian must be expanded by two-particle kinetic terms and the Coulomb and confinement potential. This leads in the Brus model to an expression for the energy of the ground state of the electron-hole pair ($1s_e 1s_h$ or first excited state),

$$E(1s_e 1s_h) = E_g + \frac{\pi^2 \hbar^2}{2m_0 R^2} \left(\frac{1}{m_e^*} + \frac{1}{m_h^*} \right) - A \frac{e^2}{4\pi\epsilon_0 \epsilon_\infty R} \quad (1.10)$$

in which the second term describes confinement and the third the Coulomb electron-hole interaction. The coefficient A corresponds to 1.786 for the $1s_e1s_h$ state and has values between 1.6 and 1.9 for other states.³⁶ Equation (1.10) implies that the gap between the filled valence band levels and the empty conduction band levels increases when the radius of the particle decreases. Due to the electron-hole Coulomb interaction, the measured optical bandgap has a slightly lower energy than the 'actual' electronic band gap.

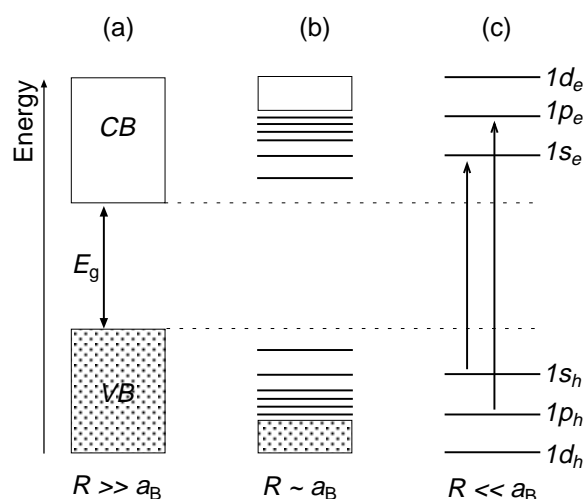


Figure 1.3 The effect of size on the electronic structure of a semiconductor crystal for three different size-ranges. (a) a macrocrystalline semiconductor ($R \gg a_B$) with continuous energy bands; the filled valence band (VB) and empty conduction band (CB) and the bandgap energy (E_g) are shown. (b) semiconductor nanocrystal with a weak size-quantization ($R \sim a_B$). (c) highly quantised dot ($R \ll a_B$) with discrete atomic-like energy levels and optical transitions.

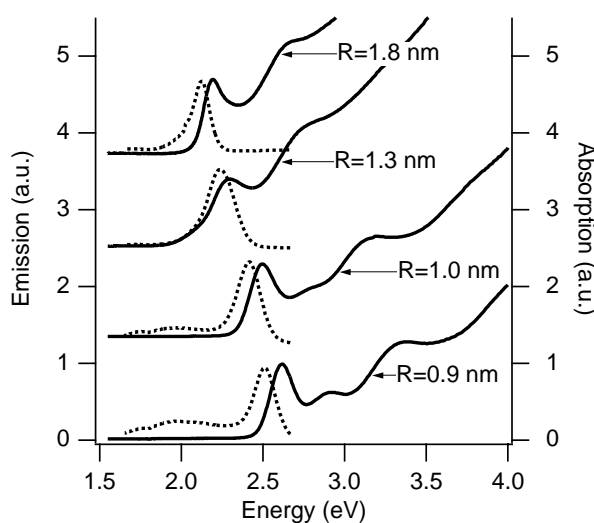


Figure 1.4 Absorption (solid lines) and emission (dotted lines) spectra of colloidal CdSe quantum dots, showing that the absorption edge shifts towards higher energies with respect to bulk CdSe (1.84 eV) and that discrete energy bands become more pronounced as the particle size decreases.

The increase of the bandgap and the transition from continuous energy bands to discrete energy levels upon a decrease of particle size has been observed by optical absorption spectroscopy in many colloidal semiconductor systems.^{30,37} The absorption and emission spectra of colloidal CdSe quantum dots of different sizes studied in this work (see Figure 1.4) demonstrate these effects. Upon a decrease of the particle radius, the onset of the absorption and the emission maximum shift towards higher energies. A clear structure in the absorption spectra is observed for the smallest particles, corresponding to discrete optical transitions.

1.2.3 Surface States

Although the presence of surface states is by no means a size-quantisation effect, surface states become increasingly important as the size of a structure reduces; the ratio of the number of surface to bulk atoms, which increases with decreasing particle radius, is very large for quantum dots. Surface atoms give rise to electron levels of energy different from those of the bulk levels; these levels can play an important role in light absorption and emission.³⁸ The importance of surface states in the photoexcited decay dynamics has become clear from time-resolved luminescence spectroscopy on colloidal suspensions of quantised PbS, CdS, CdSe, ZnO, and InP.³⁹⁻⁴² Besides direct conduction-to-valence band recombination, a broad band at lower energy is often observed in emission spectra;³⁷ this sub-bandgap emission can correspond to a transition either from the conduction band to a bandgap state, or from a bandgap state to the valence band. Alternatively, surface states can provide pathways for non-radiative recombination and therefore decrease the luminescence quantum yield. Charge carriers can also be trapped in deep bandgap states, forming a long-lived excited state of lower energy.⁴³

1.3 Electron Tunneling

1.3.1 Basic Principles of Electron Tunneling

Metals and semiconductors generally have a high potential energy barrier at their surface, which confines the electrons within the solid.⁴⁴ At room temperature thermally activated escape of the electrons over the surface barrier is very improbable. However, quantum mechanical tunneling can occur when the interfacial barrier is very thin. This is the main mechanism of electron transfer through an insulating barrier between two solids in intimate contact.

The free electron model discussed in section 1.2 allows a more quantitative discussion of the probability of finding an electron in a limited region just outside a crystal. The potential energy in the crystal is set to zero, and that of an electron at rest outside the crystal to E_{vac} . The Fermi-energy of the electrons in the crystal is considerably below E_{vac} ; The work function, $E_{vac}-\mu_e$, is generally of the order of a few eV. The Schrödinger equation for a single free electron in the region outside the crystal for the x-direction is given by,

$$-\frac{\hbar^2}{2m_e} \frac{\partial^2}{\partial x^2} \Psi(x) + E_{vac} \Psi(x) = E(x) \Psi(x) \quad (1.11)$$

The energy of the electron at rest in vacuum is larger than the total energy $E(x)$ of the impinging electron. A solution of equation (1.11) is,

$$\Psi_{vac}(x) = \frac{1}{\sqrt{L}} e^{-\kappa_{vac} x} \quad (1.12)$$

where x is the distance from the surface and κ_{vac} the decay parameter in the x-direction

$$\kappa_{vac} = \left[\frac{2m_e(E_{vac} - E(x))}{\hbar^2} \right]^{\frac{1}{2}} \quad (1.13)$$

The wave function of an electron impinging on a surface wall decays exponentially outside the metal. The decay length $1/\kappa_{vac}$ depends on the effective barrier height $E_{vac}-E(x)$. Tunneling of an electron between two solid phases can occur if these phases are separated by a distance of the order of $1/\kappa_{vac}$. The probability of tunneling is relatively small when $x > 1/\kappa_{vac}$ (strong attenuation), and is then given by,

$$T = T_0 e^{-2\kappa_{vac} d} \quad (1.14)$$

The distance dependence of the tunneling probability is determined by the exponential term, since the prefactor depends only weakly on the effective barrier height. Electrons close to the Fermi-energy which fulfill the condition $k_x^2 \gg k_y^2 + k_z^2$ have the highest tunnel probability for a barrier width, d . The rate constant for electron tunneling, *i.e.* the number of tunneling events per electron level per second, can be defined as,

$$k = k_0 e^{-\beta d} \quad (1.15)$$

in which k_0 is the maximum number per second for $d \rightarrow 0$, and β is equal to $2\kappa_{vac}$. A typical value of β for an effective barrier height of 1 eV is 1.0 \AA^{-1} . A change of 1 \AA in the barrier width typically leads to a change of the tunneling rate by a factor 2.71. This extreme sensitivity of the tunneling rate to the barrier width forms the basis for the Scanning Tunneling Microscope (STM), developed in 1982.⁴⁵ Already in 1922 field emission from metals was observed⁴⁶ and since 1937 the Field-Emission Microscope (FEM) has been used to study electron tunneling and the surface structure of metals.⁴⁷ Since 1960 electron tunneling was studied with planar metal/insulator(vacuum)/metal junctions.^{48,49}

1.3.2 Electron Tunneling between a Quantum Dot and a Metal

Colloidal semiconductor quantum dots can be adsorbed on a metal electrode by Van der Waals interactions of the capping molecules, which stabilize the dots in the suspension, with the metal surface. Alternatively, covalent anchoring of the dots to the metal is possible with a difunctionalised Self-Assembled Monolayer (SAM).⁵⁰⁻⁵⁵ In addition, QDs can be grown electrochemically on a conductive substrate; the particle size can be controlled by the charge used to electrodeposit the dots.⁵⁶⁻⁵⁸

A metal coated with a (sub)monolayer of nanocrystals can be used as working electrode in a conventional electrochemical cell. With such electrodes we have performed time-resolved photoelectrochemistry. The metal electrode, coated with a monolayer of dots, can be considered as a 2D array of mutually independent Double-Barrier Tunnel Junctions (DBTJ). The junctions are formed between the metal substrate and the dot and between the dot and the electrolyte. Using a modulated light intensity it is possible to measure the rate of photoinduced tunneling between the dots and the metal or the electrolyte solution.

With Scanning Probe techniques it is possible to perform electrical measurements on individual quantum dots. When the STM tip is positioned above a dot a DBTJ is formed consisting of the metal/dot and dot/tip junctions.⁶⁴⁻⁶⁷ A schematic illustration of the Double-Barrier Tunnel Junction is shown in Figure 1.5 (a) for an electrical and (b) for an electrochemical configuration, and in (c) the electrical circuit of the DBTJ for both configurations is shown. The electronic properties of individual semiconductor (and metal) particles have been investigated in this way with Tunneling Spectroscopy (TS).

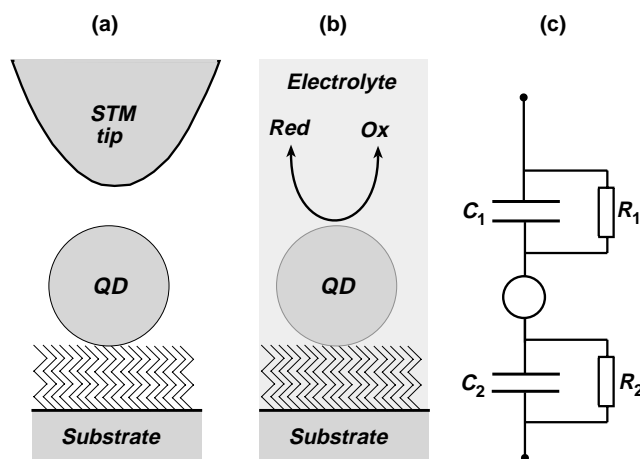


Figure 1.5 Schematic representation of a quantum dot on a Self-Assembled Monolayer on a metal substrate in (a) an electrical setup, with the STM tip as second electrode, and (b) in an electrochemical configuration, in which the electrolyte establishes the contact with the counter electrode. In (c) the electrical equivalent circuit of the Double-Barrier Tunnel Junction is shown for the two configurations.

1.3.3 Photoelectrochemical Measurements

The processes involved in photoinduced electron tunneling between a quantum dot and a metal electrode, forming the basis of the photoelectrochemical and electrical measuring techniques, are presented in this and the following section.

Figure 1.6 shows a quantum dot on a metal electrode. An electron has been excited from a valence band level (HOMO) to a conduction band level (LUMO) of the quantum dot upon absorption of a photon ($h\nu > E_g$). Direct band-band recombination is usually very fast (\sim ps) and returns the system to the ground state. However, trapping of the hole or the electron in a bandgap state may compete with the fast relaxation to the ground state. As a result, an excited state of lower energy is formed. It will become clear in this work that such a photoexcited state can possess a long lifetime, so that photoinduced tunneling between the dot and the metal can occur. Resonant tunneling of the photoexcited electron to the metal is only possible when the substrate Fermi level ($E_{F,\text{sub}}$) is below the electron level (E_e), and an electron can only tunnel from the metal to the unoccupied level in the dot when the metal Fermi level is above this level (E_h). Thus, relaxation of the excited state to the ground state via photoinduced tunneling to and from the metal can only occur when $E_h < E_{F,\text{sub}} < E_e$. Decay of the photoexcited state via the metal can be observed by time-resolved measurement of the current in the external electrical circuit. When $E_{F,\text{sub}}$ is scanned and the photoinduced tunneling currents are measured in the external circuit, the electronic levels of the long-lived excited state can be resolved. The rate constants of these

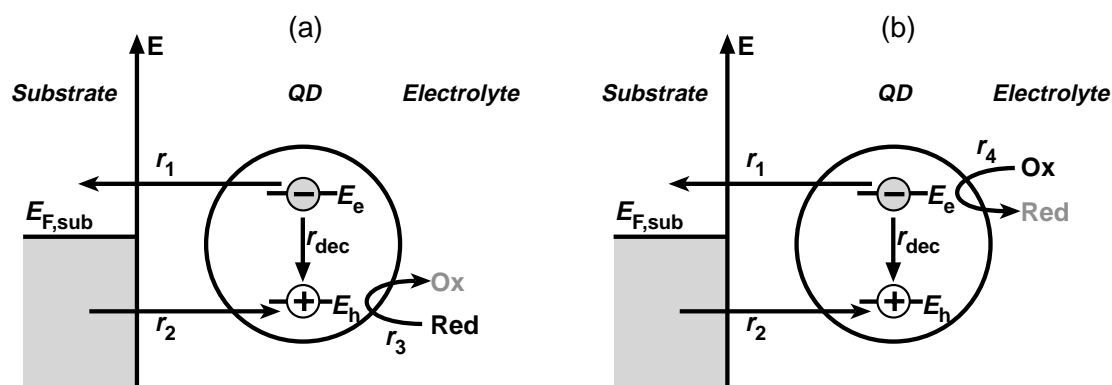


Figure 1.6 A photoexcited quantum dot adsorbed on a metal electrode, forming a DBTJ. After a photon is absorbed, one of the charge carriers is trapped in a localised state. (a) A hole scavenger is added to the electrolyte; when r_1 is followed by r_3 a steady-state anodic photocurrent is observed. (b) An electron scavenger is added; when r_2 is followed by r_4 a steady-state cathodic photocurrent is measured.

tunneling processes may be determined by using time-resolved photoelectrochemistry. This technique will be explained in section 1.4. In the presence of either a reducing agent (Figure 1.6(a)) or an oxidizing agent (Figure 1.6(b)), electron transfer may also occur between the dot and the electrolyte. When r_1 is followed by r_3 , a steady-state anodic photocurrent will be observed. Otherwise, when r_2 is followed by r_4 , a steady-state cathodic photocurrent results.

1.3.4 Electrical Measurements with a Substrate/Dot/Tip Configuration

Figure 1.7 shows an energy level scheme for a highly quantised semiconductor quantum dot (with discrete energy levels) in contact with a metal substrate. By positioning the STM tip above the particle a DBTJ is formed. For simplicity, we assume that $E_{F,sub}$ is fixed with respect to the energy levels in the quantum dot. At small bias ($\Delta E \ll E_g$) the Fermi levels of the tip and the substrate are located in the bandgap of the nanocrystal and resonant electron tunneling via energy levels of the dot cannot occur. If a bias potential is applied such that $E_{F,tip} > E_{F,sub}$, resonant tunneling of an electron from the tip to the dot and from the dot to the substrate can occur when $E_{F,tip}$ reaches the first discrete conduction band level of the quantum dot. When $E_{F,tip}$ is raised further and reaches the next level, tunneling through this level can also take place. At a bias such that $E_{F,tip} < E_{F,sub}$ an electron can tunnel from the substrate to tip, via the levels of the valence band. In the current-bias plot a zero current range around $\Delta E = 0$ will be found, corresponding to the bandgap of the quantum dot. Steps in the current-bias (I - V) plot or peaks in the conductance-bias plot (dI/dV - V) will appear at bias values corresponding to resonant tunneling through discrete

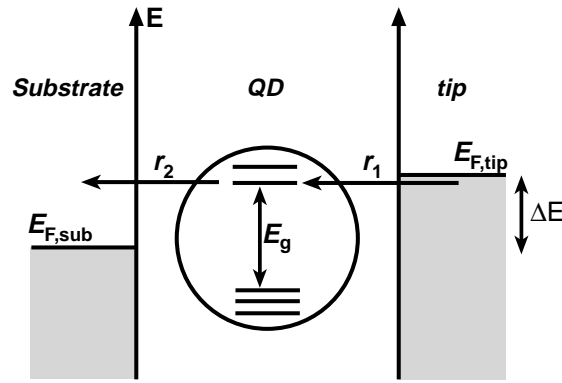


Figure 1.7 A schematic representation of a DBTJ for a metal/dot/tip configuration. Resonant tunneling via a discrete energy level in the quantum dot can occur when $E_{F,tip}$ reaches that level.

energy levels of the quantum dot. For an unambiguous assignment of the peaks in the dI/dV vs V curve, it is necessary to have an asymmetrical DBTJ, such that $E_{F,sub}$ is locked to the energy levels of the quantum dot. Furthermore, Tunneling Spectroscopy using an electrostatic gate electrode or a magnetic field can be very helpful in elucidating the electronic structure of semiconducting quantum dots.^{68,69}

1.4 Intensity-Modulated Photocurrent Spectroscopy

Intensity-Modulated Photocurrent Spectroscopy (IMPS) is a time-resolved optoelectrical method. In this work the technique is used in a photoelectrochemical context to determine the rate constants of electron tunneling processes between the semiconductor quantum dots and a metal or redox system in the solution. IMPS has previously been used to study recombination processes, majority carrier injection at the bulk semiconductor/electrolyte interface⁷⁰, and charge transport in nanoporous semiconductor electrodes.⁷¹⁻⁷³ In this section the principle of the technique will be briefly described.

In IMPS, a small sinusoidal modulation, $\Phi(\omega)$, is superimposed on a steady-state light intensity, Φ , giving a photocurrent which also has a sinusoidal contribution (ω is the modulation frequency). The modulated photocurrent $j(\omega)$ is measured using frequencies, ω , lower than $(RC)^{-1}$. The ratio $j(\omega)/e\Phi(\omega)$ is called the optoelectrical transfer function. Slow processes contributing to the total photocurrent will lead to a phase shift, $\theta(\omega)$, between $\Phi(\omega)$ and $j(\omega)$. The transfer function, determined by the amplitude ratio and the phase shift, can be plotted in the complex plane (imaginary component vs real component) or in a Bode plot (imaginary or real component vs frequency). In the experimental set-up used here, consisting of an illuminated metal/QD working electrode, the frequencies at which the imaginary part of the function shows

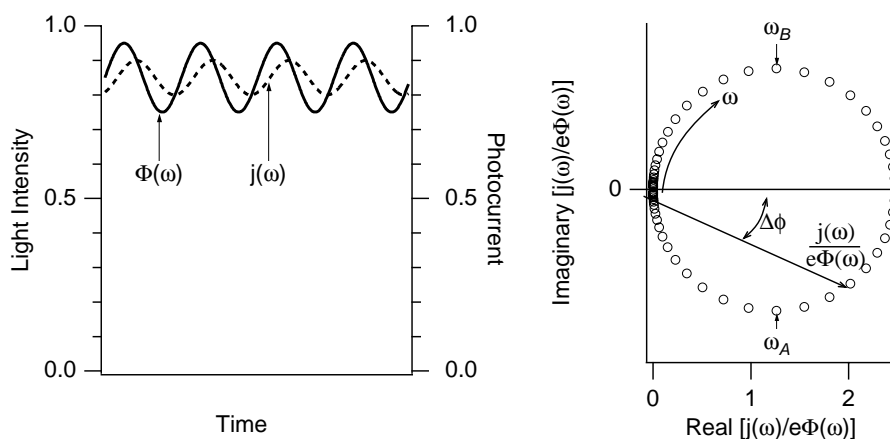


Figure 1.8 The principle of IMPS. (a) Modulated light intensity and photocurrent as a function of time. The modulation depth is $\sim 10\%$ of the base light intensity. (b) Complex plane plot of the recombination process of a photoexcited state in a semiconductor quantum dot adsorbed on a metal electrode via the metal. ω_A and ω_B correspond to the rate constants of the anodic and cathodic electron tunneling processes, respectively.

an extremum correspond to the rate constants of the photoinduced electron transfer between the QD and the metal, or the redox species in the electrolyte. The experimental data and the theoretical derivation of $j(\omega)/e\Phi(\omega)$ are the subject of chapters 2, 3, and 4. In Figure 1.8 the optoelectrical transfer function, which might be expected for the decay of a photoexcited state in the quantum dot via the metal, is shown in the complex plane with the frequency as a parameter. In the high frequency limit electron transfer is slower than the light modulation, and both the real and imaginary components are zero. When the frequency is decreased, the phase shift between $\Phi(\omega)$ and $j(\omega)$ decreases, and a signal is observed. The frequency at the minimum of this semicircle, ω_A , corresponds to the rate constant for electron tunneling from the dot to the gold, since the real component is anodic. When the frequency is further decreased a semicircle in the positive-positive quadrant is observed. The frequency at the maximum of this semicircle, ω_B , corresponds to electron tunneling from the gold to the unoccupied level in the dot. In the low frequency limit the function is zero, meaning that both transfer from the QD to the metal and from the metal to the QD can follow the light modulation.

1.5 Outline of this Thesis

In this thesis a study of resonant electron tunneling between II-VI semiconductor quantum dots and a metal substrate is described. Gold electrodes were provided with a monolayer of quantum dots for the photoelectrochemical measurements and for the STS. Chapters 2, 3 and 4

deal with the study of photoinduced electron tunneling between nanocrystalline CdS, PbS and CdSe particles, respectively, and the gold electrode. In the literature, a long-lived excited state was reported for Q-CdS and Q-CdSe; the exact nature of these states could not be elucidated by optical spectroscopy. The electronic structure of the long-lived excited state in CdS, PbS and CdSe quantum dots was studied with photoelectrochemistry. The resulting picture of the long-lived excited state, complements the data obtained with optical spectroscopy. In CdS and CdSe, the long-lived excited state consists of a hole in a deep trap in the bandgap and an electron in the LUMO, whereas in PbS the electron is deeply trapped and the hole is in the HOMO. These long-lived excited states have a much lower energy than the primary (LUMO-HOMO) exciton. Recombination of the excited state via the gold levels due to consecutive electron tunneling to and from the gold was observed. Steady-state anodic and cathodic photocurrents, due to electron injection from tartrate and electron scavenging by ferricyanide, were also seen.

With IMPS the rate constants of the electron transfer processes were obtained. We found that electron tunneling from the dot to the gold was the fastest process in the CdS/Au and CdSe/Au systems. In the PbS/Au system, electron tunneling from the gold to the unoccupied level in the dot was the fastest process. By varying the temperature, the tunneling processes could be distinguished from a possible electrochemical step; the rate constant of tunneling is, in principle, independent of the temperature, in contrast to that of an electrochemical reaction. A mathematical model was derived and fitted to the experimental results. Experiment and theory were in good agreement. These results indicated that the non-trapped charge carrier has a higher tunnel probability than the trapped charge carrier, which was not completely understood.

In chapter 4, results are described for colloidal CdSe particles, covalently bound to Self-Assembled Monolayers of (non-rigid) dithiols and rigid disulfide spacer molecules. The aim of this work was to study the distance dependence of electron tunneling in the Au/SAM/Q-CdSe assembly. An advantage of such a system is that the photoinduced electron transfer is not thermally activated. Generally, thermally activated electron transfer (ET) forms a serious problem in the interpretation of the distance-dependence of ET, because in most systems the molecular and environmental properties, and hence the reaction free energy, and the activation energy also change with the distance between the electron donor and acceptor. When alkane dithiols were used as spacer molecules, the measured rate constants depended on the applied potential and did not show a trend upon a chain length variation. Probably the SAM deformed on applying a potential and the tunneling distance changes. Possibly due to the flexibility of the molecules, the distance between the dots on the monolayer and the gold was not constant. With a rigid disulfide as a linker between the gold surface and the CdSe dots, the tunneling rate constants depended

exponentially on the distance. A value of 0.5 \AA^{-1} was found for β , the decay parameter; this value was rather small in comparison to values found in metal/vacuum/metal systems. Very likely, the wave function in the CdSe quantum dot is coupled to the gold wave functions via a through-bond interaction, in which the σ -orbitals of the cyclohexylidenes and the π -orbitals of the double bonds of the spacer molecules are involved. Photoelectron spectroscopy has shown that the lone pair π -type orbitals of the sulfide groups had a strong interaction in this type of molecule.

In the work described in chapter 5, resonant tunneling in a Au/QD/tip DBTJ was studied using CdS and CdSe quantum dots. With nanocrystals bound to gold via a spacer molecule, the potential was distributed over both junctions of the metal/dot/tip system. In this case, resonant tunneling occurred via the levels of the conduction band at positive and at negative bias; the tunneling spectra were quite symmetrical. Quantum dots, electrodeposited epitaxially, were strongly coupled to the gold. An asymmetrical DBTJ was formed when the tip is placed above the dot. In this configuration the substrate Fermi-level was fixed with respect to the energy levels in the dot. When the bias was sufficiently positive or negative, the discrete energy levels of the conduction and valence band were observed, respectively. The potential range of zero current was independent of the dot/tip distance and corresponded to the bandgap of the quantum dot.

An STS study at cryogenic temperatures on the electronic structure of individual CdSe quantum dots is presented in chapter 6. Colloidal CdSe nanoparticles were attached to a bare gold surface. The symmetry of the DBTJ was varied by changing the tip/dot distance and, as a consequence, not only the ratio of capacitances was changed but also the ratio of the rates of electron tunneling to and from the dot. If tunneling from the dot to the substrate was much faster than tunneling from the tip to the dot, the probability that an orbital of the dot was occupied by an electron was very small, and electron-electron Coulomb charging effects were negligible. In this case the conduction and valence band levels were probed, but the degeneracy of the levels was not resolved. If the rates of electron tunneling to and from the dot were comparable, the occupation probability of an orbital in the dot by an electron might be sufficiently high to observe Coulomb charging. Due to the charging, degenerate energy levels could be resolved. The measured electronic structure of CdSe quantum dots could be described on the basis of the model for an electron in a cubic box.

References

- 1 S.V. Gaponenko, *Optical Properties of Semiconductor Nanocrystals* **1998**, Cambridge University Press, United States of America
- 2 MRS Bulletin, february **1998**
- 3 G. Jaeckel, *Z. Tech. Phys.* **1926**, 6, 301
- 4 A. Henglein, *J. Phys. Chem.* **1982**, 86, 2291-2293
- 5 L.E. Brus, *J. Chem. Phys.* **1984**, 80, 4403
- 6 H. Mattoussi, L.H. Radzilowski, B.O. Dabbousi, D.E Fogg, R.R. Schrock, E.L. Thomas, M.F. Rubner, and M.G. Bawendi, *J. Appl. Phys.* **1999**, 86, 4390
- 7 Y. Yang, S. Xue, S. Liu, J. Huang, and J. Shen, *Appl. Phys. Lett.* **1996**, 69, 377
- 8 D.L. Klein, P.L. McEuen, J.E. Bowen Katari, R. Roth, and A.P. Alivisatos, *Appl. Phys. Lett.* **1996**, 68, 2574
- 9 M.A. Kastner, *Nature* **1997**, 389, 667
- 10 D.L. Klein, R. Roth, A.K.L. Lim, A.P. Alivisatos, and P.L. McEuen, *Nature* **1997**, 389, 699
- 11 H. Weller, *Advanced Materials* **1993**, 5, 88
- 12 J. Fang, J. Wu, X. Lu, Y. Shen, and Z. Lu, *Chem. Phys. Lett.* **1997**, 270, 145
- 13 S. Kohtani, A. Kudo, and T. Sakata, *Chem. Phys. Lett.* **1993**, 206, 166
- 14 C. Nasr, P.V. Kamat, and S. Hotchandani, *J. Electroanal. Chem.* **1997**, 420, 201
- 15 D. Liu, and P.V. Kamat, *J. Phys. Chem.* **1993**, 97, 10769
- 16 Y.A. Vlasov, N. Yao, and D.J. Norris, *Advanced Materials* **1999**, 11, 165
- 17 V.L. Colvin, M.C. Schlamp, and A.P. Alivisatos, *Nature* **1994**, 370, 354
- 18 B.O. Dabbousi, M.G. Bawendi, O. Onitsuka, and M.F. Rubnar, *Appl. Phys. Lett.* **1995**, 66, 1316
- 19 A.P. Alivisatos, K.P. Johnsson, X. Peng, T.E. Wilson, C.J. Loweth, M.P. Bruchez jr, and P.G. Schultz, *Nature* **1996**, 382, 609
- 20 D.F. Ollis, H. Al-Ekabi, Photocatalytic Purification and Treatment of Water and Air, Elsevier Science Publishers **1993**, Amsterdam, The Netherlands
- 21 C. Dekker, *Physics. Today* **1999**, 52, 22
- 22 J.R. Arthur, *J. Appl. Phys.* **1968**, 39, 4032
- 23 A.Y. Cho, *J. Vac. Sci. Technol.* **1971**, 8, S31
- 24 D. Heitmann, and J P. Kotthaus, *Physics Today* **1993**, june, 56
- 25 M.A. Kastner, *Physics Today* **1993**, january, 24
- 26 U. Rothlisberger, W. Andreoni, M. Parinello, *Phys. Rev. Lett.* **1994**, 72, 665

- 27 L. Spanhel, M. Haase, H. Weller, and A. Henglein, *J. Am. Chem. Soc.* **1987**, *109*, 5649
- 28 M.L. Steigerwald, A.P. Alivisatos, J.M. Gibson, T.D. Harris, R. Kortan, A.J. Muller, A.M. Thayer, T.M. Duncan, D.C. Douglas, L.E. Brus, *J. Am. Chem. Soc.* **1988**, *110*, 30460
- 29 X. Peng, L. Manna, W. Yang, J. Wickham, E. Scher, A. Kadavanich, and A.P. Alivisatos, *Nature* **2000**, *404*, 59-61
- 30 C.B. Murray, D.J. Norris, and M.G. Bawendi, *J. Am. Chem. Soc.* **1993**, *115*, 8706
- 31 H. Matsumoto, T. Sakata, H. Mori, H. Yoneyama, *J. Phys. Chem. B* **1996**, *100*, 13781
- 32 A. van Dijken, A. Meijerink, D. Vanmaekelbergh, *Chem. Phys. Lett.* **1997**, *269*, 494
- 33 N.W. Ashcroft, and N.D. Mermin, *Solid State Physics* **1976**, Philadelphia
- 34 L.E. Brus, *J. Phys. Chem.* **1986**, *90*, 2555
- 35 P.W. Atkins, *Physical Chemistry* **1990**, Oxford University Press, Great Britain
- 36 H.M. Schmidt, and H. Weller, *Chem. Phys. Lett.* **1986**, *129*, 615-618
- 37 A. Henglein, *Topics in Current Chemistry* **1988**, *143*, 115
- 38 A.P. Alivisatos, *J. Phys. Chem.* **1996**, *100*, 13226
- 39 A.J. Nozik, and O.I. Micic, *MRS Bulletin* february **1998**, 24
- 40 M. Kuno, J.K. Lee, B.O Dabbousi, F.V. Mikulec, and M.G. Bawendi, *J. Chem. Phys.* **1997**, *106*, 9869
- 41 M.T. Nenadovic, M.I. Comor, V. Vasic, and O.I. Micic, *J. Phys. Chem.* **1990**, *94*, 6390
- 42 P. Guyot-Sionnest, and M.A. Hines, *Appl. Phys. Lett.* **1998**, *72*, 686
- 43 W.J. Albery, G.T. Brown, J.R. Darwent, and E. Saievar-Iranizad, *J. Chem. Soc. Faraday Trans. 1* **1985**, *81*, 1999
- 44 R. Wiesendanger, *Scanning Probe Microscopy and Spectroscopy* **1994**, Cambridge University Press, Great Britain
- 45 G. Binnig, H. Rohrer, Ch. Gerber, and E. Weibel, *Phys. Rev. Lett.* **1982**, *49*, 57
- 46 J.E. Lilienfeld, *Z. Phys.* **1922**, *23*, 506
- 47 E.W. Müller, *Z. Phys.* **1937**, *106*, 541
- 48 J. Bardeen, *Phys. Rev. Lett.* **1961**, *6*, 57
- 49 P.V. Gray, *Phys. Rev.* **1965**, *140*, A179
- 50 V.L. Colvin, A.N. Goldstein, and A.P. Alivisatos, *J. Am. Chem. Soc.* **1992**, *114*, 5221
- 51 J.E. Bowen Katari, V.L. Colvin, and A.P. Alivisatos, *J. Phys. Chem.* **1994**, *98*, 4109
- 52 S. Ogawa, F.F. Fan, and A.J. Bard, *J. Phys. Chem. B* **1995**, *99*, 11182
- 53 S. Ogawa, K. Hu, F.F. Fan, and A.J. Bard, *J. Phys. Chem. B* **1997**, *101*, 5707
- 54 M. Miyaki, H. Matsumoto, M. Nishizawa, T. Sakata, H. Mori, S. Kuwabata, and H. Yoneyama, *Langmuir* **1997**, *13*, 742

- 55 S. Drouard, S.G. Hickey, and D.J. Riley, *Chem. Commun.* **1999**, 8, 67
- 56 T. Nakanishi, B. Ohtani, K. Uosaki, *J. Phys. Chem .B* **1998**, 102, 1571
- 57 G. Hodes, I.D.J. Howell, and L.M. Peter, *J. Electrochem. Soc.* **1992**, 139, 3136
- 58 B. Alpers, H. Demange, I. Rubinstein, and G. Hodes, *J. Phys. Chem. B* **1999**, 103, 4943
- 59 Y. Golan, G. Hodes, and I. Rubinstein, *J. Phys. Chem.* **1996**, 100, 2220
- 60 Y. Kuk, M.F. Jarrold, P.J. Silverman, J.E. Bower, and W.L. Brown, *Phys. Rev. B* **1989**, 39, 11168
- 61 R.H.M. Groeneveld, M.W.J. Prins, and H. van Kempen, *Surface Science* **1995**, 331-333, 1299
- 62 B. Alpers, S. Cohen, I. Rubinstein, and G. Hodes, *Phys. Rev. B.* **1995**, 52, R17017
- 63 T.D. Krauss, and L.E. Brus, *Phys. Rev. Lett.* **1999**, 83, 4840
- 64 P.J.M. van Bentum, R.T.M. Smokers, and H van Kempen, *Phys. Rev. Lett.* **1988**, 60, 2543
- 65 R.P. Andres, T Bein, M. Dorogi, S. Feng, J.I. Henderson, C.F. Kubiak, W. Mahoney, R.G. Osifchin, and R. Reifengerger, *Science* **1996**, 272, 1323
- 66 C. Schönenberger, H van Houten, H.C. Donkersloot, A.M.T. van Putten, and L.G.J. Fokkink, *Physica Scripta* **1992**, T45, 289
- 67 U. Banin, Y.W. Cao, D. Katz, and O. Millo, *Nature* **2000**, 400, 542-544
- 68 L. Gurevich, L. Canali, and L.P. Kouwenhoven, *Appl. Phys. Lett.* **2000**, 76, 384-386
- 69 D.C. Ralph, C.T. Black, and M. Tinkham, *Phys. Rev. Lett.* **1997**, 78, 4087-4090
- 70 D. Vanmaekelbergh, A.R. de Wit, and F. Cardon, *J. Appl. Phys.* **1993**, 73, 5049
- 71 P.E. de Jongh, and D. Vanmaekelbergh, *Phys. Rev. Lett.* **1996**, 77, 3427
- 72 D. Vanmaekelbergh, F. Iranzo Marin, and J. van de Lagemaat, *Ber. Bunsenges. Phys. Chem.* **1996**, 100, 616
- 73 L.M. Peter, and D. Vanmaekelbergh, '*Advances in Electrochemical Science and Engineering*' **1999**, John Wiley & Sons, Weinheim, Germany, 77

Excited State Dynamics in CdS Quantum Dots Adsorbed on a Metal Electrode

Abstract

The electronic structure and decay dynamics of a long-lived excited state in CdS quantum dots were investigated in a novel way by a time-resolved opto-electrical method. Q-CdS was adsorbed as a monolayer on a gold electrode and used in a photoelectrochemical cell, the Au/Q-CdS/electrolyte structure forming a Double-Barrier Tunnel Junction. The rates of photoinduced tunneling processes were measured by Intensity-Modulated Photocurrent Spectroscopy (IMPS). These tunneling processes compete with intra-particle decay of a long-lived excited state. In this way the excited state dynamics could be studied. It was deduced that the long-lived excited state consists of an electron in the LUMO and a hole trapped in a level in the bandgap.

2.1 Introduction

CdS is one of the most extensively studied nanocrystalline semiconductors. Brus and Henglein used CdS during the early 1980's for the investigation of size-quantisation effects.^{1,2} Much effort has been devoted to the preparation and optical characterisation of suspensions of CdS colloids.

The importance of surface states in the excited-state decay in these semiconductor colloids is clear from luminescence spectroscopy.³⁻⁷ Besides direct exciton recombination, a broad band at lower energy is often observed in the luminescence spectra, which corresponds to the transition from the LUMO to a bandgap state or from a bandgap state to the HOMO. From luminescence spectroscopy alone, it is difficult to determine the precise nature of the electronic transition by which sub-bandgap photons are emitted. For example, the luminescence spectrum of quantised-CdS suspensions shows a peak at around 2.5 eV, corresponding to direct exciton recombination, and a broad band at around 1.9 eV. The rates of direct exciton recombination and sub-bandgap emission are 10^9 and 10^7 sec^{-1} , respectively.⁸ Photobleaching experiments with supra-bandgap light showed the existence of a long-lived excited state with a life time of 50 ms.⁹ This means that the sub-bandgap emission does not lead to the ground state. However, the precise nature of the electronic transition giving rise to the sub-bandgap emission and of the resulting low-energetic excited state cannot be revealed by optical spectroscopy.

In this chapter, we present an opto-electrical method to study the excited state dynamics in quantum dots. The principle of our approach is shown in Figure 2.1. Quantum dots are adsorbed as a monolayer on a metal electrode, which is used as working electrode in a three-electrode electrochemical cell.¹⁰⁻¹²

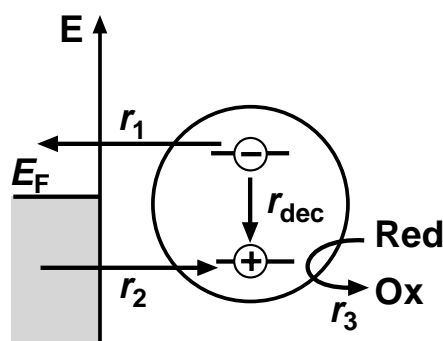


Figure 2.1 Basic model for electron tunneling between a CdS quantum dot and a gold electrode. When $r_{dec} > r_1, r_2, r_3$ intra-particle recombination occurs. When $r_1 > r_{dec}$ and $r_2 > r_3$, gold mediated recombination can be observed in the external circuit. When $r_1 > r_{dec}$ and $r_3 > r_2$, charge separation can be measured in the external circuit.

Upon illumination, a long-lived excited state will be formed, indicated in Figure 2.1. This state may decay to the ground state by an electronic transition within the particle. However, the adsorbed dot forms a metal/dot/electrolyte Double-Barrier Tunnel Junction which enables decay of the excited state by electron tunneling events. If, for instance, the metal Fermi level (E_F) is between the occupied and empty energy level of the long-lived state, decay of the excited state may occur by tunneling of the electron to the metal and subsequent tunneling from the metal to the empty level, or *vice versa*. This decay path is blocked if the metal Fermi-level is above the occupied or below the empty level. Charge separation may occur by tunneling of the electron to the metal and subsequent electron transfer from a reduced species (hole scavenger) in the electrolyte to the empty level. Hence, by scanning E_F and detecting the tunneling events in the external circuit, we could study the electronic structure of the excited state. Moreover, by measurement of the delay between light absorption and photoinduced tunneling processes, the excited state decay dynamics could be investigated.

The excited state dynamics in CdS quantum dots adsorbed on a gold electrode were investigated with Intensity-Modulated Photocurrent Spectroscopy (IMPS). IMPS enabled us to measure the rates of the photoinduced tunneling processes between Q-CdS and gold and between Q-CdS and a reduced species in the electrolyte. By scanning the gold Fermi level, we determined the electronic structure of a long-lived excited state in Q-CdS.

2.2 Experimental Section

The chemicals used were of *pro analysi* quality purchased from Merck. All solutions were prepared from doubly distilled water. The experiments were performed at room temperature, unless otherwise stated.

Suspension. The aqueous Q-CdS suspension was prepared according to the method described in Ref. 8. A 4 ml sample of a 10^{-4} M $\text{Cd}(\text{ClO}_4)_2$ solution was added to 2 ml of a 5×10^{-2} M $\text{Na}(\text{PO}_3)_n$ solution and brought to 100 ml. A small excess (2 ml) of H_2S gas was passed through the solution, which was vigorously shaken, resulting in a clear yellow suspension. Argon was bubbled through the suspension for 24 hours to remove the excess H_2S and oxygen. It is very important to remove all H_2S from the suspension, since it adsorbs on gold and gives rise to a photocurrent.

Photoelectrochemistry. Photoelectrochemical experiments were performed with an EG&G PAR 273A potentiostat and a conventional three electrode cell with a saturated calomel electrode (SCE) as a reference and a platinum counter electrode. All potentials and energies are given with

respect to SCE, which is 4.68 eV below the vacuum level. The working electrode was illuminated with a 450 W Oriel Xenon lamp through a quartz window and a 10 cm quartz water filter.

Gold samples and electrodes. Gold rotating disc electrodes (0.12 cm^2) were mechanically polished with diamond paste and electrochemically cleaned in a 4 M H_2SO_4 solution. CdS quantum dots were deposited on the electrodes by immersion in the suspension and polarizing the electrodes at -0.8 V(SCE) . Alternatively, self-assembled monolayers (SAM) of hexanedithiol and nonanedithiol on gold were prepared by immersing the clean gold electrode in a 5 mM dithiol/ethanol solution for 16 hours. The electrodes were subsequently rinsed with ethanol to remove the excess dithiol from the surface. The CdS quantum dots were deposited by immersing the SAM modified gold electrode in the suspension for another 16 hours and rinsing the electrode thoroughly with water to remove the excess CdS particles. For the STM measurements the samples were rinsed with ethanol and dried under a dry N_2 flow.

Scanning Tunneling Microscopy. For the STM experiments, evaporated gold films on borosilicate glass from Metallhandel Schröer were used. The gold was annealed by heating in a hydrogen flame and quenching in argon. STM images were obtained under ambient conditions with a Nanoscope III (Digital Instruments) scanning tunneling microscope with an electrochemically etched Pt/Ir tip.

Intensity-Modulated Photocurrent Spectroscopy. IMPS experiments (see Figure 2.2) were performed with an EG&G PAR 283 potentiostat and a Solartron 1255 Frequency Response

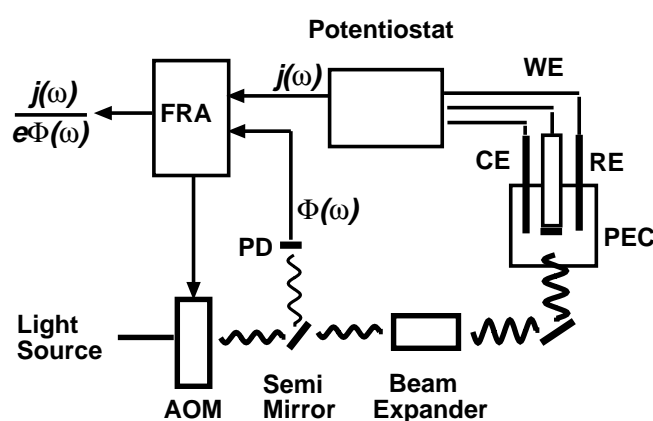


Figure 2.2 IMPS set-up, used for the determination of rates of tunneling of electrons between the quantum dot and the gold electrode. The Frequency-Response-Analyser (FRA) controls the Acousto-Optic Modulator (AOM), which modulates a part (10%) of the light from the incoming laser beam. To establish uniform illumination of the working electrode the beam was expanded. The modulated light intensity, $\Phi(\omega)$, was determined by the reference photodiode (PD), and the modulated photocurrent, $j(\omega)$ by the potentiostat. The FRA gives the opto-electrical transfer function, $j(\omega)/e\Phi(\omega)$.

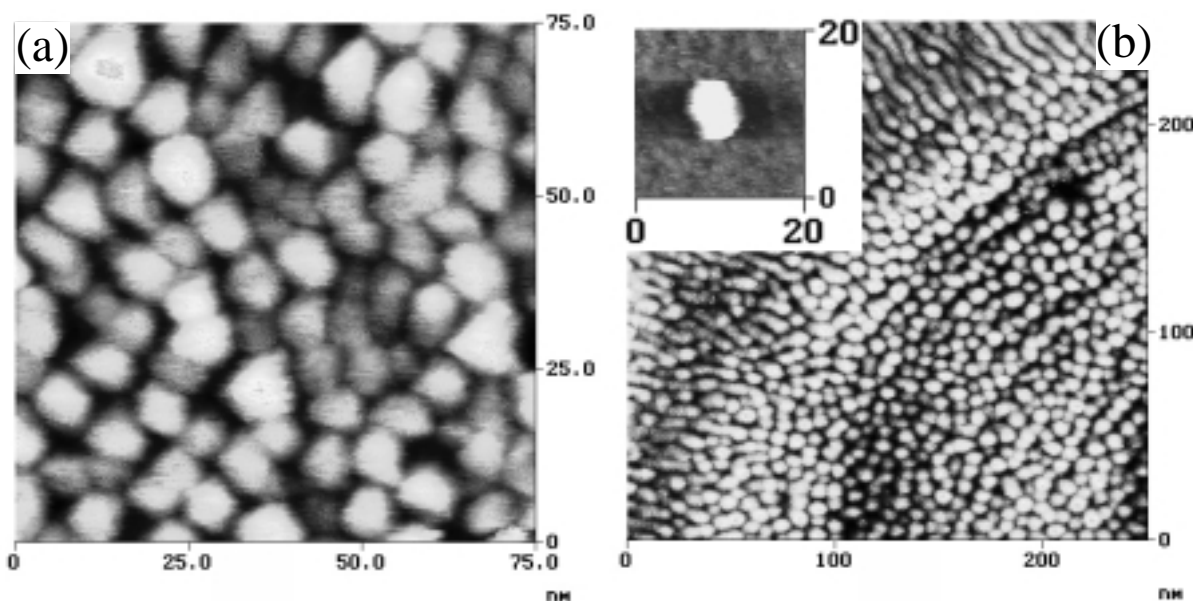


Figure 2.3 STM images of CdS quantum dots deposited on flame-annealed flat Au(111) surfaces (bias -1.5 V, 0.5 nA) (a) CdS deposited on bare gold (b) CdS quantum dots deposited on a hexanedithiol SAM on gold (inset) Single CdS quantum dot on gold.

Analyser (FRA). A Coherent Innova 90 Argon ion laser was used as light source (355 nm, 150 mW) and the light intensity was harmonically modulated by an Isomet 1211 acousto-optic modulator, which was controlled by the FRA. The modulation depth was 10% of the base light intensity. The light was detected by a photodiode, connected to the FRA. The FRA provided the ratio of the modulated photocurrent to the modulated light intensity, *i.e.* the opto-electrical transfer function $j(\omega)/e\Phi(\omega)$.

Electrical Impedance Spectroscopy. EIS measurements were performed with an EG&G PAR 273A potentiostat in a three electrode electrochemical cell. The potential was harmonically modulated with a Solartron 1255 FRA. The modulation amplitude was 10 mV and the modulation frequency was between 6×10^2 and 6×10^5 rad/s. The reference electrode was impedance matched to prevent phase shifts at high frequencies; a platinum wire was placed in solution at the tip of the reference electrode, and was coupled parallel to the reference electrode through a 10 nf capacitor.¹³

2.3 Results

2.3.1 STM

In Figure 2.3 (a) an STM image of Q-CdS on a gold surface is presented. It is clear that the surface is completely covered by CdS quantum dots. From coulometry and quantitative atomic absorption spectroscopy it could be concluded that approximately one monolayer of CdS quantum dots is present on the surface. The quantum dots are not ordered in the layer. The particles are separated by the polyphosphate capping layer. The particle size could not be determined from these measurements, but was obtained from optical absorption experiments, XRD and TEM. The average particle diameter was 50 ± 12 Å. Figure 2.3 (b) shows an STM image of CdS dots on a hexanedithiol SAM covered gold surface. The structure here seems more ordered. Both CdS monolayers, with and without the hexanedithiol SAM, were very robust; multiple scanning with the tip did not affect the appearance of the surface, in contrast to what others have observed.¹² In the inset of Figure 2.3, a single polyphosphate-capped CdS quantum dot on gold is shown. Tunneling spectroscopy experiments on such individual dots indicated that electronic coupling between the particle and the gold is weak; this aspect will be discussed in chapter 5. Very likely this weak coupling is due to polyphosphate chains between the CdS dots and the gold. The junction between the CdS dot and the gold is therefore a tunnel junction with a relatively high resistance.

2.3.2 Photoelectrochemistry

Figure 2.4(a) shows a current-potential plot of a Au/Q-CdS electrode (as in Figure 2.3(a)) in an aqueous 1.0 M KCl solution. The electrode was illuminated with chopped white light from a xenon lamp. Recombination transients set in at a potential of -0.9 V and are observed up to -0.6 V. At more positive potentials, photocurrent transients of a different shape are observed. In contrast to previous reports, minima and maxima in the photocurrent are not found.^{10,11} Figure 2.4(b) shows a current-potential plot of the same electrode in an aqueous solution at pH 14 with tartrate as a hole scavenger. The anodic photocurrent sets in at -1.2 V and shows slow transients. The shape of these transients is different from the case without a hole scavenger, and the steady-state photocurrent is higher by a factor of 10. Photoanodic dissolution did not occur in the first 30 minutes. Tartrate and triethanolamine are well-known stabilizing agents for CdS.^{12,14} The observation of photoinduced current transients and a steady-state photocurrent shows that

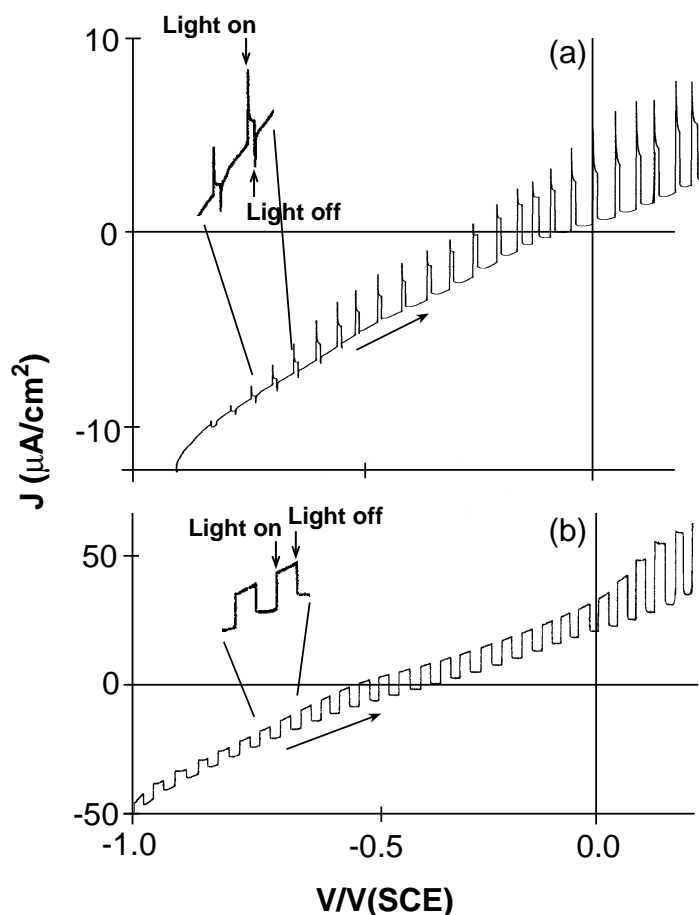


Figure 2.4 (a) Current - potential plot of a Au/Q-CdS electrode, illuminated with chopped light, in an aqueous 1.0 M KCl solution. Photocurrent transients are clearly visible in the potential range between -0.9 V and -0.6 V. At more positive potentials the transients have a different shape. (b) Current - potential plot of a Au/Q-CdS electrode, illuminated with chopped light, in an aqueous 0.5 M tartrate solution of pH 14. The photocurrent onset is at -1.2 V. Note that the photocurrent is much higher than in (a). The scan rate was 5 mV/sec.

electron tunneling events compete with excited state decay in the particle. Electrochemical experiments with CdS single-crystal electrodes have shown that the conduction band edge is located at 1.0 eV in aqueous solutions of pH 7 and at somewhat higher energy in solution of pH 14.¹⁵ In a solution of pH 7 without hole scavenger current transients were observed when E_F was below 0.9 eV; in a solution of pH 14, a photocurrent arises when E_F was below 1.2 eV. It follows that photocurrent transients occur when E_F is below the LUMO of the quantum dot; hence, the long-lived excited state consists of an electron in the LUMO and a trapped hole.

In solution without an electron donor, an anodic transient is found, indicating that electron tunneling from the occupied level to the gold is followed by tunneling from the gold to an empty level in the particle. Relaxation via the gold competes with intra-particle excited state decay. In solution with an electron donor (pH 14), charge separation due to tunneling from the occupied

level to gold and electron transfer from the donor to the empty level in the particle occurs when E_F is below the occupied level.

2.3.3 Opto-electrical transfer function

In Figure 2.5(a) the opto-electrical transfer function, $j(\omega)/e\Phi(\omega)$ for a Au/Q-CdS electrode in aqueous 1.0 M KCl solution (at -0.9 V) is presented in a complex plane plot with the frequency as parameter. In Figure 2.5(b) the modulus of the function, $|j(\omega)/e\Phi(\omega)|$, is plotted versus the modulation frequency. It can be seen that the modulus, which is nearly zero as $\omega \rightarrow 0$, first increases to a maximum and then decreases to zero with increasing frequency. $j(\omega)/e\Phi(\omega)$

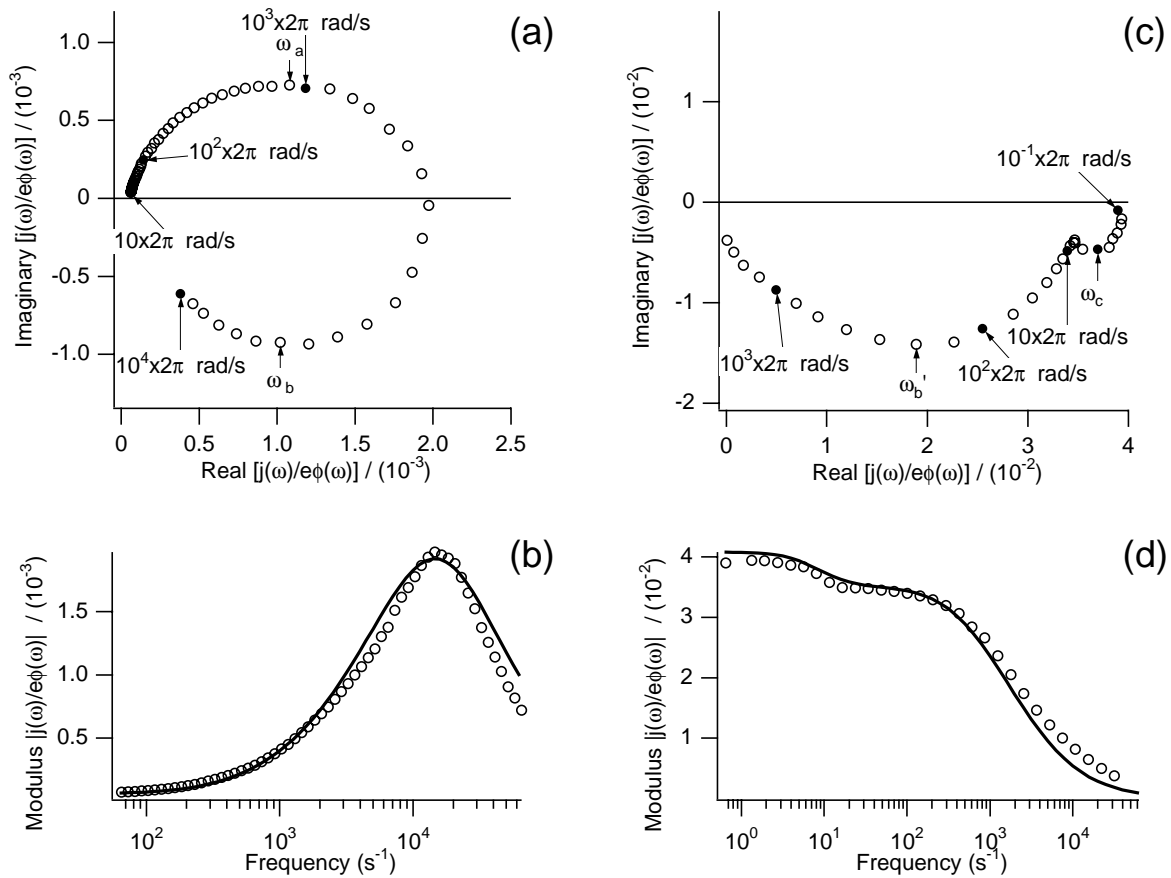


Figure 2.5 (a) Opto-electrical transfer function of a Q-CdS covered gold electrode in an aqueous 1.0 M KCl solution at 297 K plotted in the complex plane (potential -0.9 V). The photon flux was $10^{17}/\text{cm}^2 \cdot \text{s}$ and the modulation frequency was between 60 rad/s and 60×10^3 rad/s. (b) The modulus plotted as a function of the frequency for the results from Figure 2.5(a) (markers) and the model (solid line). (c) Opto-electrical transfer function of a Q-CdS covered gold electrode in an aqueous 0.5 M tartrate solution of pH 14 at 297 K plotted in the complex plane (-0.7 V). The photon flux was $10^{17}/\text{cm}^2 \cdot \text{s}$ and the modulation frequency was between 0.6 rad/s and 6×10^3 rad/s. (d) The modulus plotted as a function of the frequency for the results from Figure 2.5(c) (markers) and the model (solid line).

corresponds to an anodic current at the working electrode, which means that electron tunneling from the dot to the gold electrode is followed by tunneling from the gold to the hole in the dot. In the complex plane, two semicircles are observed. The characteristic frequencies at the extrema of the imaginary part of $j(\omega)/e\Phi(\omega)$, ω_a and ω_b , are 5.8×10^3 rad/s and 2.7×10^4 rad/s, respectively. The flattening of the semicircle indicates a distribution in the rate constants for electron tunneling. The characteristic frequencies are reproducible for a given electrode, but variations of a factor of 2 can be observed with different samples. The modulus is zero when E_F is above 1.1 eV. The shape of the spectrum and the characteristic frequencies do not depend on the photon flux in the range $10^{14} < \Phi < 10^{17}$ photons/s·cm², indicating that two-photon processes are not important. Thermally activated processes or thermal release of charge carriers are not involved since the transfer function is also independent of temperature in the range of 274 K to 334 K. The absolute quantum yield was 0.01 % of the total incident light flux, not corrected for reflection. At 0.4 V the absolute quantum yield was 0.1 %. The results obtained with a Au/SAM/Q-CdS electrode in the same electrolyte are similar (Figure 2.6(a)), but the characteristic frequencies are somewhat different. These results for KCl solution can be interpreted by the simplified model presented in Figure 2.1 At high frequencies the modulus tends to zero and with decreasing frequencies the anodic signal increases. This means that only the fastest current generating process can follow the modulation of the light intensity; this is the tunneling of an electron from the occupied level of the CdS dot into the empty levels of the gold ($r_1 > r_{dec}$). At lower frequencies $|j(\omega)/e\Phi(\omega)|$ decreases with decreasing ω , indicating that the tunneling of an electron from the gold into the empty level of the CdS particle ($r_2 > r_3$) is also measured. The excited state in the CdS quantum dots decays via two consecutive tunneling processes and energy relaxation in the gold. When the gold Fermi-level is raised above 1.1 eV, *i.e.* above the occupied level of the CdS quantum dot, this gold-mediated recombination mechanism is blocked.

Figure 2.5(c) shows a complex plane plot of the opto-electrical transfer function of a Au/Q-CdS electrode in an aqueous solution of pH 14 with 0.5 M tartrate (at -0.7 V). The modulus is shown in Figure 2.5(d) as a function of the modulation frequency. The low frequency limit is a non-zero point on the real axis. A small semicircle with a characteristic frequency, ω_c , of 6 rad/s is found, followed by a second semicircle with a characteristic frequency, ω_b' , of 7×10^2 rad/s. The radius of the low frequency semicircle and ω_c depend on temperature, whereas the radius of the high frequency semicircle and ω_b' are independent of temperature. The temperature dependence indicates that ω_c corresponds to the rate of an electrochemical process, *i.e.* electron donation from the reduced species. The light intensity also affects the shape of the spectrum. At very low light

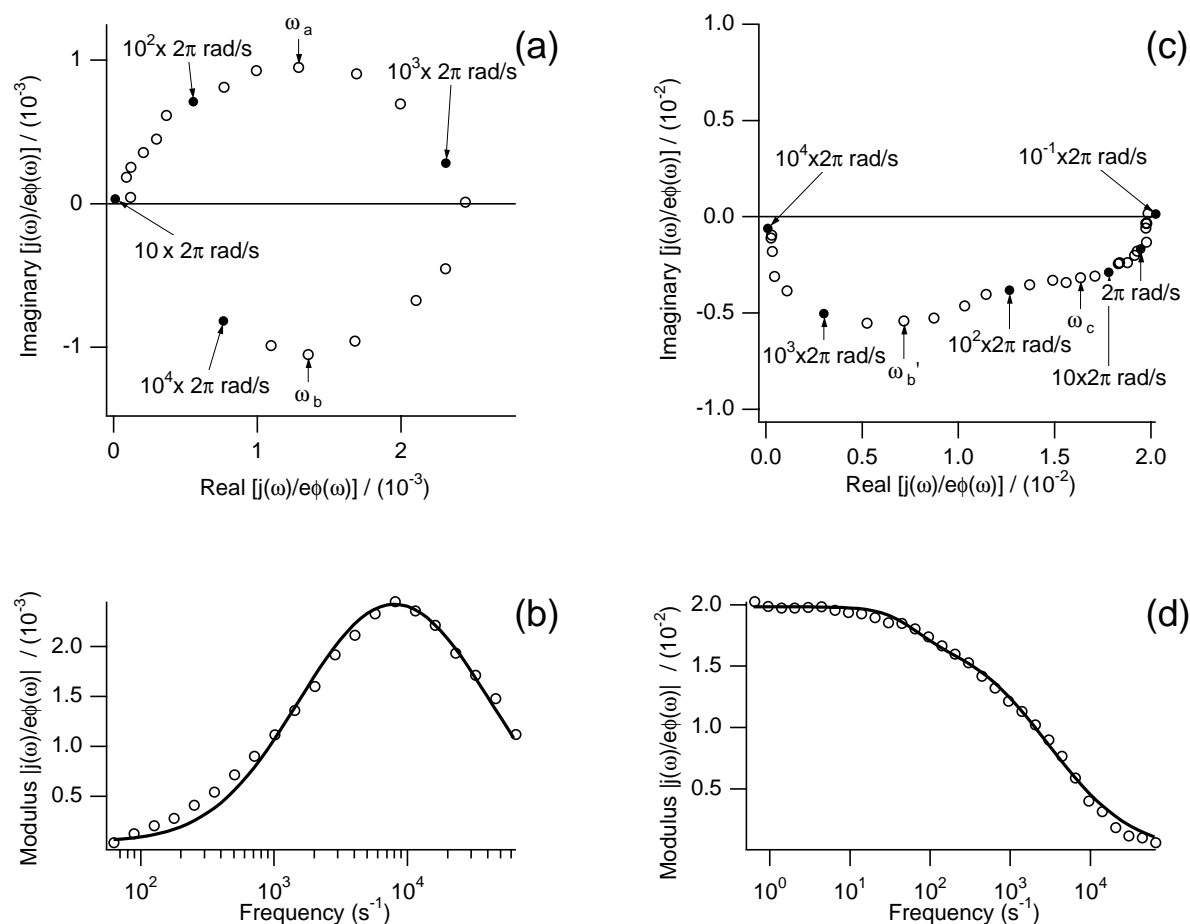


Figure 2.6. (a) Opto-electrical transfer function of a Au/SAM/Q-CdS electrode in an aqueous 1.0 M KCl solution at 297 K plotted in the complex plane (potential -0.8 V). The photon flux was $10^{17}/\text{cm}^2\cdot\text{s}$ and the modulation frequency was between 60 rad/s and 60×10^3 rad/s. (b) The modulus plotted as a function of the frequency for the results from Figure 2.6(a) (markers) and the model (solid line). (c) Opto-electrical transfer function for a Au/SAM/Q-CdS electrode in an aqueous 0.5 M tartrate solution of pH 14 at 297 K plotted in the complex plane (-0.7 V). The photon flux was $10^{17}/\text{cm}^2\cdot\text{s}$ and the modulation frequency was between 0.6 rad/s and 60×10^3 rad/s. (d) The modulus plotted as a function of the frequency for the results from Figure 2.6(c) (markers) and the model (solid line).

intensities recombination instead of electron-hole separation was observed. The opto-electrical transfer function for a Au/SAM/Q-CdS electrode exhibits two semicircles (Figure 2.6(c)); however, these are less well resolved than for the Au/Q-CdS electrode. The absolute quantum yield has increased upon adding a stabilizing agent to the electrolyte. At high frequencies the modulus of the opto-electrical transfer function (Figures 2.5(d) and 2.6(d)) is zero and with decreasing frequencies the anodic signal increases. The semicircle at the higher frequencies is temperature independent and therefore corresponds to tunneling of an electron from the occupied level of the particle into the empty levels of the gold ($r_I > r_{dec}$). The process at lower frequencies is a thermally activated electrochemical process and represents electron injection from the tartrate

into the empty level of the CdS particle; this implies that electron tunneling from the gold into the particle is slower than electron transfer from the reduced species ($r_3 > r_2$). These processes are presented in Figure 2.1.

2.3.4 Electrical Impedance Spectroscopy

Electrical impedance experiments were performed to determine the capacitance of the Au/SAM/Q-CdS/electrolyte junction and the RC -time constant of the system. Table 2.1 shows results for different systems, measured in a potential range between -1.0 V and $+0.5$ V in 1.0 M KCl (pH 7). The measured capacitance was independent of the potential. The capacitance of a bare gold electrode was $42.2 \mu\text{F}/\text{cm}^2$, in reasonable agreement with what others found for mechanically polished, clean gold electrodes.¹⁶ The capacitance of a hexanedithiol- and nonanedithiol modified gold electrode was 18.6 and $13.8 \mu\text{F}/\text{cm}^2$, respectively. A chain length dependence was also observed for thiol-modified gold electrodes.¹⁷ CdS quantum dots deposited on the SAM or on the bare gold electrode raised the capacitance of the system. The capacitance of a dithiol-modified gold electrode with a monolayer of CdS quantum dots, which is subsequently placed in a 5 mM dithiol/ethanol solution for 20 hours, was 6.4 and $7.7 \mu\text{F}/\text{cm}^2$; this is lower than the capacitance of the electrode before the second immersion in the dithiol solution. The polyphosphate capping may be replaced by dithiol molecules and/or defects in the SAM may be repaired when the electrode is re-immersed in the dithiol solution.^{18,19} The resistance of the electrolyte was 1.3Ω , and the resulting RC -time constant for these systems was 1.1×10^5 rad/s.

System	Capacitance ($\mu\text{F}/\text{cm}^2$)	$R_{el}C_{sc/el}$ (10^3 rad/s)
Au	42.2 ± 6.8	18.9
Au/CdS	55.2 ± 12.0	14.4
Au/Hex	18.6 ± 4.0	42.9
Au/Hex/CdS	21.5 ± 2.4	37.2
Au/Hex/CdS/Hex	6.4 ± 0.8	125
Au/Non	15.8 ± 3.2	50.5
Au/Non/CdS	34.7 ± 2.2	23
Au/Non/CdS/Non	7.7 ± 0.7	104

Table 2.1 Capacitances and RC -time constant of different systems, measured in the potential range from -1.0 V to 0.5 V in 1.0 M KCl (pH 7).

2.4 Discussion

The quantised CdS particles studied in this work, are adsorbed as a monolayer on gold and are assumed not to interact with each other.²⁰ The Au/Q-CdS/electrolyte system forms a Double-Barrier Tunnel Junction (see Figure 2.7). The capacitance of the interface between the gold and the particle, C_1 , is very likely determined by the gold/electrolyte and the dot/electrolyte double-layer capacitances. The polyphosphate chains may also influence this capacitance. The capacitance of the interface between the particle and the electrolyte, C_2 , is determined by the dot/electrolyte double-layer capacitance, but may also be influenced by the polyphosphate capping. j_1 and j_2 represent the photoinduced tunnel currents through the particle-gold junction and the particle-electrolyte junction, respectively. If a particle in the ground state (Q_0) is illuminated ($h\nu \geq \Delta E_{H,L} = 2.5$ eV) an electron is excited from the HOMO (H) into the LUMO (L) giving an excited state ($Q_{e,h}$), which can relax radiatively to the ground state within a nanosecond.

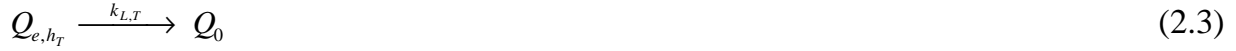


Time-resolved absorption spectroscopy on CdS suspensions has shown a photobleaching effect with a life time of 50 ms.⁹ The relatively long lifetime of this excited state in CdS can only be explained by the trapping of an electron or a hole in a localised state.²¹⁻²³ The long-lived excited state could consist of an electron in the LUMO and a trapped hole, or a trapped electron and a hole in the HOMO. Since we found that photo-electrical activity sets in when $E_F < E_{LUMO}$, we must conclude that the long-lived excited state consists of an electron in the LUMO and a trapped hole. Hence, an electron transition between a trap and the empty HOMO competes with direct exciton recombination



If the long-lived state Q_{e,h_T} arises from a sub-bandgap transition with emission of a 1.9 eV photon, it must be concluded that the hole trapping level is deep, *i.e.* far above the HOMO. An excited state with a deeply trapped hole and an electron in the LUMO has also been observed with CdSe quantum dots.²⁴ Hence, we assume that the photoelectrochemical activity is due to a

long-lived excited state with an electron in L and a hole trapped in a bandgap state (see Figure 2.7). The long-lived excited state may decay to the ground state by a LUMO-trap transition



The electron in the LUMO can tunnel into the gold leaving a positively charged particle, $Q_{h_T}^+$ (reaction (2.4)). An electron from the gold may tunnel into the empty level (trapped hole) of $Q_{h_T}^+$ (reaction (2.5)).



where $k_{L,Au}$ and $k_{Au,T}$ are tunnel rates per Q_{e,h_T} and $Q_{h_T}^+$, respectively. These rates depend strongly on the position of the Fermi level in the gold $E_{F,Au}$ with respect to the energy of the photoexcited electron and the trapped hole. Reaction 2.4 can take place when $E_{LUMO} > E_{F,Au}$, and reaction (2.5) when $E_{F,Au} \geq E_{h_T}$. It follows that recombination via the gold can only be observed when $E_{LUMO} > E_{F,Au} \geq E_{h_T}$. To account for a long-lived excited state a repulsive electrostatic force is expected between the trapped hole in the surface state and the electron in the LUMO. When S^{2-} is assumed to be the surface state, trapping of a hole gives S^{\bullet} which is negatively charged and will repel the electron in the LUMO. The trapped hole can be scavenged by tartrate, a reducing agent (reaction (2.6)).



The processes succeeding the formation of the long-lived excited state and the model electrical circuit are schematically represented in Figure 2.7. Four relaxation processes can be distinguished; direct HOMO-LUMO recombination (2.1), recombination via the surface state ((2.2) followed by (2.3)) recombination via the gold ((2.4) followed by (2.5)) and charge separation ((2.4) followed by (2.6)). The system can be described by first order differential equations involving the concentrations of the different states of the quantum dot and the tunneling rates, defined in (2.1)-(2.6).

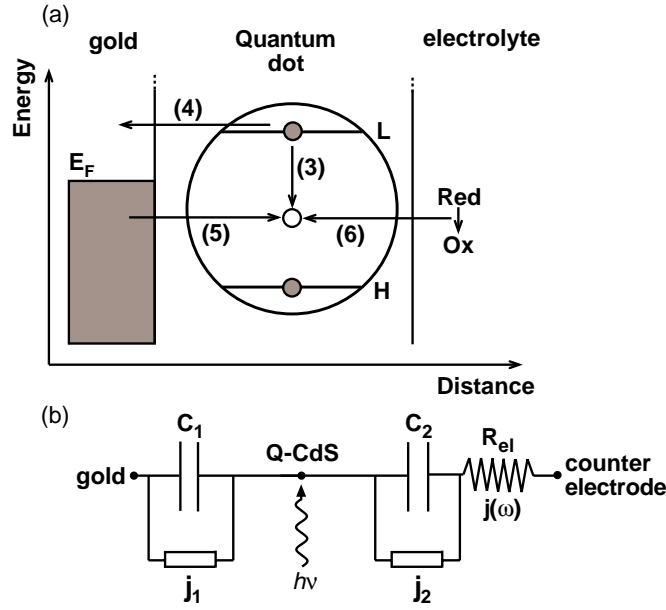


Figure 2.7 (a) Schematic representation of the Double-Barrier Tunnel Junction. The tunneling processes after formation of the long-lived excited state are indicated. (b) A scheme of the model electrical circuit. The Q-CdS covered gold is the illuminated working electrode.

$$\frac{d[Q_{e,h}]}{dt} = k_{H,L} \Phi[Q_0] - (k_{L,H} + k_{T,H})[Q_{e,h}] \quad (2.7)$$

$$\frac{d[Q_{e,h_T}]}{dt} = k_{T,H}[Q_{e,h}] - (k_{L,T} + k_{L,Au})[Q_{e,h_T}] \quad (2.8)$$

$$\frac{d[Q_{h_T}^+]}{dt} = k_{L,Au}[Q_{e,h_T}] - (k_{Au,T} + k_{R,T})[Q_{h_T}^+] \quad (2.9)$$

The total concentration of particles is equal to the sum of the concentrations of particles in the different states

$$[Q] = [Q_0] + [Q_{e,h}] + [Q_{e,h_T}] + [Q_{h_T}^+] \quad (2.10)$$

A general formula for a photogenerated tunnel current over two capacitances C_1 and C_2 in series (Figure 2.7(b)) is, according to Kirchoff's laws,

$$\gamma j_1 + (1 - \gamma) j_2 = j_{ph} + \tau_{cell} \frac{dj_{ph}}{dt} \quad (2.11)$$

in which τ_{cell} is the RC-time constant of the photoelectrochemical cell and

$$\gamma = \frac{C_2}{C_1 + C_2} \quad (2.12)$$

j_{ph} is the photocurrent measured in the external circuit. j_1 and j_2 are the currents for electron tunneling over C_1 and C_2 respectively

$$j_1 = ek_{L,Au}[Q_{e,h_T}] - ek_{Au,T}[Q_{h_T}^+] \quad (2.13)$$

$$j_2 = ek_{R,T}[Q_{h_T}^+] \quad (2.14)$$

From these general equations, expressions can be derived for the steady-state photocurrent and the opto-electrical transfer function.

2.4.1 Steady-state photocurrent

Under steady-state conditions, the photocurrent density is equal to the photoinduced tunnel current through the gold-particle junction and the particle-electrolyte junction

$$j_{ph} = \sum_N j_1 = \sum_N j_2 \quad (2.15)$$

where N is the surface concentration of particles. The decay times of the excited state to the ground state (2.1) and to the long-lived excited state (2.2) have been determined with time-resolved optical spectroscopy. Using $k_{T,H} \approx 10^7 \text{ s}^{-1}$, $k_{L,T} \approx 20 \text{ s}^{-1}$ and $k_{L,H} \approx 10^9 \text{ s}^{-1}$ from Ref. 8 and 9 and equations (2.7)-(2.10) the steady-state concentration of $Q_{h_T}^+$ is readily obtained

$$[Q_{h_T}^+] = \frac{N k_{H,L} \Phi k_{T,H} k_{L,Au}}{(k_{L,H} + k_{T,H})(k_{L,T} + k_{L,Au})(k_{Au,T} + k_{R,T})} \quad (2.16)$$

It follows from (2.14)-(2.16) that the steady-state quantum yield is then given by

$$\frac{j_{ph}}{e\Phi} = N k_{H,L} \left(\frac{k_{T,H}}{k_{L,H} + k_{T,H}} \right) \left(\frac{k_{L,Au}}{k_{L,T} + k_{L,Au}} \right) \left(\frac{k_{R,T}}{k_{Au,T} + k_{R,T}} \right) \quad (2.17)$$

The steady-state photocurrent quantum yield is independent of the photon flux. The first bracketed term of this equation is determined by intra-particle processes, direct recombination and the formation of the long-lived excited state. From the time resolved spectroscopic results it follows that the value of this part is 0.01. The second term describes the competition between tunneling from the LUMO to the gold and decay from the LUMO to the trap. Since a photocurrent was observed $k_{L,Au}$ should exceed $k_{L,T}$ and this part of the equation is close to 1. This point will be discussed in more detail further on. The third term describes the competition between tunneling from the gold to the trap and tunneling from the electrolyte to the trap. Without a hole scavenger, recombination transients are observed when $0.9 \text{ eV} > E_{F,Au} \geq 0.6 \text{ eV}$, indicating that under these conditions $k_{Au,T} \gg k_{R,T}$ and this part of the equation $\ll 1$. However, the presence of a hole scavenger results in an anodic steady-state photocurrent, indicating that for this case $k_{R,T} > k_{Au,T}$; this part then approximates to 1. According to this equation, the steady-state photocurrent quantum yield will increase upon adding a hole scavenger to the electrolyte, as has been observed in the photoelectrochemical experiments.

2.4.2 Opto-electrical transfer function

A harmonically modulated intensity is superimposed upon a background light intensity, Φ_0 , such that the total incident light intensity is defined by

$$\Phi(\omega) = \Phi_0 + \Phi_m e^{i\omega t} \quad (2.18)$$

When the tunneling rates are independent of the incident light intensity, the time-dependent concentrations can be derived from rate equations for the different states of the quantum dot. The resulting modulated photocurrent is, according to Kirchoff's laws, given by

$$j(\omega) = \frac{\gamma \sum_N j_1(\omega) + (1-\gamma) \sum_N j_2(\omega)}{1 + i\omega\tau_{cell}} \quad (2.19)$$

From equation (2.19) and the rate equations for the concentrations of the excited states, the opto-electrical transfer function is found to be

$$\frac{j(\omega)}{e\Phi(\omega)} = N \left(\frac{k_{H,L} k_{T,H}}{k_{H,L}\Phi + k_{L,H} + k_{T,H}} \right) \left(\frac{(i\omega\gamma + k_{R,T})k_{L,Au}}{(i\omega + k_{Au,T} + k_{R,T})(i\omega + k_{L,T} + k_{L,Au})} \right) \left(\frac{1}{1 + i\omega\tau_{cell}} \right) \quad (2.20)$$

At the low frequency limit equation (2.20) corresponds to the expression for the steady-state photocurrent quantum yield (2.17). This function can be plotted in the complex plane with the frequency as parameter. When $\tau_{cell} > (k_{L,T} + k_{L,Au}) > (k_{Au,T} + k_{R,T})$ and $(\gamma k_{Au,T}) > ((1-\gamma) k_{R,T})$ a semicircle is expected in the positive-positive quadrant with a characteristic frequency around $(k_{Au,T} + k_{R,T})$ and a second semicircle in the positive-negative quadrant with a characteristic frequency around $(k_{L,T} + k_{L,Au})$. At both the high and the low frequency limit the function tends to zero. Changing the ratio of capacitances only affects the amplitude of the signal, since the same tunnel junction is involved in both processes. A temperature dependence would not be expected in this case, since there are no thermally activated processes involved. When $(\gamma k_{Au,T}) < ((1-\gamma) k_{R,T})$ the function gives two semicircles in the positive-negative quadrant, with characteristic frequencies that correspond to $(k_{Au,T} + k_{R,T})$ and $(k_{L,T} + k_{L,Au})$ or τ_{cell} . Since C_1 is determined by the Helmholtz capacitance of the Au/electrolyte and the CdS/electrolyte junctions and C_2 by the CdS/electrolyte junction, C_1 and C_2 are not significantly different and hence the lower characteristic frequency corresponds to $k_{R,T}$. The relative radii of the semicircles depend on γ . The low-frequency limit is equal to the steady-state quantum yield and, at the high frequency limit, the function tends to zero. Since the electrochemical reaction is thermally activated, tunneling and electrochemical processes can be distinguished by varying the temperature.

The opto-electrical transfer function (2.20) can be fitted to the results obtained for solutions with and without an electron donor. In Figures 2.5(b,d) and 2.6(b,d) the modulus of the functions is shown versus the modulation frequency for the model and the results. A distribution in rate constants for $k_{Au,T}$ (2.5(b) and 2.6(b)) and $k_{L,Au}$ (2.5(d) and 2.6(d)) was introduced for the fitting; this point will be discussed in more detail in the next section. A comparison of the results obtained with Au/Q-CdS in the absence of an electron donor with the model shows that the IMPS spectra presented in Figures 2.5(a) and 2.6(a) correspond to excited state relaxation via the gold. The characteristic frequency of the low frequency semicircle corresponds to $k_{Au,T}$ and that of the high frequency semicircle in principle to $k_{L,Au}$. Electrical impedance experiments showed that τ_{cell} for a CdS covered gold electrode is 1.44×10^4 rad/s which corresponds to the characteristic frequency of the semicircle in the positive-negative quadrant. From this, it is clear that the high

frequency loop is determined by the RC -time constant of the electrochemical cell (τ_{cell}) which means that the tunneling from the LUMO to the gold is faster than τ_{cell} . The capacitance of the electrode could be decreased to $6.4 \mu\text{F}/\text{cm}^2$ by providing the electrode with an organic dithiol layer increasing τ_{cell} to 1.25×10^5 rad/s, but $k_{L,Au}$ still exceeds τ_{cell} .

The high frequency tunneling step gives an anodic signal, showing that the fastest process is tunneling of an electron from the LUMO of the CdS quantum dot into empty levels of the gold. Tunneling of an electron from the gold into the trapped hole in the surface state is considerably slower; this might be due to a larger average tunnel distance and a higher effective tunnel barrier height. The width of the tunnel barrier is probably determined by the polyphosphate links between the gold and the CdS quantum dots. Excited state relaxation via the substrate has not been observed before with comparable systems such as C_{60} molecules adsorbed on a metal surface.²⁵ In contrast to Q-CdS no long-lived excited state is formed in this system and exciton relaxation to the ground state occurs within nanoseconds.

When the results obtained with Au/Q-CdS in the presence of an electron donor are compared to the model, it can be concluded that the IMPS spectra in Figures 2.5(c) and 2.6(c) represent charge separation by two consecutive electron tunneling processes. In the presence of an electron donor, two semicircles in the positive-negative quadrant are obtained as shown in Figures 2.5(c) and 2.6 (c). The radius of the low frequency semicircle and the characteristic frequency are temperature dependent indicating a thermally activated process. The high frequency semicircle corresponds to tunneling of an electron from the LUMO of the CdS quantum dot to empty levels in the gold. This process is much slower in alkaline solution than in a neutral electrolyte. In alkaline solution, a CdO or Cd(OH)₂ layer is formed around the CdS quantum dot which forms an effective tunnel barrier and decreases the tunneling rate. This decrease in tunneling rate makes it possible to observe $k_{L,Au}$ instead of τ_{cell} . The fastest process is tunneling from the LUMO into the empty level of the gold (600 rad/s), leaving a positively charged particle. This is followed by the slower process, scavenging of the trapped hole by tartrate (6 rad/s). Though $k_{L,Au}$ is relatively slow, the tunneling is still faster than relaxation of the long-lived excited state (50 rad/s). Therefore, charge separation can effectively compete with excited-state relaxation within the dot. The fact that at very low light intensities, gold-mediated excited state relaxation is faster than electron-hole separation, cannot be explained by the current model for the excited state dynamics.

2.4.3 Distribution of rate constants

As mentioned before, all the semicircles representing tunneling processes are flattened, as a result of a distribution in rate constants. The rates of electron tunneling should depend strongly on the spacing between the electron donor and acceptor.²⁶ A distribution of tunnel distances will lead to a distribution of rate constants. Peter and coworkers have shown that a dispersion in the rate constants affects the opto-electrical transfer function.²⁷ A broad distribution results in depressed semicircles in the IMPS spectrum. Electron tunneling from the gold to the trapped hole, process (2.5), is observed in Figure 2.5(a), and the semicircle in the IMPS spectrum corresponding to this process is flattened. Process (2.4), electron tunneling from the LUMO of the quantum dot into the empty gold levels is faster than the RC -time of the electrochemical cell in neutral electrolyte and is therefore only considered for the system in alkaline solution. For $k_{Au,T}$, for instance, the following distance dependence is expected according to equation (1.15)

$$k_{Au,T} \propto k_0 e^{-\beta d} \quad (2.21)$$

where d is the barrier thickness and β is a constant, dependent of the barrier height. For $k_{Au,T}$, a Gaussian distribution is assumed around d , the distance between the gold surface and the trapped hole

$$G_{(s)} = \frac{1}{\sigma \times \sqrt{2\pi}} e^{-\frac{1}{2} \left(\frac{d-d_0}{\sigma} \right)^2} \quad (2.22)$$

in which σ is the width of the distribution. This distribution is caused by a dispersion in the particle-Au distance, particle size and by the fact that the trapped hole can be located anywhere on the surface of the particle. For these reasons a rather broad distribution around s_0 can be taken. For the distance between the gold surface and the centre of the particle 4 ± 1 nm is assumed. The radius of the particle is ~ 2.5 nm and taking into account a random distribution of the surface states over the surface of the particle, the tunneling distance varies from 0.5 nm to 7.5 nm. In practice, only the processes with a relatively small tunneling distance will contribute to the transfer function. The resemblance in flattening and frequency dispersion (Figures 2.5 and 2.6) confirms that the model is in reasonable agreement with the experimental data.

2.5 Conclusion

In this chapter we have shown that the excited state dynamics in CdS quantum dots adsorbed on a metal electrode can be studied with a time-resolved photoelectrochemical technique, providing additional information to time resolved spectroscopy. The energetics and the chemical nature of the surface state are elucidated. The tunneling rates can be directly determined, providing information about the tunneling sequence. By varying the temperature, tunneling and electrochemical processes can be distinguished. Though the tunneling rates are rather low, tunneling can still compete with excited state relaxation within the particle due to participation of a long-lived excited state. The low tunnel rates and the weak electronic coupling indicate that the particles are not bound to the surface by a sulfur-gold interaction, but by the stabilizing polyphosphate chains. We have seen that for the tunneling processes a distribution in rate constants has to be taken into account, which originates from variations in tunneling distance. IMPS should be widely applicable to the study of excited state dynamics in a whole range of semiconducting materials adsorbed on conducting substrates.

References and Notes

- 1 A. Henglein, *J. Phys. Chem.* **1982**, *86*, 2291-2293
- 2 L.E. Brus, *J. Chem. Phys.* **1984**, *80*, 4403
- 3 A.J. Nozik and O.I. Micic, *MRS Bulletin* february **1998**, 24-30
- 4 M. Kuno, J.K. Lee, B.O Dabbousi, F.V. Mikulec, and M.G. Bawendi, *J. Chem. Phys.* **1997**, *106*, 9869-9882
- 5 M.T. Nenadovic, M.I. Comor, V. Vasic, and O.I. Micic, *J. Phys. Chem.* **1990**, *94*, 6390-6396
- 6 L. Spanhel, M. Haase, H. Weller, and A. Henglein, *J. Am. Chem. Soc.* **1987**, *109*, 5649-5655
- 7 P. Guyot-Sionnest, and M.A. Hines, *Appl. Phys. Lett.* **1998**, *72*, 686-688
- 8 A. Henglein, *Topics in Current Chemistry* **1988**, *143*, 115
- 9 W.J. Albery, G.T. Brown, J.R. Darwent, and E. Saievar-Iranizad, *J. Chem. Soc. Faraday Trans. 1* **1985**, *81*, 1999-2007
- 10 S. Ogawa, K. Hu, F.F. Fan, and A.J. Bard, *J. Phys. Chem. B* **1997**, *101*, 5707-5711
- 11 M. Miyaki, H. Matsumoto, M. Nishizawa, T. Sakata, H. Mori, S. Kuwabata, and H. Yoneyama, *Langmuir* **1997**, *13*, 742-746
- 12 S. Ogawa, F.F. Fan, and A.J. Bard, *J. Phys. Chem. B* **1995**, *99*, 11182-11189

- 13 F. Mansfeld, S. Lin., Y.C. Lin, and H. Shih, *J. Electrochem. Soc.* **1988**, *135*, 906-907
- 14 J.R. White, and A.J. Bard, *J. Phys. Chem.* **1985**, *89*, 1947-1954
- 15 A.R. de Wit, D. Vanmaekelbergh, and J.J. Kelly, *J. electrochem. Soc.* **1992**, *139*, 2508-2513
- 16 J.A.M. Sondag-Huethorst, and L.G.J. Fokkink, *Langmuir* **1992**, *8*, 2560-2566
- 17 E. Sabatini, I. Rubinstein, R. Maoz, and J. Sagiv, *J. Electroanal. Chem.* **1987**, *219*, 365-371
- 18 T. Nakanishi, B. Ohtani, and K. Uosaki, *J. Phys. Chem.* **1998**, *102*, 1571-1577
- 19 K. Hu, M. Brust, and A.J. Bard, *Chem. Mater.* **1998**, *10*, 1160-1165
- 20 In principle, exciton diffusion from dot to dot may occur in the monolayer array. However, this process does not lead to a photoinduced current, and therefore does not have to be taken into account in our model. Transfer of individual electrons from one dot to another may also occur leading to photoinduced intermediate states not incorporated in the present model. Such processes have a considerably lower probability than tunneling involving metal and electrolyte states. The dots are separated by a distance determined by two polyphosphate capping layer. Moreover, the metal and redox electrolyte have a considerably higher density of states than the CdS quantum dots surrounding an excited dot.
- 21 A. Eychmüller, A. Hässelbarth, L. Katsikas, and H. Weller, *Ber. Bunsenges. Phys. Chem.* **1991**, *95*, 79-84
- 22 M. O'Neil, J. Marohn, and G. McLendon, *J. Phys. Chem.* **1990**, *94*, 4356-43630
- 23 M.G. Bawendi, P.J. Carroll, W.L. Wilson, and L.E. Brus, *J. Chem. Phys.* **1992**, *96*, 946-954
- 24 E. Lifshitz, I. Dag, I. Litvin, G. Hodes, S. Gorer, R. Reisfeld, M. Zelner, and H. Minti, *Chem. Phys. Lett.* **1998**, *288*, 188-196
- 25 K. Kuhnke, R.B. Becker, M. Epple, and K. Kern, *Phys. Rev. Lett.* **1997**, *79*, 3246-3249
- 26 J. Bardeen, *Phys. Rev. Lett.* **1961**, *6*, 57-59; P.V. Gray, *Phys. Rev.* **1965**, *140*, A179-186
- 27 J. Li, and L.M. Peter, *J. Electroanal. Chem.* **1986**, *199*, 1-26

Time-Resolved Photoelectrochemistry with PbS Quantum Dots Adsorbed on Gold

Abstract

The electronic structure and decay dynamics of a long-lived photoexcited state in PbS quantum dots (QD) adsorbed as a monolayer on a gold electrode were studied by a time resolved photoelectrochemical technique, Intensity-Modulated Photocurrent Spectroscopy (IMPS). By scanning the Fermi level of the gold, we found that the excited state consists of an electron in a deep trap and a hole in the HOMO. The rate constants of photoinduced electron tunneling between the dots and the electrode and between the dots and the electrolyte were determined. It was found that the trapped charge carrier has a lower tunneling probability than the free charge carrier, indicating that distance is the determining parameter for electron tunneling.

3.1 Introduction

There is a strong current interest in the optical, electrical and optoelectrical properties of metal and semiconductor nanoparticles.¹⁻⁴ Applications in electronic and optoelectronic devices have been proposed.⁵⁻⁹ The electronic structure of both ground and excited states are important for the applications. In the past decade, suspensions of semiconductor nanocrystallites have been extensively studied with optical spectroscopy.¹⁰⁻¹² Besides HOMO-LUMO recombination a sub-bandgap emission is often observed, involving a charge carrier trapped in a bandgap state.¹³⁻¹⁵ Transient absorption measurements on CdS quantum dots showed that trapping of a charge carrier can result in a long-lived excited state.¹⁶ However, with optical spectroscopy alone it is not possible to determine the electronic structure of such an excited state. The study of electron exchange between a semiconductor quantum dot and a metal electrode using a photo-electrochemical technique has been described in the previous chapter.¹⁷⁻²³ With this technique we were able to determine the electronic structure of the long-lived excited state in a CdS quantum dot (Q-CdS).

The principle of the method is explained in Figure 3.1, which shows a long-lived excited state in a quantum dot adsorbed on a gold electrode.¹⁷ Tunneling of the photoexcited electron to the metal is only possible when the metal Fermi level, E_F , is below the electron level, E_e , and an electron can only tunnel from the metal to the unoccupied state in the dot when the metal Fermi level is above the hole level, E_h . Thus, relaxation of the excited state to the ground state via

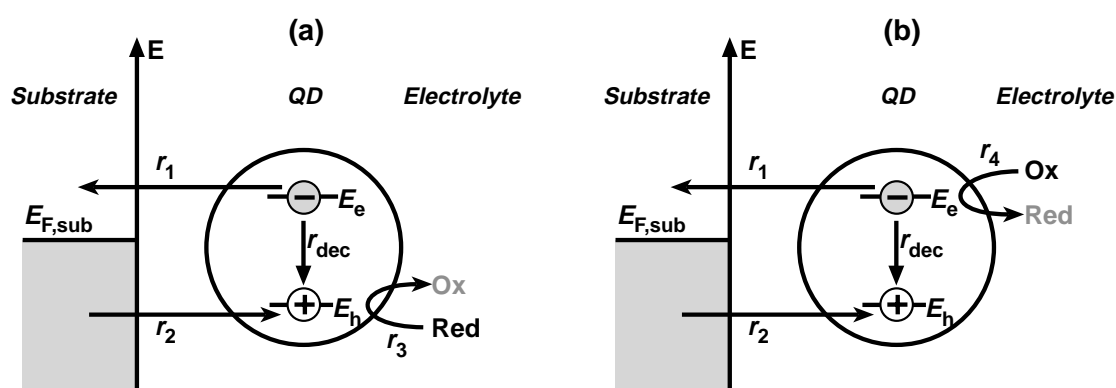


Figure 3.1 Schematic representation for electron tunneling between an adsorbed quantum dot and a metal electrode. r_1 and r_2 are tunneling events between the dot and the gold and r_3 and r_4 between the dot and the redox system in the electrolyte. When intraparticle recombination, r_{dec} is the fastest process no photoinduced current will be measured in the external circuit. When r_2 is followed by r_1 , gold-mediated recombination will be observed and when (a) r_1 is followed by r_3 or (b) r_2 by r_4 charge separation can be measured in the external circuit.

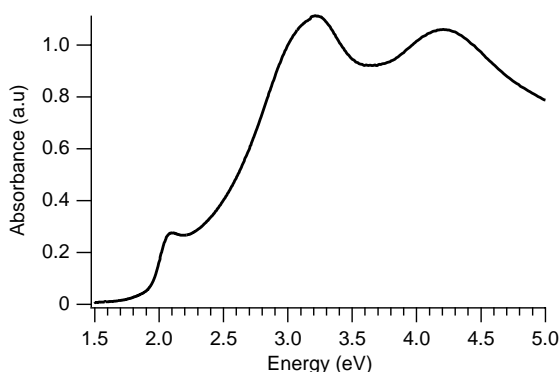


Figure 3.2 Absorption spectrum of an aqueous Q-PbS suspension. The bandgap of Q-PbS is at 2.08 eV.

interaction with the metal levels can only occur when $E_h < E_F < E_e$. By scanning E_F and measuring the photoinduced tunneling currents in the external circuit, the electronic levels of the long-lived excited state can be resolved. Moreover, by measurement of the delay between the photon absorption and the resulting photocurrent, the rates of electron tunneling between the particle and the gold may be determined.

Galena, PbS, has an optical bandgap of 0.41 eV at 300 K and can therefore be used as a long-wavelength light detector. Because the effective masses of holes and electrons in PbS are small ($m_e = m_h = 0.09 m_0$) and the semiconductor has a very high dielectric constant ($\epsilon_0 \approx 170$), one would expect strong size-quantization.^{24,25} That this is the case is clear from Figure 3.2, which shows the absorption spectrum of a Q-PbS ($d = 65 \text{ \AA}$) suspension. The onset of the optical absorbance is at 2.1 eV, and at higher energies the spectrum shows structure. The width of the absorption peaks is due to the dispersity in particle size. Despite such strong quantization, only a few papers have been published on the photoluminescence (PL) of PbS. Besides the exciton recombination peak, two maxima at lower energy with an intensity ten times that of the exciton emission are observed in the PL spectra.²⁶ The sub-gap luminescence peaks correspond to a transition from the LUMO to a bandgap state or from a bandgap state to the HOMO, indicating that at least one of the charge carriers is trapped in a bandgap energy level. The precise mechanism for sub-bandgap emission has not been resolved.

Photoelectrochemical measurements on PbS quantum dots adsorbed on a hexanedithiol covered gold electrode have been performed by Bard and coworkers.²⁷ Benzoquinone was found to scavenge electrons and tartrate to scavenge holes from the photoexcited PbS colloids.²⁸⁻³⁰ The fact that a photocurrent can be measured, means that the rate of electron tunneling between the

quantum dot and the gold electrode or a species in the electrolyte must be faster than intraparticle recombination. Hence, upon photoexcitation of PbS nanocrystals, a fraction of the excitons must decay to form a long-lived excited state, which can lead to photoinduced electron tunneling.

In this chapter the electronic structure and dynamics of the long-lived photoexcited state in Q-PbS were studied with a time-resolved photoelectrochemical technique. In the experiments a gold electrode provided with a monolayer of nanocrystalline PbS particles was used as working electrode. We found that the long-lived excited state in PbS is different from that in CdS described in the previous chapter. The rates of photoinduced tunneling were measured with Intensity-Modulated Photocurrent Spectroscopy (IMPS). With this time resolved opto-electrical technique, the direction and sequence of the tunneling steps could be determined directly and IMPS thus provides a fingerprint for the decay dynamics.

3.2 Experimental Section

The chemicals used were purchased from Aldrich and were of *pro analysi* (analytical grade) quality. In all experiments doubly distilled water was used.

PbS suspension. The aqueous Q-PbS suspension was prepared according to the method described in Reference 26. A sample of 0.044 g. polyvinylalcohol (PVA) was dissolved in 100 ml deoxygenated water. A small excess of H₂S gas (2 ml), was passed into the solution. A 1.0 ml sample of a 10 mM Pb(ClO₄)₂ solution was diluted to 50 ml and slowly added to the PVA/H₂S solution. The final deep red color was formed within several minutes. The excess H₂S was removed by slowly bubbling N₂ through the suspension. The suspension was stable for weeks when stored in a cool place in the dark.

Electrodes. The electrodes were provided with a monolayer of PbS quantum dots by immersion in the suspension and sweeping the potential between -0.4 V and -0.9 V(SCE).

Photoelectrochemistry. Photoelectrochemical experiments were performed with an EG&G 273A potentiostat and a conventional three electrode cell with a saturated calomel electrode (SCE) as reference and a platinum counter electrode. The energy corresponding to SCE is 4.68 eV below the vacuum level. The working electrode was illuminated with a Coherent Innova 90-6 argon ion laser (514.5 and 488 nm).

Intensity-Modulated Photocurrent Spectroscopy. IMPS measurements were performed with the same set-up as in chapter 2. For uniform illumination the diameter of the light spot was expanded by a Newport Beam Expander. The incident flux, 10¹⁸ photons/cm²·s for 514.5 nm light

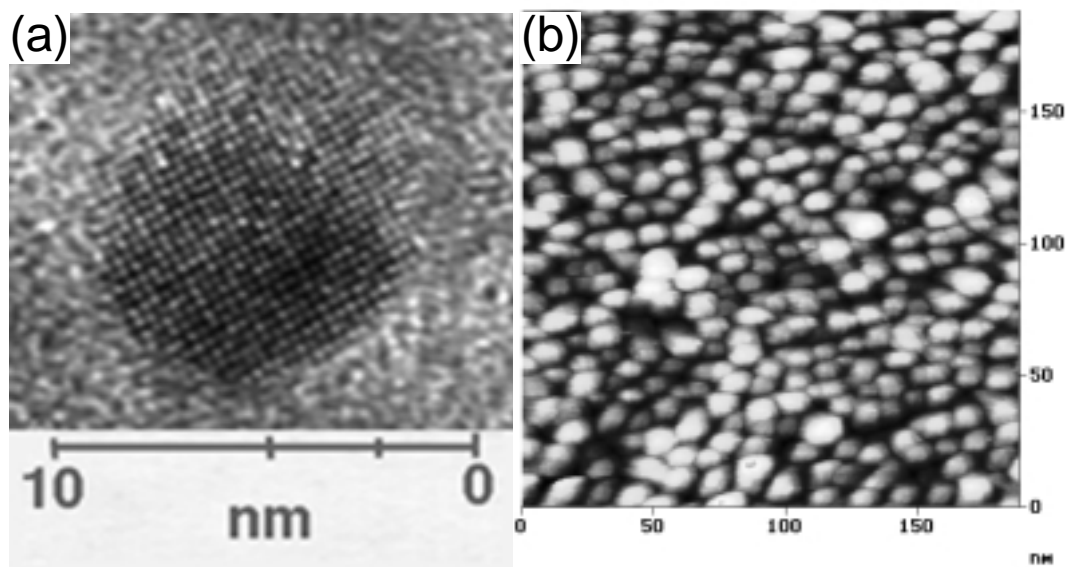


Figure 3.3 (a) HR TEM image of a single PbS quantum dot and (b) an STM image of a flame-annealed Au(111) surface covered with PbS quantum dots (bias -1.0 V, 500 pA).

and 10^{17} photons/cm²·s for 488 nm light, was determined with a silicon photodiode at the same position as the sample.

Optical Absorbance. For light absorbance measurements a Perkin-Elmer lambda 16 UV/VIS spectrophotometer was used.

HRTEM. Samples were prepared by dipping a grid with a film of amorphous carbon into the suspension. A Philips CM30 TEM was used at an operating voltage of 300 kV.

3.3 Results

3.3.1 Surface characterization

From the HR TEM analysis (Figure 3.3(a)) the nanoparticles were found to be spherical with a diameter of 65 ± 20 Å. The PbS had a rock salt structure and the crystal-plane spacing was 2.9 Å corresponding to the Pb-S bond length.³¹ The surface morphology of the PbS-covered gold was studied with STM. From Figure 3.3(b) it is clear that the whole surface is uniformly covered with quantum dots. The dots are very likely separated by the PVA capping layer. On the basis of the total amount of PbS as determined by coulometry under conditions of anodic dissolution and the particle size as revealed by TEM it could be concluded that the gold surface is covered with approximately a monolayer of PbS quantum dots.

3.3.2 Photoelectrochemistry

Figure 3.4(a) shows a current-potential plot of a Q-PbS covered gold electrode in an aqueous 1.0 M KCl solution. The electrode was illuminated with the 514.5 nm line from the argon ion laser and the light was chopped. Photocurrent transients were observed in the potential range between -0.42 V and $+0.05$ V. When the light was turned on, a cathodic current overshoot resulted, and the current decreased with time; an anodic overshoot was observed when the light was turned off. At a potential of $+0.25$ V the PbS layer is anodically dissolved in the dark.

In Figure 3.4(b) a current-potential plot is presented for the same electrode in a KCl solution with 0.2 M tartrate. A steady-state anodic photocurrent is observed between -0.4 V and $+0.05$ V, with slow transients. This steady-state anodic current indicates electron tunneling from Q-PbS to Au and from tartrate to an empty level in Q-PbS. Figure 3.4(c) shows a current-potential plot for the same electrode in an aqueous 10 mM $\text{Fe}(\text{CN})_6^{3-}$, 1 M KCl solution. A photocurrent was observed in the potential range between -0.7 V and $+0.05$ V. It was not possible to detect a photocurrent at potentials more negative than -0.7 V, because of a rapidly increasing dark current. Illumination resulted in a small cathodic overshoot, after which the current decayed

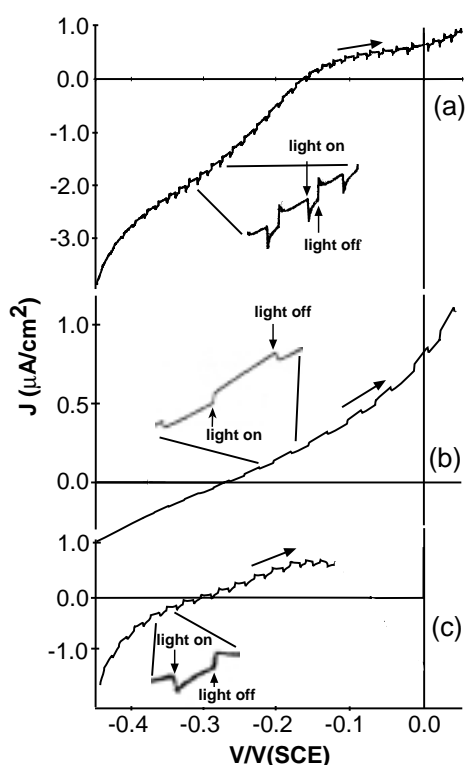


Figure 3.4 Current-potential plots of an Au/Q-PbS electrode illuminated with chopped light in (a) 1.0 M KCl, (b) 0.2 M tartrate/1.0 M KCl and (c) 10 mM $\text{Fe}(\text{CN})_6^{3-}$ /1.0 M KCl solution. The scan rate was 5 mV/sec.

to a steady-state signal; a small anodic overshoot was observed when the light was turned off. This indicates that photoexcited electrons from the Q-PbS are scavenged by $\text{Fe}(\text{CN})_6^{3-}$, and that electrons tunnel from the gold into the particle.

3.3.3 Opto-electrical transfer function

Figure 3.5(a) shows the opto-electrical transfer function, plotted in the complex plane as a function of frequency, for Au/Q-PbS in 1.0 M KCl at -0.3 V. The frequency range was 6 rad/s - 1×10^5 rad/s. At the low frequency limit the function tends to zero. The characteristic frequency of the semicircle in the neg-neg quadrant is 5×10^4 rad/s, and a second semicircle at much higher frequencies is observed in the neg-pos quadrant. This spectrum is typical for the potential range between 0.0 and -0.5 V. The modulus of the function strongly decreases when the potential is more negative than -0.4 V, as is shown in Figure 3.5(b). The transfer function is independent of the temperature in the range $293 < T < 332$ K. The wavelength of the incident light does not affect the shape of the spectrum for $h\nu > E_{L-H}$. The IMPS data can be explained by the model presented in Figure 3.1. At high modulation frequencies the tunneling processes cannot follow the light modulation, but when the frequency is decreased a cathodic signal develops. This means that the fastest step is electron tunneling from the gold to the particle (r_2 in Figure 3.1). We are not able to measure the rate of this tunneling process, but it is larger than 1.2×10^5 rad/s. When the frequency is further decreased the function goes to zero, indicating a slower anodic process. This slower process is tunneling of the photoexcited electron from the particle into the gold (r_1 in Fig. 3.1). The transfer function reflects the excited state relaxation via the gold. When E_F is scanned above 0.4 eV, the modulus of the

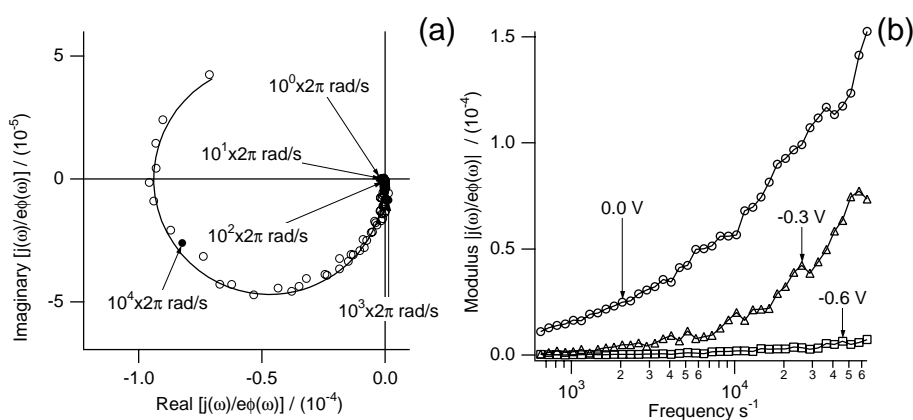


Figure 3.5 (a) Optoelectrical transfer function of a Au/Q-PbS electrode, measured at -0.3 V, in a 1.0 M KCl solution plotted in the complex plane. The frequency was modulated between 0.6 - 6×10^4 rad/s. (b) The modulus of the function measured at different potentials as a function of the frequency.

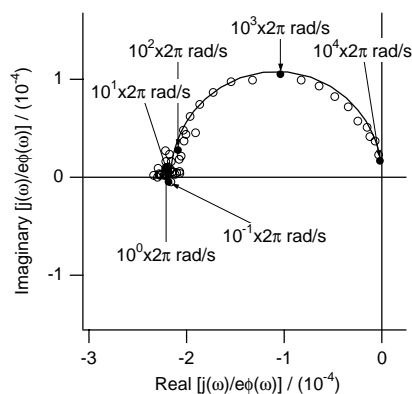


Figure 3.6 Optoelectrical transfer function of a Au/Q-PbS electrode, measured at -0.3 V, in 10 mM $\text{Fe}(\text{CN})_6^{3-}$ / 1.0 M KCl solution plotted in the complex plane. The frequency was modulated between 0.6 rad/s - 6×10^4 rad/s.

function rapidly decreases. This indicates that the energy of the excited electron is at around 0.4 eV. When the Fermi level is above this level, photoinduced electron transfer from the particle to the gold becomes impossible.

The optoelectrical transfer function of Au/Q-PbS in a 1.0 M KCl/ 10 mM $\text{Fe}(\text{CN})_6^{3-}$ solution at -0.3 V is presented in Figure 3.6. The frequency was modulated in the range 0.6 rad/s - 6×10^4 rad/s. At the high frequency limit the function goes to zero. The characteristic frequency of the semicircle in the neg-neg quadrant is 6×10^3 rad/s. A cathodic signal develops when the frequency is decreased, and at the low frequency limit the function gives a point on the negative real axis, corresponding to a steady-state cathodic photocurrent. This current is caused by electron tunneling from the gold to an empty level in the particle (r_2) and transfer of the photoexcited electron from the particle to a $\text{Fe}(\text{CN})_6^{3-}$ ion (r_4). Since only one semicircle is observed, the tunneling rate constants are of the same order of magnitude and therefore cannot be resolved.

3.4 Discussion

Anodic dissolution of intrinsic bulk PbS in the dark takes place at -0.15 eV.³² Since the hole and electron effective masses are the same in PbS, the HOMO and LUMO should shift symmetrically as the particle size decreases. The HOMO-LUMO transition of PbS particles with a diameter of 65 Å corresponds to an energy of 2.08 eV. From this it can be estimated that the HOMO is located at around -1.2 eV and the LUMO at around 0.9 eV.

The PVA capped PbS quantum dots are adsorbed as a monolayer on the gold electrode. An electron can be excited from the HOMO (H) to the LUMO (L) when the electrode is illuminated ($h\nu \geq \Delta E_{H,L} = 2.08$ eV). This primary exciton can recombine in the picosecond time domain³³, leaving a particle in the ground state, Q_0 (reaction (3.1)).



The fact that a photoinduced current is observed, while LUMO-HOMO recombination is very fast, indicates that a long-lived excited state can be formed after photon absorption. Since we found that photoelectrochemical activity sets in when $E_F < 0.4$ eV, and the LUMO in PbS is located at 0.9 eV, we must conclude that this long-lived excited state consists of an electron in a deep bandgap state and a hole in the HOMO. Reaction (3.2) represents the trapping of an electron in a bandgap state, which gives a long-lived excited state, $Q_{e_T,h}$, having less energy than the primary exciton.



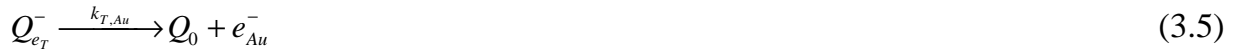
This trapped electron can recombine with the hole in the HOMO, giving a particle in the ground state (reaction (3.3)).



In the luminescence spectrum of a PVA capped PbS suspension, a broad band was observed between 1.55 and 1.24 eV.²⁶ In view of our conclusion that the long-lived state consists of a deeply trapped electron and an empty HOMO, we suggest that the sub-gap emission corresponds to a radiative transition from the trap to the empty HOMO. To observe an electrical signal in the external circuit, one of the tunnel processes between the gold and the dot must be faster than intraparticle recombination. The rate constants for electron tunneling between the dot and the electrode were determined by IMPS. The faster process is electron tunneling from the gold to the unoccupied level in the HOMO (reaction (3.4)), resulting in a negatively charged particle, $Q_{e_T}^-$.



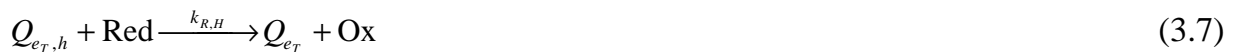
The rate constant for this process, $k_{au,H}$, exceeds 1.2×10^5 rad/s. Hence, the long-lived excited state should have a lifetime at least of the order of microseconds. The trapped electron can subsequently tunnel into empty levels in the gold.



This tunneling process can only take place when the gold Fermi level is below the energy level of the trapped electron. When the electrons, trapped in the bandgap states, are not removed by the electrolyte the photocurrent flow will stop when E_F is above the electron level. Alternatively, the trapped electron can be removed by an oxidizing agent in the electrolyte, leaving a particle in the ground state,



The photoelectrochemical experiments in which an oxidizing agent was present in the electrolyte showed that a cathodic photocurrent is observed at energies higher ($E_F < 0.7$ eV) than in the absence of an oxidizing agent ($E_F < 0.4$ eV). In this case, the electron trapped in the bandgap state is removed and a photocurrent with a steady state component was observed. Alternatively, the hole in the HOMO can be scavenged by a hole scavenger or reducing agent in the electrolyte,



When the hole in the HOMO is removed by a reducing agent, an electron is present in the particle. This electron can only tunnel into the gold; for this to occur the Fermi level of the gold must be below the bandgap state in which the electron is trapped. A photocurrent onset was observed at the same potential as for the case in which no redox couple was used, confirming that the bandgap state is located at around 0.4 eV.

An expression for the steady-state photocurrent and the opto-electrical transfer function can be derived, using the differential equations describing generation and decay of excited states as was done in the previous chapter for Q-CdS on gold. The tunneling current through the capacitance of the interface between the dot and the gold, C_1 , is defined as

$j_1 = e(k_{T,Au}[Q_{e_r}] - k_{Au,H}[Q_{e_r,H}])$. C_1 is determined by the double layer capacitances of the gold/electrolyte and dot/electrolyte interfaces. The tunneling current through C_2 , the capacitance of the interface between the dot and the electrolyte, is $j_2 = ek_{R,H}[Q_{e_r,h}]$ in the presence of a reducing agent or $j_2 = -ek_{T,O}[Q_{e_r}]$, in the presence of an oxidizing agent. C_2 is determined only by the double layer capacitance of the dot/electrolyte interface.

3.4.1 Steady-State Photocurrent

The total steady-state tunneling current, measured in the external circuit, is equal to the photoinduced tunneling current through the gold/particle and the particle/electrolyte junction. In the presence of an oxidizing agent ($k_{R,H}=0$ and $k_{T,O} \neq 0$), the steady state photocurrent quantum yield is given by

$$\frac{j_{ph}}{e\Phi} = Nk_{H,L} \left(\frac{k_{L,T}}{k_{L,H} + k_{L,T}} \right) \left(\frac{-k_{T,O}k_{Au,H}}{(k_{T,H} + k_{Au,H})(k_{T,Au} + k_{T,O})} \right) \quad (3.8)$$

(I)
(II)

The function is independent of the light flux. N is the surface concentration of particles. Term I is controlled by intraparticle processes, direct exciton recombination ($k_{L,H} \approx 10^{11} \text{ s}^{-1}$)¹³ and the trapping of the electron in a localized state. Term II is determined by the rate constants of the tunneling processes between the gold and the particle, and the particle and the electrolyte. Values for $k_{L,T}$ and $k_{T,H}$ are not known; however, it is clear that $k_{Au,H}$ must exceed $k_{T,H}$ since a photocurrent is observed. $k_{T,O}$ depends on the concentration of the oxidizing agent. When no oxidizing agent is present, recombination transients are observed when $0.4 \text{ eV} > E_F$, indicating that $k_{T,Au} > k_{T,O}$. In the presence of an oxidizing agent a cathodic steady-state current is observed indicating that $k_{T,O} > k_{T,Au}$.

3.4.2 Optoelectrical transfer function

The working electrode is illuminated with a background light intensity, upon which a harmonically modulated intensity is superimposed. The time-dependent concentrations of the different types of excited states follow from the rate equations. It is assumed that the tunneling

rate constants are independent of the light intensity. The transfer function is derived using Kirchoff's laws,

$$\frac{j(\omega)}{e\Phi(\omega)} = A \frac{\gamma k_{Au,H} (k_{T,Au} - B) + (1 - \gamma)(k_{R,H}B - k_{T,O} k_{Au,H})}{B(i\omega + k_{T,H} + k_{Au,H} + k_{R,H})} \quad (3.9)$$

in which $A = \frac{k_{L,T}k_{H,L}N}{(k_{H,L}\Phi + k_{L,H} + k_{L,T})(1 + i\omega\tau_{cell})}$, $B = (i\omega + k_{T,Au} + k_{T,O})$ and $\gamma = \frac{C_2}{C_1 + C_2}$.

Prefactor A is determined by intra-particle processes and τ_{cell} , the RC time constant of the system. In the low frequency limit, equation (3.9) corresponds to equation (3.8), the expression for the steady state photocurrent. This function can be plotted in the complex plane with the frequency as parameter. Since C_1 is determined by the double layer capacitances of both the gold/electrolyte and the PbS/electrolyte junctions and C_2 only by the latter, these capacitances are not significantly different. The shape of the optoelectrical transfer function is therefore mainly determined by the tunneling rate constants and the function is consequently a fingerprint for the decay dynamics. For example, when $k_{T,O} = k_{R,H} = 0$ and $\tau_{cell} > (k_{T,H} + k_{Au,H}) > k_{T,Au}$, semicircles in the neg-pos quadrant and in the neg-neg quadrant are expected with characteristic frequencies around $(k_{T,H} + k_{Au,H})$ and $(k_{T,Au})$, respectively. At the high and the low frequency limit, the function goes to zero. This function then corresponds to exciton decay via the gold levels. Otherwise, when $k_{Au,H} > k_{R,H}$ and $k_{T,O} > k_{T,Au}$ one semicircle or two semicircles in the neg-pos quadrant will be expected, depending on the ratio of the capacitances and rate constants. This function corresponds to charge separation via two steps; electron transfer from the gold to the particle and from the particle to the electrolyte.

The opto-electrical transfer function can be fitted to the IMPS results. In Figure 3.7 Bode plots are shown for the experimental results with an indifferent electrolyte solution (a) and a solution with an electron scavenger (b); the fits to equation (3.9) are also shown. The characteristic frequency of the low frequency semicircle corresponds to $k_{T,Au}$ and that of the high frequency semicircle to the RC time constant of the system, indicating that tunneling from the gold into the particle is faster than τ_{cell}^{-1} . The function for the system with an electron scavenger represents charge separation by two consecutive tunneling processes. Since only one semicircle was observed, the tunneling rate constants for these processes could not be resolved, but the order of magnitude can be indicated.

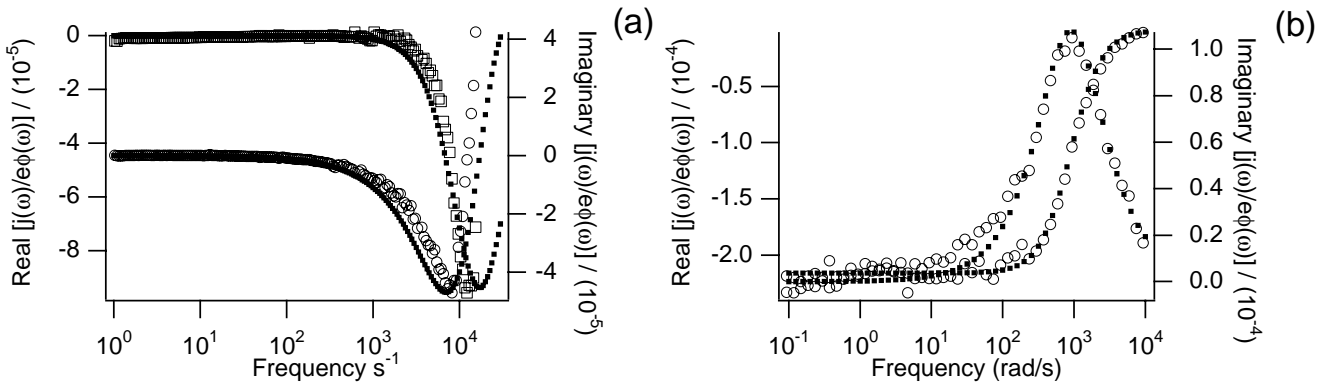


Figure 3.7 Bode plots of a Au/Q-PbS electrode in (a) 1.0 M KCl and (b) 10 mM $\text{Fe}(\text{CN})_6^{3-}$ /1.0 M KCl solution for the real (open squares) and the imaginary (circles) parts of the optoelectrical transfer functions shown in Figures 3.5 and 3.6 and the fits (solid squares).

We have shown that the long-lived excited state in PbS consists of a trapped electron and a hole in the HOMO. The fastest tunneling process is electron transfer from the gold to the hole in the HOMO. In the previous chapter we have shown that the long-lived excited state in CdS consists of a trapped hole and an electron in the LUMO. In this system the fastest tunneling process is electron transfer from the LUMO of the particle into the gold. The results of both of these studies indicate that free charge carriers have a higher tunneling rate constant than trapped charge carriers. The tunneling rate is defined by^{34,35}

$$k = k_0 e^{-\beta d} \quad (3.10)$$

where d is the tunneling distance, k_0 is the tunneling rate for the dot in a van der Waals contact with the metal, and

$$\beta = \frac{2\sqrt{2mV_0}}{\hbar} \quad (3.11)$$

where m is the rest mass of the electron and V_0 the tunneling barrier height. The main contribution to k comes from the exponential term. Basically, the electron tunneling rate depends on two parameters: the barrier height, V_0 , and the distance, d . The fastest process in CdS is the tunneling process with the smaller tunnel barrier, namely electron tunneling from the LUMO of the particle into the gold. Although the tunnel barrier for tunneling from the trapped electron on the PbS particle into the gold is smaller than for tunneling from the gold into the HOMO of the PbS QD, the latter process is faster. This means that the tunneling distance plays a more important role

than the barrier height for the tunneling probability. Free charge carriers have a higher tunneling probability because they are delocalized over the particle and tunnel at the most favourable tunneling distance. The trapped charge carriers are randomly distributed in the particle or on the particle surface, and consequently have a statistically larger average tunneling distance, resulting in a lower tunneling coefficient.

3.5 Conclusion

We have shown in this chapter that the energetics and decay of the long-lived excited state in PbS quantum dots adsorbed on a metal electrode can be studied by time-resolved photoelectrochemistry methods. Although the tunneling rates are slow, tunneling can still compete with intraparticle recombination, due to the existence of a long-lived excited state. With IMPS, the tunneling sequence of excited state relaxation via the gold electrode has been resolved, showing that tunneling involving a delocalized carrier in the dot is faster than tunneling involving a localized electron level, irrespective of the barrier height.

References

- 1 R.P. Andres, J.D. Bielefeld, J.I. Henderson, D.B. Janes, V.R. Kolagunta, C.P. Kubiak, W.J. Mahoney, and R.G. Osifchin, *Science* **1996**, 273, 1690-1693
- 2 U. Banin, Y. Cao, D. Katz, and O. Millo, *Nature* **1999**, 400, 542-544
- 3 R.P. Andres, T. Bein, M. Dorogi, S. Feng, J.I. Henderson, C.F. Kubiak, W. Mahoney, R.G. Osifchin, and R. Reifengerger, *Science* **1996**, 272, 1323-1325
- 4 M. Nirmal, B.O. Dabbousi, M.G. Bawendi, J.J. Macklin, J.K. Trautman, T.D. Harris, and L.E. Brus, *Nature* **1996**, 383, 802
- 5 M. Kastner, *Nature* **1997**, 389, 667-668
- 6 M. Kastner, *Phys. Today* **1993**, 24-31
- 7 D.L. Klein, R. Roth, A.K.L. Lim, A.P. Alivisatos, and P.L. McEuen, *Nature* **1997**, 389, 699-701
- 8 D.C. Glatti, *Nature* **1998**, 393, 516-517
- 9 A.P. Alivisatos, *MRS Bulletin February* **1998**, 18-23
- 10 M. Kuno, J.K. Lee, B.O. Dabbousi, F.V. Mikulec, and M.G. Bawendi, *J. Chem. Phys.* **1997**, 106, 9869-9882
- 11 A.J. Nozik, and O.I. Micic, *MRS Bulletin February* **1998**, 24-30

- 12 A. van Dijken, A.H. Janssen, M.H.P. Smitsmans, D. Vanmaekelbergh, and A. Meijerink, *Chem. Mater.* **1998**, *10*, 3512-3520
- 13 P. Guyot-Sionnest, M. Shim, C. Matranga, and M. Hines, *Phys. Rev. B.* **1999**, *60*, R2181-R2184
- 14 L. Spanhel, M. Haase, H. Weller, and A. Henglein, *J. Am. Chem. Soc.* **1987**, *109*, 5649-5655
- 15 M.G. Bawendi, P.J. Carroll, W.L. Wilson, and L.E. Brus, *J. Chem. Phys.* **1992**, *96*, 946-954
- 16 W.J. Albery, G.T. Brown, J.R. Darwent, and E. Saievar-Iranizad, *J. Chem. Soc. Trans. I* **1985**, *81*, 1999-2007
- 17 E.P.A.M. Bakkers, E. Reitsma, J.J. Kelly, and D. Vanmaekelbergh, *J. Phys. Chem. B* **1999**, *103*, 2781-2788
- 18 S.G. Hickey, and D.J. Riley, *J. Phys. Chem. B* **1999**, *103*, 4599-4602
- 19 P. Drouard, S.G. Hickey, and D.J. Riley, *Chem. Commun.* **1999**, 67-68
- 20 S. Ogawa, F.F. Fan, and A.J. Bard, *J. Phys. Chem. B* **1995**, *99*, 11182-11189
- 21 K. Hu, M. Brust, and A.J. Bard, *Chem. Mater.* **1998**, *10*, 1160-1165
- 22 T. Torimoto, S. Nagakubo, M. Nishizawa, and H. Yoneyama, *Langmuir* **1998**, *14*, 7077-7081
- 23 W.J. Albery, P.N. Bartlett, and J.D. Porter, *J. Electrochem. Soc.* **1984**, 2892-2900
- 24 H. Kanazawa, and S. Adachi, *J. Appl. Phys.* **1998**, *83*, 5997-6001
- 25 O. Madelung (editor), *Landolt-Börnstein* **1988**, III-17, 35-194
- 26 S. Gallardo, M. Gutierrez, A. Henglein, and E. Janata, *Ber. Bunsenges. Phys. Chem.* **1989**, *93*, 1080-1090
- 27 S. Ogawa, K. Hu, F.F. Fan, and A.J. Bard, *J. Phys. Chem. B* **1997**, *101*, 5707-5711
- 28 H. Miyoshi, M. Yamachika, H. Yoneyama, and H. Mori, *J. Chem. Soc. Far. Trans.* **1990**, *86*, 815-818
- 29 T. Torimoto, T. Sakata, H. Mori, and H. Yoneyama, *J. Phys. Chem.* **1994**, *98*, 3036-3043
- 30 T. Torimoto, H. Uchida, T. Sakata, H. Mori, and H. Yoneyama, *J. Am. Chem. Soc.* **1993**, *115*, 1874-1880
- 31 R. Rossetti, R. Hull, J.M. Gibson, and L.E. Brus, *J. Chem. Phys.* **1985**, *83*, 1406-1409
- 32 A.P. Davis, and C.P. Huang, *Langmuir* **1991**, *7*, 803-808
- 33 M.T. Nenadovic, K.I. Comor, V. Vasic, and O.I. Micic, *J. Phys. Chem.* **1990**, *94*, 6390-6396
- 34 E.E. Polymeropoulos, *J. Appl. Phys.* **1977**, *48*, 2404-2407
- 35 M. Sugi, T. Fukui, and S. Lizima, *Appl. Phys. Lett.* **1975**, *10*, 559-561

Distance Dependent Electron Transfer in Gold/Spacer/Q-CdSe-Assemblies

Abstract

Colloidal CdSe quantum dots were chemisorbed on a gold electrode using a variety of Self-Assembled Monolayers (SAMs) consisting of dithiols and rigid disulfides. After absorption of a supra-bandgap photon, a long-lived excited state was formed in the quantum dot; this state can decay by electron tunneling via the gold. The rate of photoinduced tunneling was measured directly by Intensity-Modulated Photocurrent Spectroscopy (IMPS), and its distance dependence was studied using rigid SAMs, separating the Q-CdSe and Au. The tunneling rate was found to depend exponentially on the distance, with a decay length of 2 Å.

4.1 Introduction

Semiconductor and metal quantum dots (QDs) have attracted much attention in the past decade due to their interesting size-dependent optical and electronic properties. Potential applications of nanocrystallites are in opto-electrical or electrical devices such as light-emitting diodes or single-electron transistors.¹⁻⁶ Much effort has been devoted to the control and improvement of the chemical and physical properties of individual particles and arrays of these dots.⁷⁻¹¹ The particles can be attached to metal surfaces using a Self-Assembled Monolayer (SAM) of difunctional linking molecules to form (ordered) two or three-dimensional structures.¹²⁻¹⁶

Intramolecular electron transfer in large (bio)molecules and organized structures is an important topic in current research. The relationship between tunneling rates and distance is usually studied by either synthesizing a series of analogous organic molecules with different donor-acceptor distances or by using biochemical molecules with different intramolecular donor-acceptor spacings.¹⁷⁻²⁴ Electroactive SAMs with redox centers at a controlled distance from the electrode are also convenient systems because the transfer kinetics can be studied as a function of both overpotential and temperature.²⁵⁻²⁸ It is, however, difficult to find a system in which the distance dependence of electron transfer can be studied, independent of changes in the Gibbs free energy, ΔG^0 , the reorganization energy, λ , of the reaction centres, or the conductivity of the molecule. Another problem is that, often, the transfer rate is determined indirectly by measurement of the emission decay; quenching mechanisms other than electron transfer might be introduced by a chemical change of the system.

We have developed a direct method to study the distance dependence of electron tunneling that avoids the problems described above. A monolayer of quantum dots is chemisorbed on an organic SAM on a gold electrode, forming a Double-Barrier Tunnel-Junction.²⁹⁻³³ The Au/SAM/QD system is used as a photoelectrode in a three-electrode photoelectrochemical cell. With Intensity-Modulated Photocurrent Spectroscopy (IMPS) we are able to measure the tunneling rates of photoexcited charge carriers between the particle and the gold electrode.

In this work we have studied electron tunneling as a function of the distance between CdSe quantum dots and a gold electrode. To vary this distance, we have used two classes of spacers: rigid and non-rigid molecules. In addition, an Ohmic contact was established by epitaxial electrodeposition of isolated QDs on gold. After absorption of a photon with an energy larger than the band gap, a long-lived excited state can be formed, if the hole from the HOMO or the electron from the LUMO is trapped in a localized bandgap state (see Figure 4.1). Then, excited

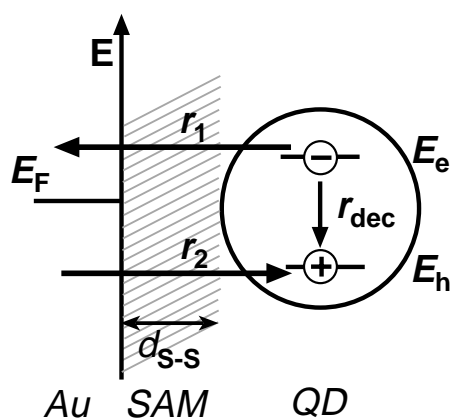


Figure 4.1 Schematic representation of the tunneling processes between a semiconductor quantum dot and a metal electrode after the formation of a long-lived excited state. When electron tunneling from the particle to the gold, r_1 , or tunneling from the gold to the particle, r_2 , is faster than intraparticle decay, r_{dec} , a photoinduced current can be measured in the external circuit. Process r_1 can only occur when the gold Fermi level, E_F , is below the electron level and process r_2 can only take place when E_F is above the hole level.

state decay via electron tunneling to and from the metal may compete with intraparticle decay. Process r_1 , electron tunneling from the particle to the gold, can only occur when the gold Fermi level, E_F , is below the electron level, E_e . Process r_2 , tunneling from the gold to the hole in the particle, can only occur when E_F is above the hole level, E_h . Using time-resolved photoelectrochemistry, the rates of individual electron transfer steps can be measured, and by scanning E_F the electronic structure of a long-lived excited state can be revealed. We show that a long-lived excited state in Q-CdSe consists of a hole trapped in a deep bandgap state and an electron in the LUMO. The distance dependence of photoinduced electron transfer was measured in the range 3 Å to 12 Å.

4.2 Experimental Section

The chemicals used were of *pro analysi* quality (analytical grade) from Merck. High-purity water (18 MΩ/cm) was used to prepare the solutions. The experiments were performed at room temperature, unless otherwise stated. All manipulations involving bis-trimethylsilyl-selenium, $(\text{TMS})_2\text{Se}$, were carried out in a nitrogen-filled glovebox.

Q-CdSe Suspension. The Q-CdSe suspension was prepared according to Reference 33. A sample of 16.7 g. of the surfactant bis(2-ethylhexyl)sulfosuccinate (AOT; see Figure 4.2) was purified by dissolving it in petroleum ether, filtered to remove particles, evaporated to dryness,

and subsequently redissolved in 650 ml heptane; deoxygenated water (2.15 ml) was then added. A sample of 0.56 ml of a 1.0 M $\text{Cd}(\text{ClO}_4)_2$ aqueous solution was added, and the mixture was stirred magnetically to form an optically homogeneous microemulsion. A sample of 50 ml of a 0.93 mM $(\text{TMS})_2\text{Se}$ heptane solution was added quickly and an orange color developed. The ratio $W=[\text{H}_2\text{O}]/[\text{AOT}]$ controls the size of the colloidal crystallites. The suspension was evaporated to dryness and redissolved in heptane; this suspension was stable for months. TEM measurements showed that the resulting crystalline CdSe quantum dots were spherical and had the zinc blende structure.

Organic Spacer Compounds. 1,4-Dithiane (**1**), was purchased from Lancaster Synthesis. The organic disulfide compounds, 4,4'-(tetrahydro-4H-thiopyran-ylidene) (**2**), 4-(tetrahydro-4H-thiopyran-4-cyclohexylidene-4'-ylidene)tetrahydro-4H-thiopyran (**3**), 4-(cyclohexylidene) tetrahydro-4H-thiopyran (**7**), and 4-(4-(cyclohexylidene-cyclohexylidene)tetrahydro-4H-thiopyran (**8**) as represented in Figure (4.2) were prepared and purified as described elsewhere.³⁴ The intramolecular S-S distance, $d_{\text{S-S}}$, determined either with single crystal X-ray diffraction or *ab initio* SCF MO (RHF/6-31G*) calculations³⁵ is given in Figure (4.2). 1,3-Propanedithiol (**4**) and 1,6-Hexanedithiol (**5**) were purchased from Fluka. 1,9-Nonanedithiol (**6**) was obtained from Aldrich.

Gold Samples. Evaporated gold films on borosilicate glass from Metallhandel Schröer ($A=1 \text{ cm}^2$) were annealed by heating in a hydrogen flame and quenching under argon; gold grains were formed with a typical diameter of 1 μm with atomically flat Au(111) surfaces. Self-Assembled Monolayers were prepared by immersing the gold film in a 5mM dithiol/ethanol or

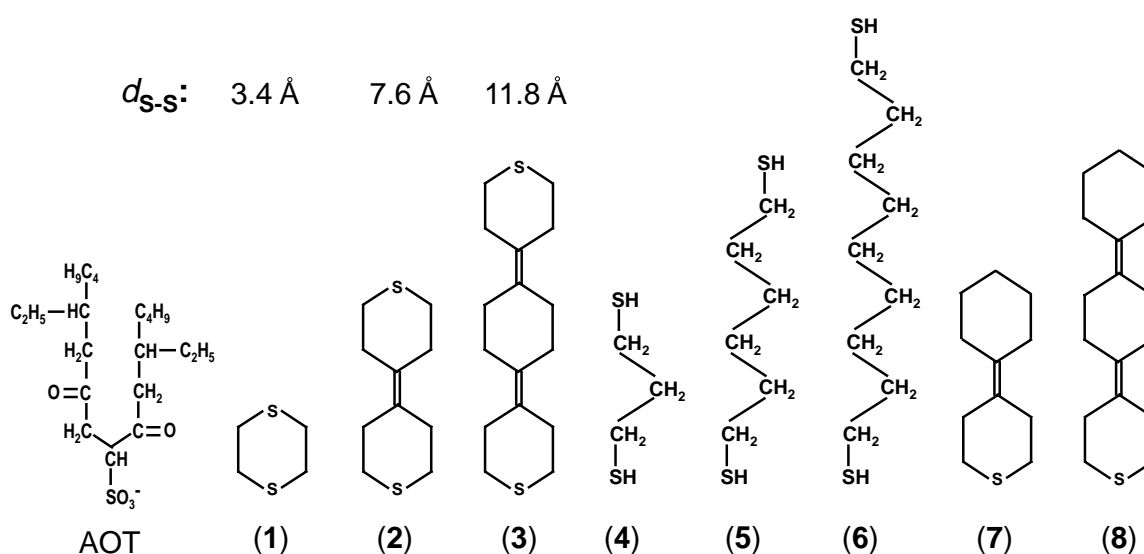


Figure 4.2 The organic compounds used for the formation of Self-Assembled Monolayers (SAM) and AOT, a capping molecule for the stabilization of the Q-CdSe colloids.

saturated disulfide/ethanol solution for 1 week at 50° C. The samples were subsequently rinsed with ethanol to remove the excess dithiol/disulfide from the surface and dried under a dry nitrogen flow. CdSe quantum dots were deposited on the Au/SAM electrode by immersion in the suspension for 1 week. The samples were rinsed with heptane to remove the excess particles.

Galvanostatically Deposited CdSe. Epitaxially-oriented quantum dots were electro-deposited on hydrogen-flame-annealed Au(111) samples as described in the literature.³⁶⁻³⁸ The CdSe dots were deposited cathodically from an unstirred 50 mM Cd(ClO₄)₂/15 mM Se DMSO solution at 120°C in a two electrode electrochemical cell. A constant current density of 0.1 mA·cm⁻² was applied for 7-20 s. After deposition, the working electrode was rinsed first with hot DMSO (140°C), then with ethanol, and dried under an argon flow. The size of the dots was controlled by the current density and the deposition time. AFM/STM experiments showed that the islands were uniformly distributed over the surface and their size could be estimated.

Photoelectrochemistry. Photoelectrochemical experiments were performed with an EG&G PAR 273A potentiostat and a conventional three electrode cell with a saturated calomel electrode (SCE) as reference and a platinum counter electrode. All potentials and energies are given with respect to SCE, which is 4.68 eV below the vacuum level. The working electrode was illuminated with a 450 W Oriel Xenon lamp through a quartz window and a 10 cm quartz water filter.

Cyclic Voltammetry. Experiments were performed in the three electrode electrochemical cell described above using an unstirred 10 mM K₄Fe(CN)₆/1.0 M Na₂SO₄ electrolyte solution. The scan rate was 100 mV/s.

STM/AFM. STM images were obtained in ambient air (40 % humidity) with a Nanoscope III (Digital Instruments, Santa Barbara, CA) with an electrochemically etched Pt/Ir tip. AFM images of the electrodeposited CdSe on gold were obtained under ambient conditions in tapping mode with a tapping mode tip, provided by Digital Instruments. The SAMs on gold were studied in the contact mode with an oxide-sharpened silicon nitride tip ($k= 0.12$ N/m), also provided by Digital Instruments.

Intensity-Modulated Photocurrent Spectroscopy. IMPS experiments were performed with an EG&G PAR 283 potentiostat and a Solartron 1255 FRA. A Coherent Innova 90 Argon ion laser was used as light source (457 nm, 350 mW) and the light intensity was harmonically modulated by an Isomet 1211 acousto-optic modulator, which was controlled by the FRA. The modulation depth was 10% of the base light intensity, which was detected by a photodiode. For uniform illumination the diameter of the light spot was expanded (to $d=2.5$ cm) by a Newport Beam expander. The FRA provided the ratio of the modulated photocurrent to the modulated light intensity, *i.e.* the opto-electrical transfer function $j(\omega)/e\Phi(\omega)$.

Electrical Impedance Spectroscopy. Capacitance measurements were performed with an EG&G PAR 273A potentiostat and a three electrode electrochemical cell. The potential was harmonically modulated with a Solartron 1255 FRA. The modulation amplitude was 10 mV, and the modulation frequency was between 6×10^1 and 6×10^5 rad/s. The reference electrode was impedance matched to prevent phase shifts at high frequencies.³⁹

4.3 Results & Discussion

4.3.1 Characterisation of Self-Assembled Monolayers on Gold

The properties of the different layers on Au were studied with electrical impedance spectroscopy, cyclic voltammetry and AFM/STM. The results of the electrochemical experiments obtained with these systems are summarized in Table 4.1. EIS measurements showed that the capacitance of the Au/SAM/electrolyte junction drops from $46 \mu\text{F}/\text{cm}^2$ for bare gold to about $6\text{--}8 \mu\text{F}/\text{cm}^2$ for compounds **1-3**. For comparison, the capacitance of a well-ordered octadecanethiol-SAM on a gold electrode was $1.3 \mu\text{F}/\text{cm}^2$. The capacitance of these systems is determined by the dielectric constant, ϵ , and the thickness of the layers, d . Defects in the layer will lead to an increase of the capacitance which is consequently indicative of the quality of the layers. In Figures 4.3(a) and 4.3(b), cyclic voltammograms are shown for a bare gold electrode and gold electrodes provided with a SAM of compounds **1-3**. The current density at the maximum of the $\text{Fe}(\text{CN})_6^{4-}$ oxidation peak has decreased with respect to that of bare gold by a factor of 10 for **1** and a factor of 100 for **2** and **3**. Such a strong reduction of the Faradaic current

System	Capacitance $\mu\text{F}/\text{cm}^2$	I_{anodic} mA/cm^2
Au	46 ± 1.4	2.26
Au/dodecanthiol SAM	1.3 ± 0.04	1.4×10^{-2}
Au/ (1) SAM	8.2 ± 0.12	3.2×10^{-1}
Au/ (2) SAM	5.8 ± 0.6	5.9×10^{-2}
Au/ (3) SAM	6.7 ± 1.5	2.3×10^{-2}
Au/ (7) SAM	2.2 ± 0.2	4.8×10^{-2}
Au/ (8) SAM	5.8 ± 0.6	1.7×10^{-2}

Table 4.1 Capacitance of Au/SAM electrodes determined in the potential range from -0.5 V to 0.5 V in a 1.0 M Na_2SO_4 solution and peak current densities for the oxidation of $\text{Fe}(\text{CN})_6^{4-}$ at the electrode in a 10 mM $\text{Fe}(\text{CN})_6^{4-}/1.0$ M Na_2SO_4 solution.

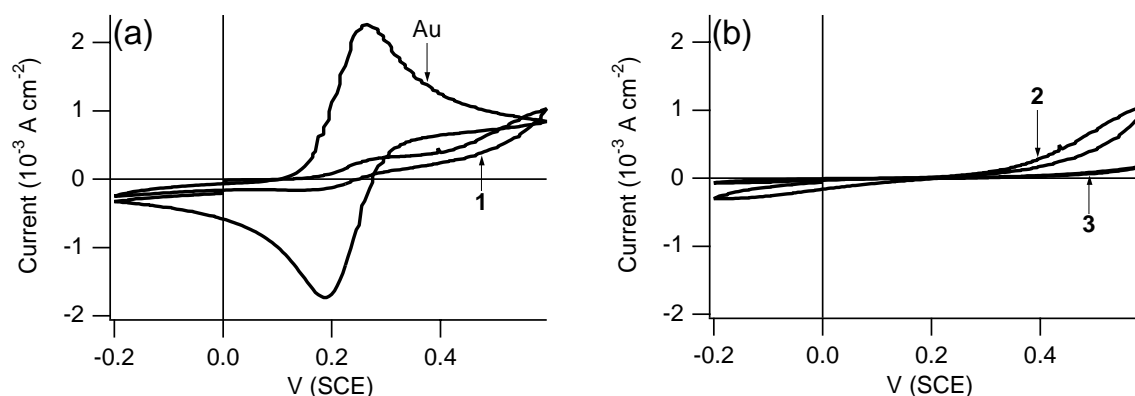


Figure 4.3 Cyclic voltammograms of (a) bare gold, and compound 1-SAM/gold, and (b) compound 2 and 3 SAM/gold electrodes.

shows that there are only a few pinholes in these layers.⁴⁰

AFM experiments revealed that the gold was uniformly covered by a thin layer (SAM) after the gold was immersed in solutions of compounds **1-3** in ethanol. Molecular resolution of the SAM structures was not obtained with contact mode AFM. Difficulties in imaging the SAM structure at molecular resolution with AFM were also encountered previously by others.⁴¹ In STM experiments on gold samples, which had been immersed in the ethanol/sulfide solutions, an adlayer was not observed on the gold, only the gold terraces underneath; the SAMs consist of insulating molecules, and have no electronic interaction with the tip. However, with a fixed tip position the conductivity increased with time, and the sample showed local damage in subsequent scans. This indicates that the SAM degrades from persistent electron tunneling. It was not possible to determine the SAM thickness with AFM and STM. The depth of the observed holes in the layer were independent of the chain length of the adsorbed sulfide and corresponded to monoatomic Au steps. The areas of the holes expanded on successive scanning of the tip. Tip-induced erosion of a thiol-modified Au surface has also been observed by others.⁴²⁻⁴⁴

4.3.2 CdSe Quantum Dots on Au and on Au/SAM.

Figure 4.4(a) shows an AFM image of CdSe electrodeposited on Au(111). The surface was uniformly covered with CdSe islands. The size of the dots was estimated from STM and AFM measurements and corresponded to 5 nm in diameter and height. This is in good agreement with what one expects on the basis of the amount of charge used to electrodeposit the particles. Scanning Tunneling Spectroscopy (STS) showed that the electronic coupling between these dots and the gold was strong, as will be discussed in chapter 5.

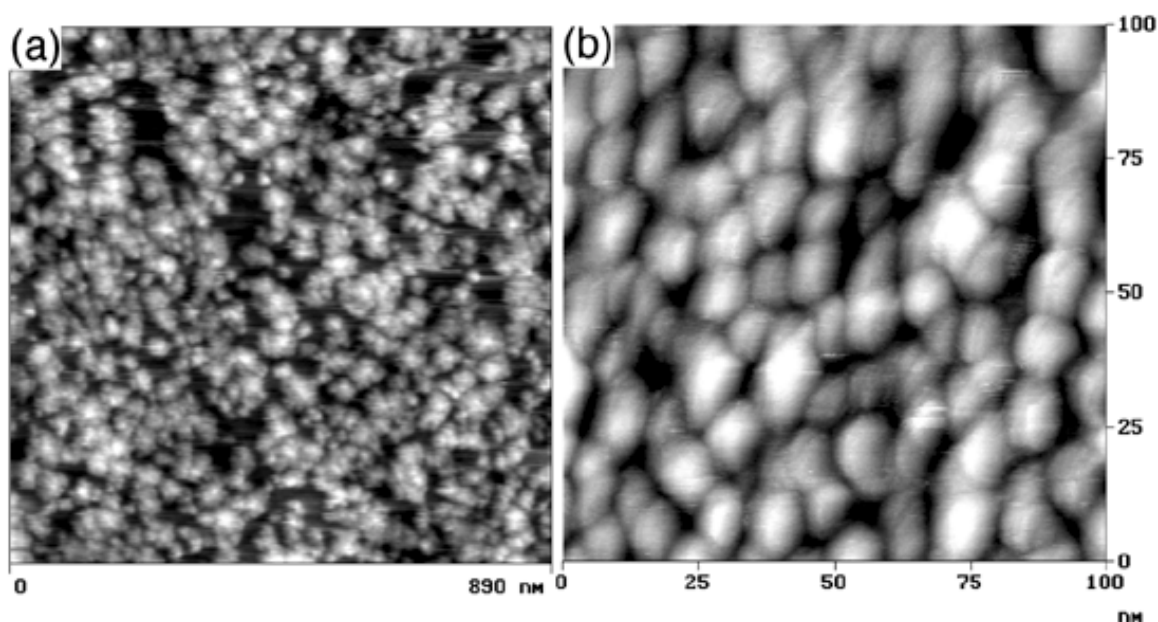


Figure 4.4 (a) An AFM image of electrodeposited CdSe on Au(111) recorded in the tapping mode with a Z-range of 3 nm. (b) An STM image of colloidal Q-CdSe deposited on Au/2-SAM (bias -1.0 V; set point 500 pA).

Since the dots were grown directly on the annealed gold, there is no insulating layer between the dot and the metal. Hence, the junction between the gold and the particle has a low tunnel resistance. Figure 4.4(b) presents an STM image of colloidal CdSe deposited on Au/5-SAM. The surface was uniformly covered with CdSe dots. STS showed that the electronic coupling between the colloidal particles and the gold was weak. Hence, the large tunneling resistance is due to the insulating SAM between the crystallites and the gold. The size of the colloidal particles, determined with TEM and optical absorbance, was 32 ± 4 Å.

4.3.3 Photoelectrochemistry.

Figure 4.5 shows a current-potential plot of a Au/5-SAM/CdSe electrode in an aqueous 1.0 M Na_2SO_4 solution (pH=7). The electrode was illuminated with chopped white light from a xenon lamp. Light-induced recombination transients upon a background current were observed between -0.9 V and -0.5 V. At potentials more positive than -0.5 V a steady-state photocurrent was observed, corresponding to anodic dissolution of the CdSe quantum dots. Samples provided with different spacer molecules and the electrodeposited CdSe on gold electrodes gave similar results. The observation of a photocurrent means that tunneling between the metal and the

quantum dot can compete with intra-particle decay. This indicates that, in competition with LUMO-HOMO recombination, a long-lived excited state can be formed after photon absorption.

Electrochemical studies on single crystals showed that the conduction band of n-CdSe is located at ~ 0.8 eV in aqueous solutions of pH 7.0 in the dark.⁴⁶⁻⁴⁹ The recombination transients for these quantised particles set in when the gold Fermi level is at or below 0.9 eV. From this we deduce that recombination transients are observed when E_F is below the LUMO of the quantum dot. Consequently, the long-lived excited state in Q-CdSe consists of an electron in the LUMO and a hole trapped in a bandgap state. Anodic transients were observed when the light was switched on, indicating that an electron tunnels from the LUMO of the particle to the gold. This is followed by electron tunneling from the gold to the trapped hole. Thus, exciton decay via the gold competes with intra-particle recombination.

Optical spectroscopy on Q-CdSe ($d=32$ Å) suspensions showed, besides the band-edge emission ($h\nu=2.3$ eV), a deep-trap emission ($h\nu=1.8$ eV) at an energy 0.5 eV below that of the band-edge emission.⁵⁰ The mechanism of this sub-bandgap emission could not be elucidated by photoluminescence measurements; it is not clear whether the photon is emitted by an electronic transition from the LUMO to a bandgap state or by a transition from a bandgap state to the HOMO. In this chapter we have shown that the long-lived excited state in CdSe consists of an electron in the LUMO and a hole trapped at 0.4 eV below the LUMO. From this it follows that the sub-bandgap emission must be due to the radiative transition of an electron from a bandgap state to the HOMO, resulting in a long-lived excited state with an electron in the LUMO, and an empty level located 0.4 eV below the LUMO. The bandgap state could consist of a surface Se^{2-} site, which can be oxidized to Se^\bullet by trapping a hole; this final state is still negatively charged and will therefore repel the electron in the LUMO. The electronic structure of the long-lived excited state in CdSe is similar to that in CdS, though in CdS the state has a somewhat higher energy. In view of the similarity of the photoelectrochemical properties of CdSe and CdS the mathematical model derived for CdS²⁶ can also be applied to CdSe.

4.3.4 Time-resolved Photoelectrochemistry

A typical spectrum of the opto-electrical transfer function, $j(\omega)/e\Phi(\omega)$, is shown in Figure 4.6(a) for a Au/3-SAM/Q-CdSe electrode in a deoxygenated 1.0 M Na_2SO_4 aqueous solution (pH=7). Two semicircles in the pos-neg and pos-pos quadrants are observed, with characteristic frequencies ω_a and ω_b , respectively. At low and high modulation frequencies $j(\omega)/e\Phi(\omega)$ tends to zero. $j(\omega)/e\Phi(\omega)$ corresponds to an anodic current at the working electrode, which means that

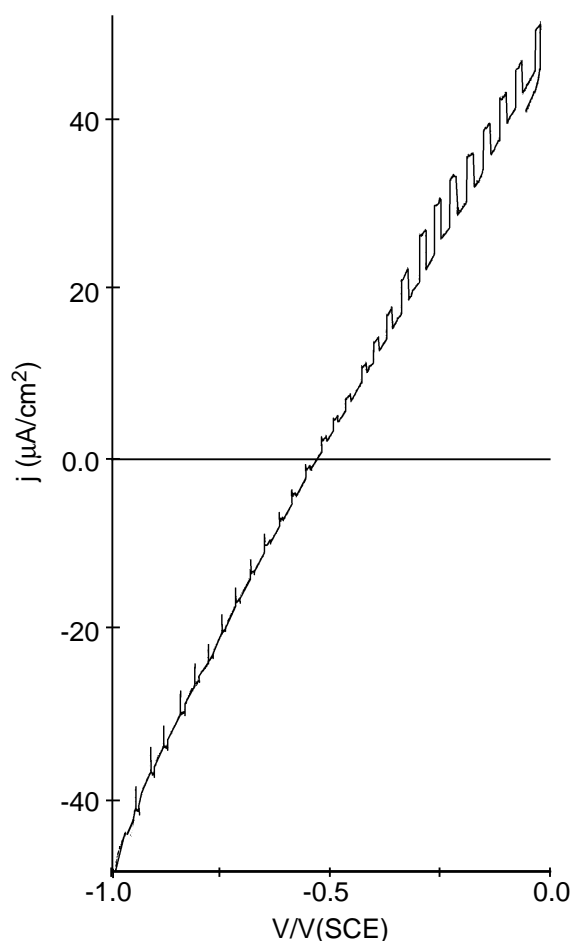


Figure 4.5 Current-potential curve of a Au/5-SAM/Q-CdSe electrode in an aqueous 1.0 M Na_2SO_4 solution. The electrode was illuminated with chopped white light from a xenon lamp.

electron tunneling from the dot to the Au occurs prior to tunneling from Au to the dot. The flattening of the upper semicircle and the frequency dispersion arise from a distribution of the tunneling rates around a mean value. It is found that $j(\omega)/e\Phi(\omega)$ is independent of the temperature ($293 \text{ K} < T < 333 \text{ K}$) and the photon flux ($10^{14} < \Phi_0 < 10^{17} / \text{cm}^2 \cdot \text{s}$). This means that two-photon processes or thermally activated electron transfers are not involved. The variation in the characteristic frequencies obtained with different samples of a given Au/SAM/Q-CdSe configuration can be seen in Figure 4.8.

The transfer function can be interpreted by the simplified model presented in Figure 4.1. At high modulation frequencies, no tunneling process is able to follow the light modulation; this corresponds to $j(\omega)/e\Phi(\omega)=0$. When the frequency is decreased the faster process can follow the modulation; since the current is anodic, this is electron tunneling from the LUMO of the particle to the gold. Upon further decrease of the frequency, the slower process can also be observed; this is electron tunneling from the gold to the trapped hole. In chapter 2 we developed a mathematical model for charge transfer between a CdS quantum dot and a gold electrode.³⁰⁻³¹

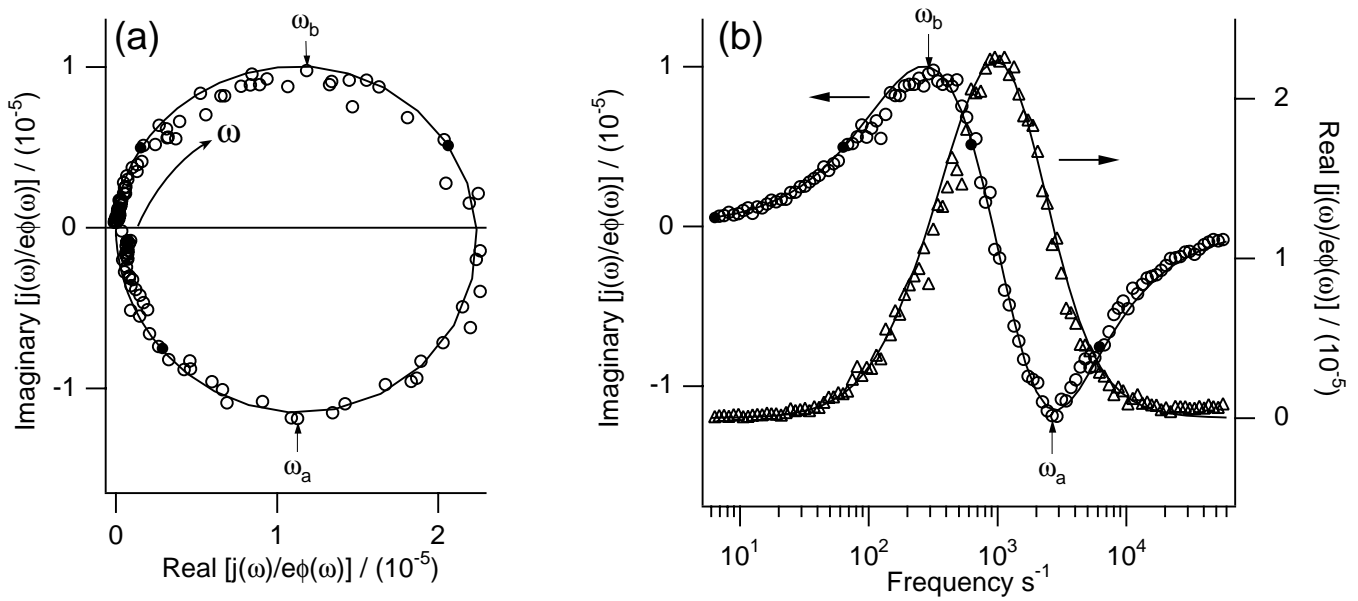


Figure 4.6 (a) Optoelectrical transfer function of a Au/3-SAM/Q-CdSe electrode in an aqueous 1.0 M Na_2SO_4 solution (markers) and the fit to the data (solid line). (b) Bode plots of the real (triangles) and imaginary part (circles) of the function and the fit (solid line). For the fit only $k_{L,Au}$, $k_{Au,T}$, the distribution in the rate constants and a dimensionless scaling prefactor were taken as variables.

By solving the first-order rate equations for the steps in which the different states of the quantum dot are involved, we obtained an expression for the steady-state photocurrent and the opto-electrical transfer function. This calculated transfer function is compared to that measured experimentally with a Au/SAM/Q-CdSe system in 1.0 M Na_2SO_4 . The observed opto-electrical transfer function, shown in Figure 4.6(a), corresponds to excited state decay via two consecutive electron tunneling steps between the particle and the gold. The characteristic frequency of the semicircle in the positive-negative quadrant, ω_a , corresponds to $k_{L,Au}$, the rate constant for electron tunneling from the LUMO of the particle to the gold. The characteristic frequency of the semicircle in the positive-positive quadrant, ω_b , corresponds to $k_{Au,T}$, the rate constant for tunneling from the gold to the trapped hole. The tunneling rate constants are thus directly determined from the IMPS results. The flattening of the semicircles is caused by a dispersion of rate constants, originating from a distribution in tunneling distance. Defects in the SAM, a particle size distribution and the fact that the trapped hole can be located anywhere in or on the surface of the particle lead to a variation in tunneling distance. However, in practice only the charge carriers with the smallest tunneling distance will contribute to the transfer function. A Gaussian distribution around an average distance, s_0 (the length of the spacer molecule) is assumed with $\sigma = 0.10 s_0$; this leads to a variation in the tunneling rates of $\pm 15\%$. The model is then found to be in good agreement with the data as shown in the Bode plots in Figure 4.6(b).

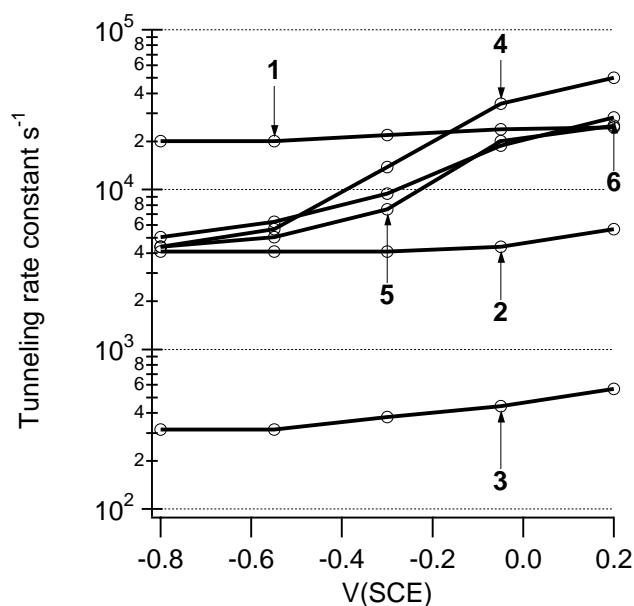


Figure 4.7 Tunneling rates of the cathodic process are plotted semi-logarithmically versus the applied potential for **1-6** SAM/Q-CdSe modified gold electrodes.

4.3.5 Distance-Dependence of Electron Tunneling

To study the distance dependence of the tunneling rate, the distance between the particles and the gold was varied by using Self-Assembled Monolayers of different chain length. The tunneling rate constants for CdSe dots electrodeposited on gold were faster than $2 \cdot 10^5 \text{ s}^{-1}$, which is the upper limit of our set-up. A high tunneling rate was to be expected since an insulating layer is not present between the dot and the gold. The rate constants for the samples with SAMs formed by compounds **4-6**, were strongly dependent on the applied potential and did not show a trend upon a chain length variation as is shown in Figure 4.7. It is known from the literature that these dithiol molecules are not rigid and do not give a perfectly ordered SAM.⁵¹ A tentative explanation of the potential dependence of the tunneling rates may be that these layers deform when the potential is changed. The particles are probably surrounded by a negatively charged (AOT) capping layer. When the potential of the electrode is lowered, the charge density on the metal becomes more positive (or less negative); the particles may be attracted to the gold electrode. Consequently, the effective tunneling distance between the dots and the gold decreases, and the tunneling rate increases. In contrast, the potential dependence observed with the rigid compounds **1-3** was very weak, indicating that these SAMs are more ordered and more rigid than the dithiols. The double bonds between the rings prevent bending of the molecules and, due to intermolecular interactions, these SAMs are well-ordered. A clear dependence of the tunneling rate on the distance was found with **1-3** as shown in Figure 4.8. The tunneling rate increases by

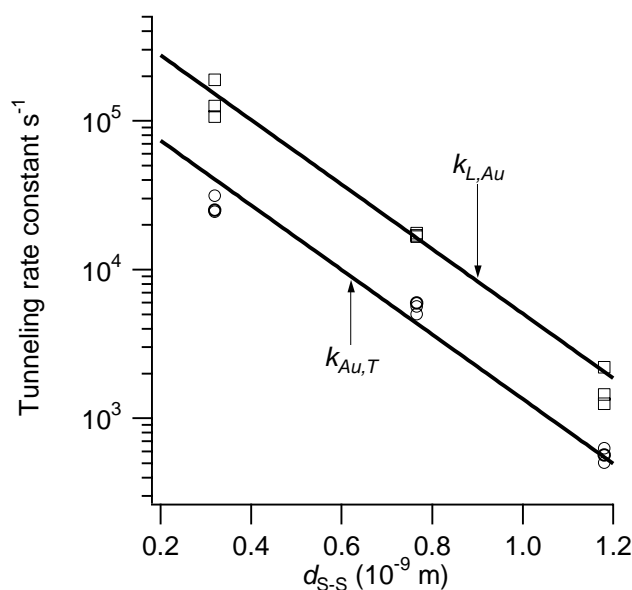


Figure 4.8 The tunneling rates are plotted semi-logarithmically versus the intramolecular S-S distance, d_{S-S} , for the anodic ($k_{L,Au}$; squares) and the cathodic ($k_{Au,T}$; circles) processes with **1-3**. The results, obtained with three different samples of each configuration, and the fits to the data (solid lines) are shown.

two orders of magnitude upon a decrease in S-S distance from 11.8 to 3.4 Å. In Figure 4.8, the measured tunneling rate constants for the anodic and cathodic processes are plotted semi-logarithmically versus the length of the spacer molecule, d_{S-S} . A linear relationship is observed. Assuming elastic tunneling through a one-dimensional barrier, $k = k_0 e^{-\beta d_{S-S}}$, we obtain values of $\beta = 0.50 \pm 0.05 \text{ \AA}^{-1}$. Compounds **7** and **8**, similar to **2** and **3**, respectively, but with only one sulfur atom, were also used to form SAMs on Au. These compounds were attached to the gold via the sulfur atom and formed ordered, current-blocking SAMs (see Table 4.1) due to their intermolecular interactions. After immersion in the Q-CdSe suspension these samples did not give a photosignal, indicating that the particles are not adsorbed on a SAM of **7** and **8**. This is supported by the fact that no dots were observed on SAMs of **7** and **8** on Au with STM. These results indicate that the dots are chemically bound to the spacer molecules **1-3**, probably via a covalent Cd-S interaction.¹²

The distance dependence of electron tunneling is often studied with redox centers attached via alkanethiol SAMs on gold and with biological (DNA, proteins) or synthetic organic *donor-link-acceptor* molecules. A problem with this approach is that the Gibbs free energy of the transfer reaction, ΔG^0 , and the reorganization energy, λ , of the reaction centres are controlled by molecular properties and the solvent.¹⁷⁻²⁴ Another problem is that the tunneling rates are obtained indirectly by measuring the emission decay of the donor site. Fluorescence quenching might

involve another mechanism than electron transfer. To obtain the rate of electron tunneling in such systems several assumptions have to be made. The advantage of studying the relationship between the tunneling rate and distance with Au/SAM/Q-CdSe systems is that no activation or reorganization energy is involved. Because analogous molecules are used to vary the tunneling distance, the tunnel barrier height is kept constant. Thus, the relationship between the electron tunneling rates and the distance can be determined directly from IMPS measurements on these systems, without interference from other parameters.

From Figure 4.8 it is clear that the tunneling rates for the anodic and the cathodic processes depend exponentially on the tunneling distance. A value for β of $0.50 \pm 0.05 \text{ \AA}^{-1}$ was determined from the slope of the plots. The spacer molecules are probably oriented, not perpendicular to the gold surface, but at a small angle to the normal axis. From single crystal X-ray diffraction it was found that these molecules have an angle of $\sim 23^\circ$ with respect to the *c*-axis.³⁰ When it is assumed that all molecules **1-3** are tilted 23° to the normal axis a value for β of $0.55 \pm 0.05 \text{ \AA}^{-1}$ was found. This value for β is much smaller than that calculated for electron transfer through vacuum (2.0 \AA^{-1}). In many reactions between solvated donors and acceptors β varies between 1.0 and 2.0 \AA^{-1} .¹⁷ In systems in which the electroactive center is coupled to an electrode via an alkanethiol SAM the values for β vary between $0.2-0.95 \text{ \AA}^{-1}$, depending on the conjugation of the bridging molecules.²⁵⁻²⁸ However, in systems consisting of a dye and acceptor, separated by a fatty-acid, smaller values for β ($0.3-0.5 \text{ \AA}^{-1}$) were obtained, while in DNA systems even smaller values ($0.1-0.4 \text{ \AA}^{-1}$) were found.²¹ Possible explanations for the low values of β given by others are that the spacer between donor and acceptor may decrease the effective tunneling barrier height with respect to the vacuum level or that tunneling occurs via intermediate states. In our systems, a superexchange mechanism via ‘through-bond-interaction’ (TBI), involving the σ -orbitals of the cyclohexyl-type rings, may be responsible for the small distance dependence of electron tunneling. TBI can play a significant role in electronic coupling between the donor and acceptor sites, and consequently influence the distance dependence.⁵²⁻⁵⁴ Photo-electron spectroscopy (PES) has unequivocally shown that the 3p-sulfur lone pair orbitals [Lp_{S}] and the olefinic π -bond orbitals [$\pi(C=C)$] in the spacer molecules used are strongly coupled via a through-bond interaction involving the $H_{ax}-C-C-H_{ax}$ orbitals of the cyclohexyl-type rings. For compounds **1-3** a splitting of the two Lp_{S} orbitals, $\Delta E_{\text{v,j}}$, of 0.45 eV, 0.40 eV and ~ 0.3 eV was found, respectively. These orbitals interact via the hydrocarbon skeleton over distances of *ca.* 8 \AA and 12 \AA .³⁵ Consequently, upon physisorption via one Lp_{S} orbital the second one positioned at the opposite end of the molecule will be perturbed and as such these

oligo(cyclohexylidenes) can be envisaged as molecular relays.³⁴ Electron-donor/electron-acceptor functionalized oligo(cyclohexylidenes) were also shown to be active in photoinduced charge separation.⁵⁴ The distance dependence should be slightly different for the anodic and cathodic process, due to the different effective barrier height.

The lowest value for $k_{L,Au}$, tunneling from the LUMO of the dot to the gold, was obtained with the **3**-SAM system and was $\sim 2 \cdot 10^3 \text{ s}^{-1}$. Since this tunneling process has to compete with intra-particle recombination, the lifetime of the long-lived excited state must exceed 0.5 ms. Bawendi and coworkers^{57,58} have performed photoluminescence measurements on single CdSe quantum dots and they found a fluorescence intermission with an average time of about seconds. The on/off times were influenced by the capping of the dot, indicating that surface states were involved. These processes were explained by photoionisation in which one of the charge carriers was trapped. This indicates that trapping of a charge carrier can lead to an excited state with a remarkably long lifetime of seconds. The fastest tunneling process in the Au/Q-CdSe system is tunneling from the LUMO to the gold. This agrees with earlier work, in which we showed that the free charge carrier has a higher tunneling probability than the trapped carrier.³¹

4.4 Conclusions

We show that IMPS is a direct and elegant method for studying photoinduced electron tunneling between a gold substrate and an anchored nanoparticle and the dependence of the tunneling rate on the distance between the two. This method has the advantage that elastic electron transfer proceeds without (solvent) reorganization and the tunneling rate is measured directly. This photoelectrochemical method allows us to determine the electronic structure of a long-lived excited state in CdSe quantum dots, giving information supplementary to that of optical spectroscopy. In agreement with previous work it was shown that the free charge carrier has a higher tunneling probability than the trapped carrier, due to the fact that the trapped carrier has a larger average tunneling distance than the free charge carrier.

References

1. D.L. Klein, P.L. McEuen, J.E. Bowen Katari, R. Roth, and A.P. Alivisatos, *Appl. Phys. Lett.* **1996**, *68*, 2574-2576
2. D.L. Klein, R. Roth, A.K.L. Lim, A.P. Alivisatos, and P.L. McEuen, *Nature* **1997**, *389*, 699-701
3. S-H. Kim, G. Markovich, S. Rezvani, S.H. Choi, K.L. Wang, and J.R. Heath, *Appl. Phys. Lett.* **1999**, *74*, 317-319
4. H. Mattoussi, L.H. Radzilowski, B.O. Dabbousi, D.E. Fogg, R.R. Schrock, E.L. Thomas, M.F. Rubner, and M.G. Bawendi, *J. Appl. Phys.* **1999**, *86*, 4390
5. Y. Yang, S. Xue, S. Liu, J. Huang, and J. Shen, *Appl. Phys. Lett.* **1996**, *69*, 377
6. W.U. Huynh, X. Peng, and A.P. Alivisatos, *Adv. Mat.* **1999**, *11*, 923
7. S. Chen, R.S. Ingram, M.J. Hostetler, J.J. Pietron, R.W. Murray, T.G. Schaaff, J.T. Khoury, M.M. Alvarez, and R.L. Whetten, *Science* **1998**, *280*, 2098-2101
8. C.B. Murray, C.R. Kagan, and M.G. Bawendi, *Science* **1995**, *270*, 1335-1338
9. J.R. Heath, *Science* **1995**, *270*, 1315
10. R.P. Andres, J.D. Bielefeld, J.I. Henderson, D.B. Janes, V.R. Kolagunta, C.P. Kubiak, W.J. Mahoney, and R.G. Osifchin, *Science* **1996**, *273*, 1690-1693
11. C.B. Murray, D.J. Norris, and M.G. Bawendi, *J. Am. Chem. Soc.* **1993**, *115*, 8706-8715
12. V.L. Colvin, A.N. Goldstein, and A.P. Alivisatos, *J. Am. Chem. Soc.* **1992**, *114*, 5221-5230
13. J.E. Bowen Katari, V.L. Colvin, A.P. Alivisatos, *J. Phys. Chem.* **1994**, *98*, 4109-4117
14. M. Miyake, H. Matsumoto, M. Nishizawa, T. Sakata, H. Mori, S. Kuwabata, and H. Yoneyama, *Langmuir* **1997**, *13*, 742-746
15. T. Nakanishi, B. Ohtani, and K. Uosaki, *J. Phys. Chem.* **1998**, *102*, 1571-1577
16. K. Hu, M. Brust, and A.J. Bard, *Chem. Mater.* **1998**, *10*, 1160-1165
17. R.A. Marcus, N. Sutin, *Biochim. et Biophys. Acta* **1985**, *811*, 265-322
18. C.C. Moser, J.M. Keske, K. Warncke, R.S. Farid, and P.L. Dutton, *Nature* **1992**, *355*, 796-802
19. C.C. Page, C.C. Moser, X. Chen, and P.L. Dutton, *Nature* **1999**, *402*, 47-52
20. G.L. Closs, J.R. Miller, *Science* **1988**, *240*, 440-446
21. S.O. Kelley, and J.K. Barton, *Science* **1999**, *283*, 375-381
22. P.F. Barbara, T.J. Meyer, and M.A. Ratner, *J. Phys. Chem.* **1996**, *100*, 13148-13168
23. E. Meggers, M.E. Michel-Beyerle, and B.J. Giese, *J. Am. Chem. Soc.* **1998**, *120*, 12950-12955
24. F.D. Lewis, T. Wu, Y. Zhang, R.L. Letsinger, S.R. Greenfield, and M.R. Wasielewski, *Science* **1997**, *277*, 673-676

25. C.E.D. Chidsey, *Science* **1991**, *251*, 919-922
26. H.O. Finklea, L. Liu, M.S. Ravenscroft, and S. Punturi, *J. Phys. Chem.* **1996**, *100*, 18852-18858
27. K. Slowinski, K.U. Slowinska, and M. Majda, *J. Phys. Chem.* **1999**, *103*, 8544-8551
28. Y. Gu, B. Akhremitchev, G.C. Walker, and D.H. Waldeck, *J. Phys. Chem.* **1999**, *103*, 5220-5226
29. S.G. Hickey, and D.J. Riley, *J. Phys. Chem. B* **1999**, *103*, 4599-4602
30. E.P.A.M. Bakkers, E. Reitsma, J.J. Kelly, and D. Vanmaekelbergh, *J. Phys. Chem. B.* **1999**, *103*, 2871-2788
31. E.P.A.M. Bakkers, J.J. Kelly, and D. Vanmaekelbergh, *J. Electroanal. Chem.* **2000**, *482*, 48-55
32. E.P.A.M. Bakkers, A.W. Marsman, L.W. Jenneskens, and D. Vanmaekelbergh, *Angew. Chem. int. Ed.* **2000**, *39*, 2297-2299; *Angew. Chem.* **2000**, *112*, 2385-2388
33. M.L. Steigerwald, A.P. Alivisatos, J.M. Gibson, T.D. Harris, R. Kortan, A.J. Muller, A.M. Thayer, T.M. Duncan, D.C. Douglas, and L.E. Brus, *J. Am. Chem. Soc.* **1988**, *110*, 30460-3050
34. A.W. Marsman, *Ph.D. Thesis* **1999**, Utrecht University, The Netherlands
35. A.W. Marsman, R.W.A. Havenith, S. Bethke, L.W. Jenneskens, R. Gleiter, J.H. van Lenthe, M. Lutz, and A.L. Spek, *J. Org Chem* **2000**, in press
36. G. Hodes, I.D.J. Howell, and L.M. Peter, *J. Electrochem. Soc.* **1992**, *139*, 3136-3140
37. B. Alpers, H. Demange, I. Rubinstein, and G. Hodes, *J. Phys. Chem. B* **1999**, *103*, 4943-4948
38. Y. Golan, G. Hodes, and I. Rubinstein, *J. Phys. Chem.* **1996**, *100*, 2220-2228
39. F. Mansfeld, S. Lin, Y.C. Lin, and H.J. Shih, *J. Electrochem. Soc.* **1988**, *135*, 906-907
40. B.H. Huisman, *Ph.D. Thesis* **1998**, University of Twente, The Netherlands
41. K. Edinger, A. Golzhauser, K. Demota, Ch. Woll, and M. Grunze, *Langmuir* **1993**, *9*, 4.
42. Y-T. Kim, R.L. McCarley, and A.J. Bard, *J. Phys. Chem.* **1992**, *96*, 7416,
43. C. Schönenberger, J.A.M. Sondag-Huethorst, J. Jorritsma, and L.G.J. Fokkink, *Langmuir* **1994**, *10*, 611
44. J.P. Bucher, L. Santesson, and K. Kern, *Langmuir* **1994**, *10*, 979
45. E.P.A.M. Bakkers, and D. Vanmaekelbergh, accepted for publication in *Phys. Rev. B.* (rapid communication)
46. K.W. Frese Jr., *J. Electrochem. Soc.* **1983**, *130*, 28-33
47. K.W. Frese, *J. Appl. Phys.* **1982**, *53*, 1571-1576

48. A.B. Ellis, S.W. Kaiser, J.M. Bolts, and M.S. Wrighton, *J. Am. Chem. Soc.* **1977**, *99*, 2839
49. E.C. Dutoit, R.L. Van Meirhaeghe, F. Cardon, and W.P. Gomes, *Ber. Bunsen-Ges.* **1975**, *79*, 1206-1213
50. M.G. Bawendi, P.J. Carroll, W.L. Wilson, and L.E. Brus, *J. Chem. Phys.* **1992**, *96*, 946-954
51. D.J. Lavrich, S.M. Wetterer, S.L. Bersanek, and G.J. Scoles, *J. Phys. Chem. B* **1998**, *102*, 3456 and references cited.
52. P. Pasman, G.F. Mes, N.W. Koper, and J.W. Verhoeven, *J. Am. Chem. Soc.* **1985**, *107*, 5839
53. M.N. Paddon-Row, *Acc. Chem. Res.* **1994**, *27*, 18 and references cited
54. F.J. Hoogesteger, C.A. van Walree, L.W. Jenneskens, M.R. Roest, J.W. verhoeven, W. Schuddeboom, J.J. Piet, and J.M. Warman, *J.M. Chem. Eur. J.* **2000**, in press
55. S.B. Sachs, S.P. Dudek, R.P. Hsung L.R. Sita, J.F. Smalley, M.D. Newton, S.W. Feldberg, and C.E.D. Chidsey, *J. Am. Chem. Soc.* **1997**, *119*, 10563-10564
56. K. Slowinski, R.V. Chamberlain, C.J. Miller, and Majda, *J. Am. Chem. Soc.* **1997**, *119*, 11910-11919
57. S.A. Emedocles, D.J. Norris, and M.G. Bawendi, *Phys. Rev. Lett.* **1996**, *77*, 3873-3876
58. M. Nirmal, B.O. Dabbousi, M.G. Bawendi, J.J. Macklin, J.K. Trautman, T.D. Harris, and L.E. Brus, *Nature* **1996**, *383*, 802-804

Scanning Tunneling Spectroscopy with Symmetrical and Asymmetrical Tip/Quantum Dot/Gold Configurations

Abstract

Resonant electron tunneling through nanometer-sized CdSe and CdS crystals was studied with Scanning Tunneling Spectroscopy. The gold/nanocrystal/tip configuration forms an electrical device with two tunnel barriers, one between the substrate and the nanocrystal and the other between the nanocrystal and the tip. For crystals grown electrochemically on bare gold, the applied bias is distributed asymmetrically over the barriers of the junction; a change of the bias results mainly in a shift of the tip Fermi level with respect to the electron levels of the dot. The tunnel spectra provide evidence for resonant tunneling through discrete levels of the conduction and valence bands. The bias can be distributed more symmetrically in configurations in which CdSe and CdS colloids are covalently anchored on a gold substrate via hexane dithiol. If the bias distribution is nearly symmetrical, resonant tunneling at both negative and positive bias only involves levels of the conduction band.

5.1 Introduction

The development of scanning probe techniques has made possible the investigation of materials at the atomic level. In addition, with Scanning Tunneling Spectroscopy (STS) the electronic structure of a surface can be studied with molecular resolution. There is a growing interest in the electrical and optical properties of insulating and semiconducting quantum dots (QD). Recently, the density of states (DOS) of single molecules^{1,2}, metallic³⁻⁵ and semiconductor quantum dots⁶⁻¹¹ (Si, CdS, CdSe, and InAs) has been probed by STS.

Bard and coworkers⁷ have performed STS measurements on single CdS quantum dots. The tip of the STM is positioned above an individual quantum dot, forming a Double-Barrier Tunnel Junction (DBTJ), as shown in Figure 5.1. The tunneling current I through the DBTJ is measured as a function of the bias V . They reported that if the tip was retracted from the dot, the tunneling spectra (differential conductance dI/dV vs V) show an energy region in which the conductance is very low, corresponding to the bandgap of the particle. When the tip/dot distance was decreased a smaller energy region with low-conductance was observed. It seems that the experimental STS results can only be interpreted for measurements in which the tip/dot distance is relatively large. The problem has also been recognized in STS studies of the electronic structure of InAs and CdSe quantum dots. For instance, Banin *et al.*¹⁰ and Alpers *et al.*¹¹ reported that the tip should be retracted from the dot in order to establish an asymmetrical DBTJ. The distribution of the applied bias over the DBTJ appears to be an important factor for the interpretation of the tunneling spectra.¹² Datta *et al.*^{1,2} have discussed this topic in relation to tunneling spectroscopy with molecules covalently bound to the substrate. How resonant tunneling through quantum dots depends on the distribution of the applied bias over the substrate/dot/tip junction has, however, not been studied systematically.

In this chapter we describe in more detail how the bias distribution over the junction affects the tunneling spectra. For this purpose, we used two types of junction; the electronic coupling between the substrate and the QD could be tuned by the deposition procedure of the dots on the conducting substrate. The dots can be grown electrochemically on the substrate leading to a dot/substrate barrier with a relatively high capacitance (strong coupling, see Figure 5.1(a)). Alternatively, colloidal nanocrystals can be linked to the substrate by organic spacer molecules resulting in a dot/substrate barrier with a relatively low capacitance (weak coupling, see Figure 5.1(b)). Additionally, the coupling between the tip and the QD can be varied by changing the

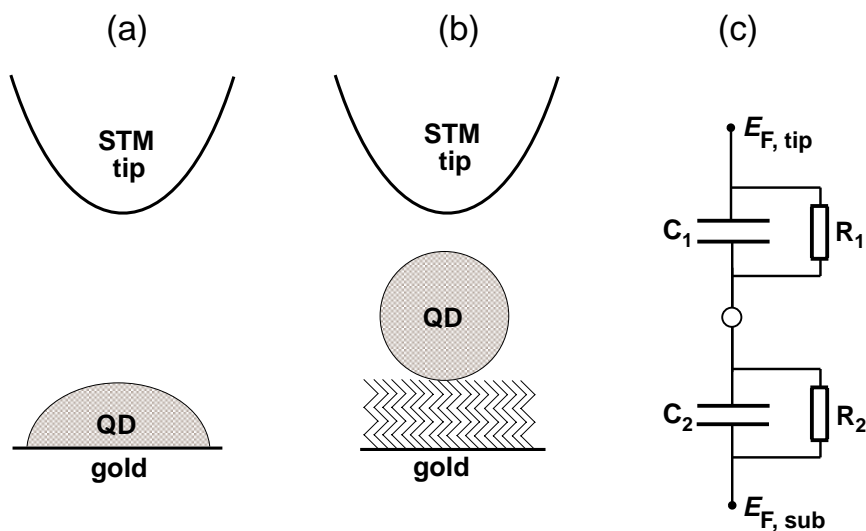


Figure 5.1 A Double-Barrier Tunnel Junction (DBTJ) is formed when the STM tip is positioned above a quantum dot, which is (a) electrodeposited on a gold substrate and (b) covalently anchored to a dithiol SAM on gold. In (c) the electrical equivalent circuit corresponding to the DBTJ is shown. The shape of the quantum dots in the image is arbitrary and is possibly different from the real shape.

tip–QD distance.

If the dots are 'strongly coupled' to the substrate and 'weakly coupled' to the tip (*asymmetrical* DBTJ, Figure 5.1(a)), the voltage drops entirely over the dot/tip junction and the valence and conduction band levels of the QD are fixed with respect to the substrate Fermi level, $E_{F,Au}$. When V is varied the tip Fermi level, $E_{F,tip}$, shifts with respect to the energy levels of the nanocrystal. In a tunneling spectrum, in which the differential conductance, dI/dV , is measured as a function of V , an increased conductance is observed each time $E_{F,tip}$ comes into resonance with a single electron level of the valence or conduction band.

When the dots are 'weakly coupled' to the substrate and the tip (*symmetrical* DBTJ, Figure 5.1(b)), the voltage is distributed over both junctions and the valence and conduction band levels of the QD are not fixed with respect to $E_{F,Au}$ or $E_{F,tip}$. When the potential is scanned, both $E_{F,Au}$ and $E_{F,tip}$ shift with respect to the levels in the nanocrystal. The tunneling spectra contrast sharply with those obtained in an asymmetrical configuration. It will become clear that the distribution of the bias over the two barriers of the junction plays a critical role in the features observed with tunneling spectroscopy. Quantitative interpretation of the experimental tunneling spectra is only possible if the ratio of capacitances of the two junctions is known.

5.2 Experimental

The chemicals used were of *pro analysi* (analytical grade) quality from Merck. High-purity water (18 M Ω /cm) was used to prepare the solutions. All manipulations involving bis-trimethylsilylselenium, (TMS)₂Se, dimethylcadmium (Me₂Cd), tri-n-octylphosphine (TOP), and trioctylphosphineoxide (TOPO) were carried out in a nitrogen-filled glovebox.

Colloidal Suspensions. The aqueous **CdS** and non-aqueous **CdSe (I)** suspensions were prepared according to the methods described in chapters 2 and 4. The **CdSe (II)** suspension was prepared according to Reference 13. A 1.0 M stock solution of TOP-complexed selenium (TOPSe) was prepared by dissolving 0.8 g selenium shot directly in 15 g TOP. For the preparation of the TOPCd stock solution a sample of 2.0 g Me₂Cd (STREM chemicals) was dissolved in 15 g TOP. Stoichiometric amounts of both stock solutions were combined and diluted with TOP to 10 ml, and loaded into a 10-ml syringe. A sample of 25 g trioctylphosphineoxide (TOPO) was heated to 400°C. The heat source was removed and when the desired temperature was reached (300-350°C) the contents of the syringe were quickly added to the vigorously stirred TOPO by a single injection. Immediately an orange/yellow colour developed and the temperature dropped to 180°C. The temperature was increased to 250°C and stabilised to establish steady growth and annealing of the particles for several hours. The solution was cooled to room temperature and the dots were removed from the solidified TOPO by washing with anhydrous methanol. Finally, the dots were dispersed in toluene. The temperature of the TOPO solution at the moment of injection determined the final particle size.

Gold samples. The gold samples were annealed and provided with electrochemically deposited nanocrystals. Alternatively, the gold samples were provided with a 2-SAM (see chapter 4) or a propanedithiol-SAM; a submonolayer of the quantum dots was deposited on the Au/SAM or on the bare gold. The procedures were performed according to the methods described in chapter 4.

STM/AFM. STM topographic images were obtained in ambient air (40 % humidity) with a Nanoscope III (Digital Instruments, Santa Barbara, CA) with an electrochemically etched Pt/Ir (90/10) tip. AFM images of the electrodeposited CdS on gold were obtained under ambient conditions in tapping mode with a tapping mode tip, provided by Digital Instruments. For Tunneling Spectroscopy the tip was positioned above an individual quantum dot and the scanning

and feedback controls were switched off. The tunneling spectra are obtained by numerically differentiating the measured I - V curves. At room temperature reproducible spectra could be obtained during ~ 60 seconds after the tip was positioned above a particle. This time is limited by thermal drift in the system, which moves the tip with respect to the sample. STM measurements at 4.2 K were performed on a home-built STM in a vacuum chamber containing a small amount of helium to act as a heat exchange gas; the STM was cooled in an Oxford cryostat. The design of the low-temperature STM is described in Reference 14.

5.3 Results

5.3.1 Topography of CdSe and CdS Quantum Dots on Gold

Figure 5.2(a) shows a topographic STM image of electrodeposited CdSe on gold (111), and Figure 5.2(b) an AFM (tapping mode) image of electrodeposited CdS on gold (111). The

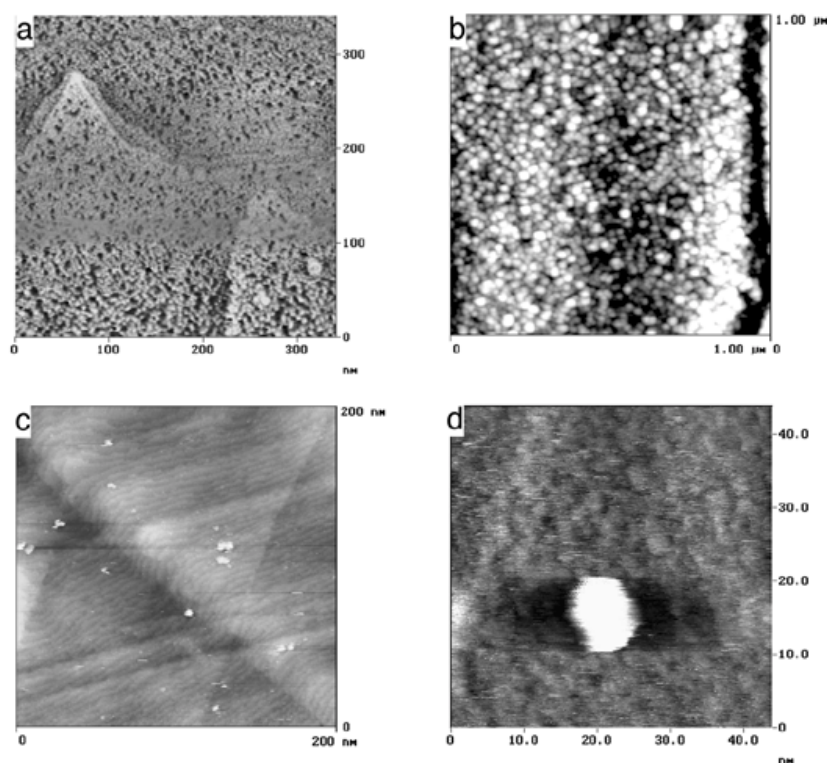


Figure 5.2. STM images of (a) electrodeposited CdSe quantum dots on gold (bias 1.2 V, set point 200 pA; height scale 4 nm), (c) colloidal CdSe (bias 1.4 V, set point 25 pA; height scale 5 nm), and (d) a single CdS QD on a SAM on gold (bias 1.3 V, set point 150 pA; height scale 5 nm). (b) AFM (TM) image of electrodeposited CdS on gold (scale 10 nm). All images were acquired with a Nanoscope III under ambient conditions.

surfaces were uniformly covered with individual semiconductor islands; the diameter and height of the CdSe and CdS dots were approximately 5 nm and 10 nm, respectively, which is in good agreement with what one expects on the basis of the amount of charge used to electrodeposit the particles. Hodes *et al.* have shown with TEM that the dots are spatially isolated¹⁵; due to tip-convolution with a scanning probe technique, the dots seem to be interconnected. The barrier between the dots and the gold is possibly related to a monolayer of elemental selenium, which is adsorbed spontaneously on the gold surface, prior to the electrodeposition of the QDs.¹¹ Figure 5.2(c) presents an STM images of a submonolayer of colloidal CdSe particles on gold and 5.2(d) an STM image of a single CdS dot deposited on gold/hexanedithiol-SAM. For the TS experiments isolated QDs were selected. The tunneling barrier between the dot and the gold is due to the insulating SAM between the crystallites and the gold.

5.3.2 Scanning Tunneling Spectroscopy

In Figure 5.3 a plot of the tunneling current I between the tip and the substrate is shown as a function of the bias V for a freshly-annealed Au surface in vacuum at 4.2 K. The distance between the tip and the gold was controlled by the set point current (20 pA at 1.0 V). In the potential range around zero bias I increases linearly with V . This type of relationship has previously been observed by others and is characteristic for elastic electron tunneling between a Pt tip and a clean Au surface.¹⁶

In Figures 5.4(a) and 5.4(c) current-voltage (I vs V) curves are presented for electrodeposited CdSe ($d \cong 100$ Å) and CdS ($d \cong 100$ Å) quantum dots, respectively. The distance between the tip and the quantum dot was varied by changing the set point current at a constant

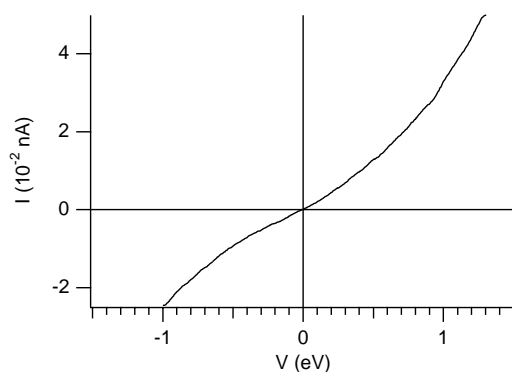


Figure 5.3 I - V curve acquired with a clean Au(111) surface at 4.2 K (bias 1.0 V, set point 20 pA)

bias voltage. The corresponding tunneling spectra (dI/dV vs V) of the CdSe and CdS samples are shown in Figures 5.4(b) and 5.4(d), respectively. In the current-voltage curves a region of very low current was observed in a considerable range around $V=0$, corresponding to the zero-conductance-gap in the tunneling spectra. The width of this zero-conductance-gap in Figure 5.4(b) decreases from 1.9 eV to 1.6 eV with an increase of the set point current from 20 pA to 3.0 nA. An increase in the set point current from 200 pA to 2.4 nA decreases the width of the gap in Figure 5.4(d) from 2.4 eV to 2.0 eV. The bandgap of bulk CdSe at room temperature is 1.84 eV and that of CdS is 2.4 eV as indicated by the dotted lines in Figures 5.4(b) and 5.4(d). Such a weak dependence of the width of the zero-conductance-gap on the tip-to-dot distance was also observed with smaller quantum dots with $d \cong 50 \text{ \AA}$ and $d \cong 20 \text{ \AA}$. The tunneling spectra in

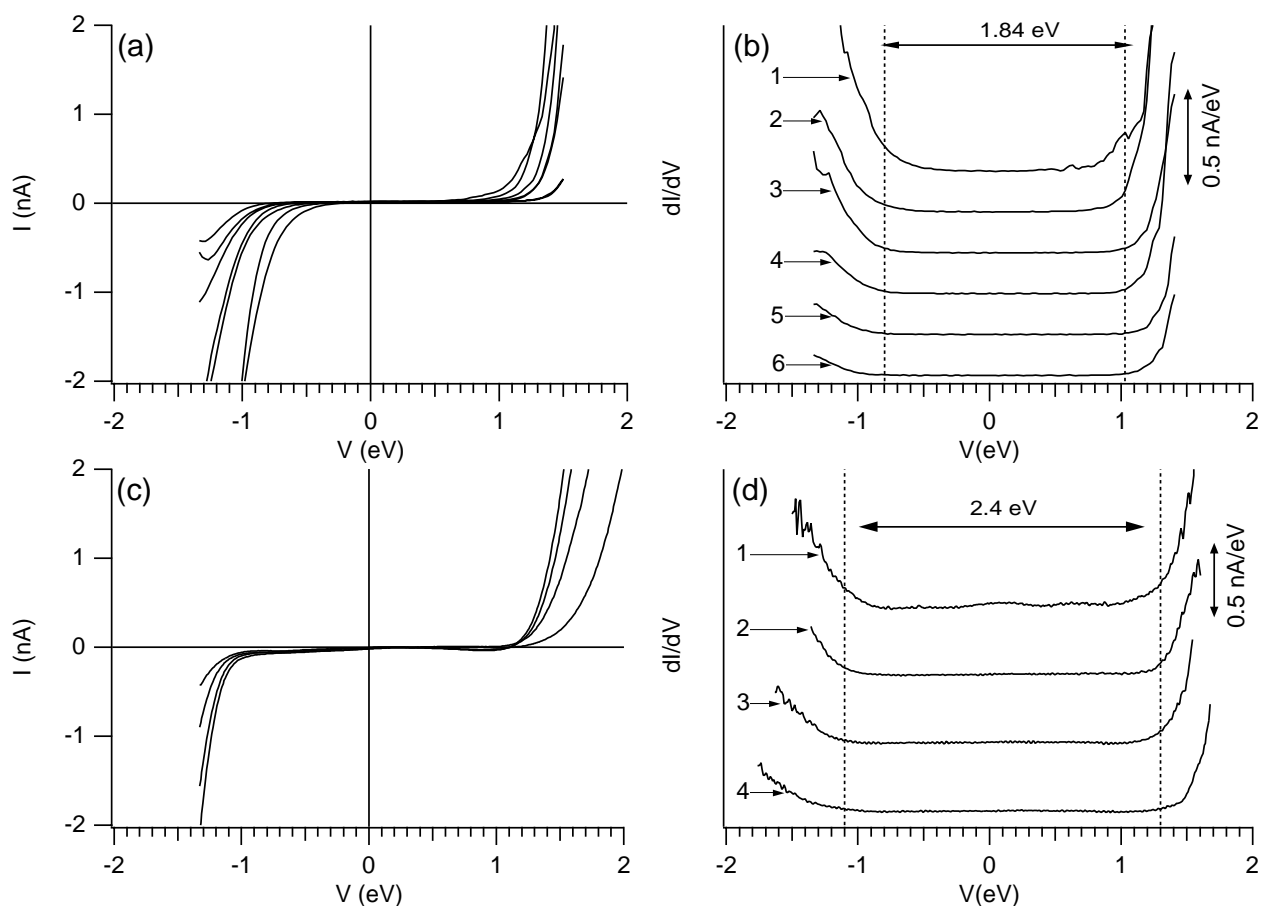


Figure 5.4 (a) and (c) Current-voltage curves obtained under ambient conditions for electrodeposited CdSe and CdS quantum dots on gold, which have a mean diameter of 100 \AA . In Figures (b) and (d) the corresponding tunneling spectra are presented. The tip-to-dot distance was varied by using different set point currents at a given bias. In Figure (b) the bias was 1.3 V and the set point currents (1) 3.0 nA, (2) 1.0 nA, (3) 200 pA, (4) 100 pA, (5) 50 pA, and (6) 20 pA. In Figure (d) the bias was 1.5 V and the set point currents (1) 2.4 nA, (2) 1.0 nA, (3) 500 pA, and (4) 200 pA.

Figures 5.4(b) and 5.4(d) do not show peaks in the regions of increasing conductance. The width of the zero-conductance-gap and the absence of discrete peaks agree well with the fact that 10 nm large dots have an electronic structure which is similar to that of macroscopic single crystals. In the tunneling spectra of the smaller dots discrete peaks were observed; these will be discussed in chapter 6. It should be remarked that the conductance increases more rapidly at positive than at negative bias.

In Figure 5.5 (a) and (c) the current-voltage curves are shown for colloidal CdSe(I) and CdS quantum dots on Au/hexanedithiol-SAM. The diameters of the CdSe and CdS particles, determined with TEM and optical absorption, are 32 ± 5 Å and 50 ± 12 Å; the optical bandgaps of these particles are 2.3 eV and 2.6 eV, respectively. In Figures 5.5(b) and (d) the corresponding tunneling spectra are shown. The width of the zero-conductance-gap depends strongly on the tip-

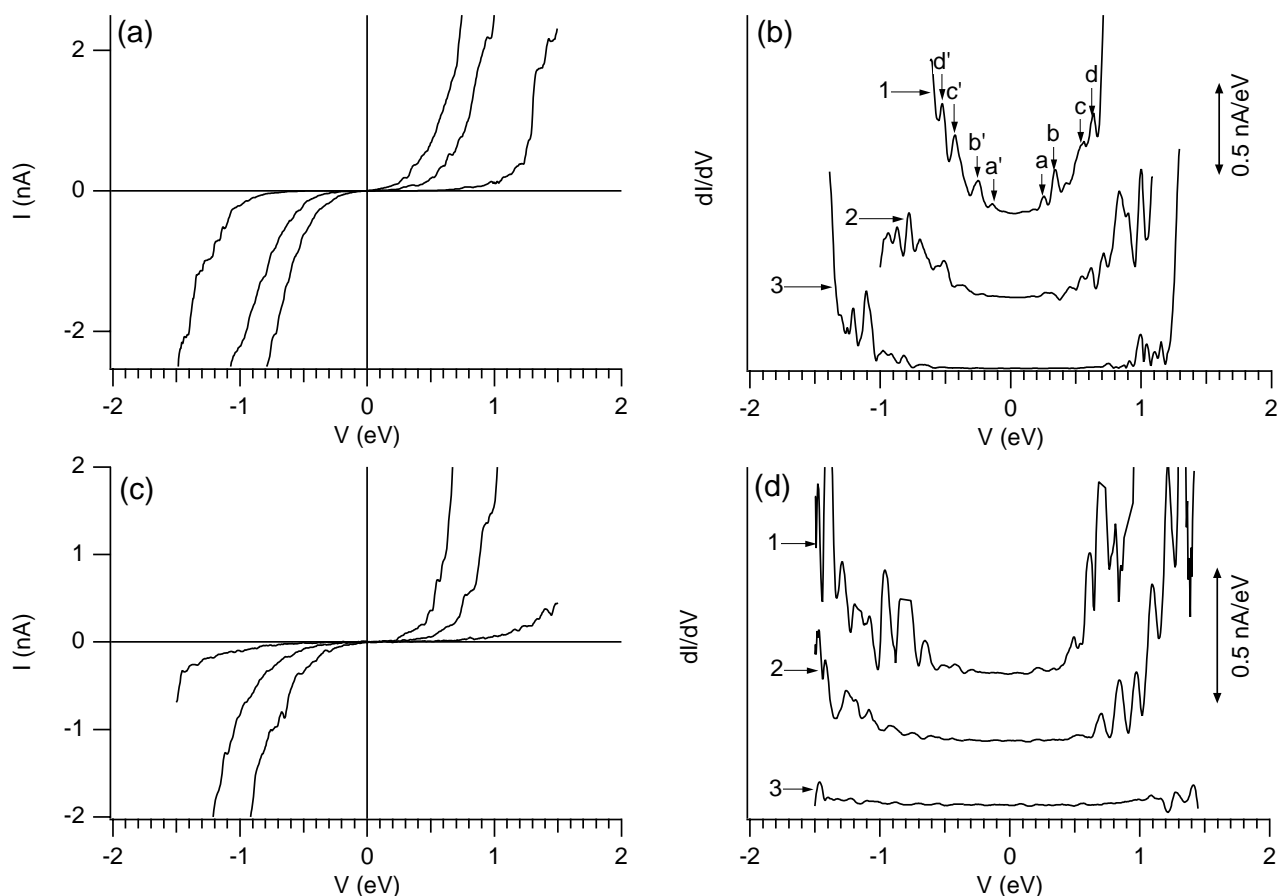


Figure 5.5 (a) and (c) Current-voltage curves obtained under ambient conditions for single colloidal CdSe and CdS quantum dots on Au/SAM, which have a mean diameter of 32 ± 5 Å and 50 ± 12 Å, respectively. In Figures (b) and (d) the corresponding tunneling spectra are presented. The tip-to-dot distance was varied by using different set point currents at a given bias. In Figures (b) and (d) the bias was 1.2 V and the set point currents (1) 2.0 nA, (2) 1.0 nA, and (3) 200 pA.

to-dot distance, in contrast to that measured on the electrodeposited dots. The width of the gap in Figure 5.5(b) decreases from 1.5 eV to 0.3 eV when the current increases from 200 pA to 2.0 nA, and in 5.5(d) the width of the gap is reduced from 2.2 eV to 0.9 eV upon an increase of the set point current from 200 pA to 2.0 nA. Such a strong dependence of the width of the zero-conductance-gap on the tip-to-dot distance has also been observed by others for colloidal CdS quantum dots on Au/SAM.⁷ The spectra obtained with the smallest tip-to-dot distance suggest a shape that is symmetrical with respect to the point $V=0$. The conductance increases sharply at positive and negative bias, in contrast to what was observed for the electrodeposited dots.

In Figures 5.6 (a) and (c) the current-voltage curves, and in (b) and (d) the tunneling spectra obtained on single colloidal CdSe(II) quantum dots in vacuum at 4.2 K are shown. The bias was 1.4 V for both scans, but in Figure 5.6(a) the set point current was 150 pA and in 5.6(c)

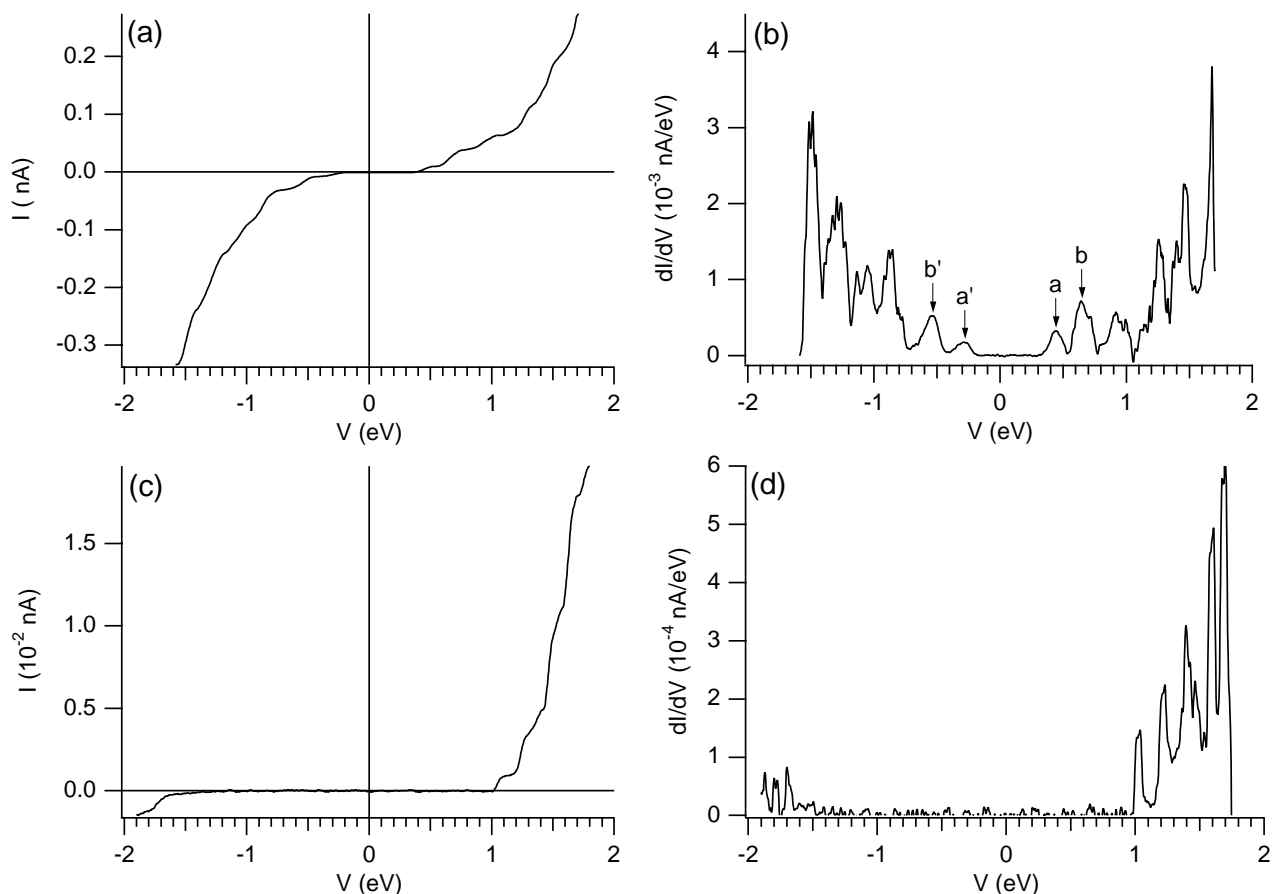


Figure 5.6 (a) and (c) Current-voltage curves obtained in vacuum at 4.2 K for a single colloidal CdSe quantum dot on Au/2-SAM, which has a mean diameter of 43 ± 4 Å. In Figures (b) and (d) the corresponding tunneling spectra are presented. The tunneling settings were (a,b) 150 pA, 1.4 V, and (c,d) 5 pA, 1.4 V.

5 pA. The diameter of these dots was 43 ± 4 Å, corresponding to an optical bandgap of 2.15 eV. The tunneling spectrum presented in Figure 5.6(b) appears to be symmetrical with peaks a-a', b-b' *etc*, which are similar in width and height in the positive and negative bias region. The width of the zero-conductance-gap in Figure 5.6(b) is 0.5 eV. The conductance peaks in the spectrum shown in Figure 5.6(d) in the positive bias region are much higher and better resolved than the peaks in the negative bias region. The width of the zero-conductance-gap is 2.5 eV. The measured peak spacing in Figure 5.6(b) between a-b and a'-b' is 220 and 250 meV and the peak widths (FWHM) for a, b, a' and b' are 120-150 meV. The width of the peaks at positive bias in Figure 5.6(d) is 60 ± 10 meV.

5.4 Discussion

An STM tip positioned above a semiconductor quantum dot forms a DBTJ as shown in Figure 5.1(c). In this electrical equivalent circuit, we assume the dot to be a point with potential ϕ_{dot} , that is located between the two barriers. The tip/dot and dot/Au capacitances are denoted by C_1 and C_2 , respectively. Single electron tunneling events lead to electrical currents J_1 and J_2 ; R_1 and R_2 correspond to the differential resistances of tunneling through the tip/dot and dot/substrate barriers, respectively. The bias ($E_{F,tip} - E_{F,Au}$) is distributed over the tip/dot and dot/Au junctions,

$$E_{F,tip} - E_{F,Au} = e \left[(\phi_{dot} - \phi_{tip}) + (\phi_{Au} - \phi_{dot}) \right] = e\Delta\phi_1 + e\Delta\phi_2 \quad (5.1)$$

in which ϕ_{Au} and ϕ_{tip} are the electrostatic potentials of the gold substrate and the tip and $\Delta\phi_1$ and $\Delta\phi_2$ are the values of the electrical potential drop over the tip/dot and dot/Au barriers. The distribution of the bias ($E_{F,tip} - E_{F,Au}$) over the two junctions can be derived by using Kirchoff's laws.

$$C_2 \frac{d\Delta\phi_2}{dt} + J_2 = C_1 \frac{d\Delta\phi_1}{dt} + J_1 \quad (5.2)$$

From equation (5.1) and (5.2) it follows that the potential drop over the tip/dot junction is given by

$$e d\Delta\phi_1 = \frac{C_2}{C_1 + C_2} d(E_{F,tip} - E_{F,Au}) + e \frac{\int (J_2 - J_1) dt}{C_1 + C_2} \quad (5.3)$$

For a DBTJ with a quantum dot in the ground state, *i.e.* not charged positively by a hole or negatively by an electron, $J_1(t)$ and $J_2(t)$ are both zero. The distribution of the bias is determined by the first term on the right hand side of equation (5.3). The second term accounts for the charging energy, E_C , due to electron (or hole) tunneling into the quantum dot. For instance, if one electron is transferred from the tip to the dot, *i.e.* $\int (J_2 - J_1) dt = -e$, the energy of the dot increases by $E_C = e^2 / (C_1 + C_2)$, for the time interval during which the electron resides on the particle. It has to be remarked here that equation (5.3) and the equation for the charging energy were derived on the basis of an electrical equivalent circuit. The microscopic physics are incorporated in the capacitances C_1 and C_2 . Two contributions to the charging energy should be distinguished; that related to an electron (or hole) interacting with the bonding electrons, *i.e.* the polarisation energy (depending on ϵ_{in} and ϵ_{out} , see Figure 5.7), and Coulomb electron-electron (or hole-hole) interaction for charge carriers in tunneling transition;¹⁷⁻²⁰ this issue will be discussed in more detail in chapter 6.

5.4.1 Asymmetrical DBTJ ($C_2 \gg C_1$)

In the bias range in which the conductance is zero ($J_1 = J_2 = 0$), the quantum dot is in the ground state. If the capacitances of the barriers do not change with the bias we find from equation

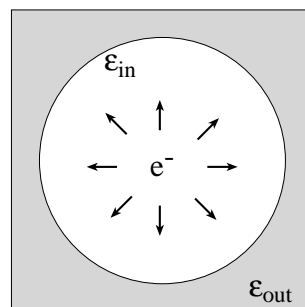


Figure 5.7 Schematic representation of an insulating quantum dot with dielectric constant ϵ_{in} in a dielectric environment with constant ϵ_{out} . The charge of the additional electron is compensated (partly) by the polarisation of the bonding electrons of the dot. The electric field, induced by the additional electron, extends the limited size of the nanocrystal; hence, the polarisation energies of the electron and the hole depend on the dielectric surroundings.

(5.3) that $\Delta\phi_1 = (E_{F,tip} - E_{F,Au}) \frac{C_2}{C_1 + C_2}$ and $\Delta\phi_2 = (E_{F,tip} - E_{F,Au}) \frac{C_1}{C_1 + C_2}$. For dots electrodeposited

directly on the substrate, the Au/QD interface has a high capacitance; the barrier is probably due to a monolayer of elemental selenium. Since $C_2 \gg C_1$ for all tip-to-dot distances, the bias drops entirely over the tip/dot junction. In this situation, a change in the bias results in a corresponding change in $E_{F,tip}$ with respect to the energy levels of the dot; the Fermi level of the gold substrate remains unchanged when the voltage is scanned. Hence, the Fermi level of the tip scans through the energy levels of the nanocrystal as is shown in Figures 5.8(a) and (b). At positive bias resonant tunneling occurs via the conduction band levels of the dot, and at negative bias via the valence band levels.

The effective barrier height ($E_{vac} - E_{F,tip}$ or $E_{vac} - E_{F,Au}$) is expected to be much larger for resonant tunneling from the substrate to the dot (see Figure 5.8(b): $E_{F,Au} > E_{F,tip}$) than for tunneling from the tip to the dot (see Figure 5.8(a): $E_{F,tip} > E_{F,Au}$). As a result, the tunneling probability and hence the conductance should be lower at negative bias than at positive bias (illustrated in Figure 5.8(c)). This effect was clearly observed with electrochemically deposited CdS and CdSe at all tip-to-dot distances and with colloidal CdSe dots when the tip was retracted.

The position of the zero-conductance-gap is nearly symmetrical around zero bias for the asymmetrical Au/dot/tip configuration, indicating that the equilibrium Fermi energy of the system is located in the middle of the bandgap of the particle.

The zero-conductance-gap is the measured difference between the voltage of the first peak at positive and the first peak at negative bias. The width of the gap corresponds to the bandgap of the dot ($E_{LUMO} - E_{HOMO}$) plus the polarisation energies for adding the first electron, E_{e_1} , at positive bias and the first hole, E_{h_1} , at negative bias.¹⁷ The polarisation energies for dots with a diameter of 100 Å are negligible. The measured widths of the gaps at the largest tip-to-dot distance are 1.9 eV and 2.4 eV for CdSe and CdS (Figure 5.4), which is close to the bandgap of the macroscopic semiconductor.

5.4.2 Symmetrical DBTJ ($C_2 \cong C_1$)

A symmetrical DBTJ can be formed if the quantum dot is covalently anchored to the gold substrate by an alkane dithiol, and the tip is positioned at a sufficiently small distance from the

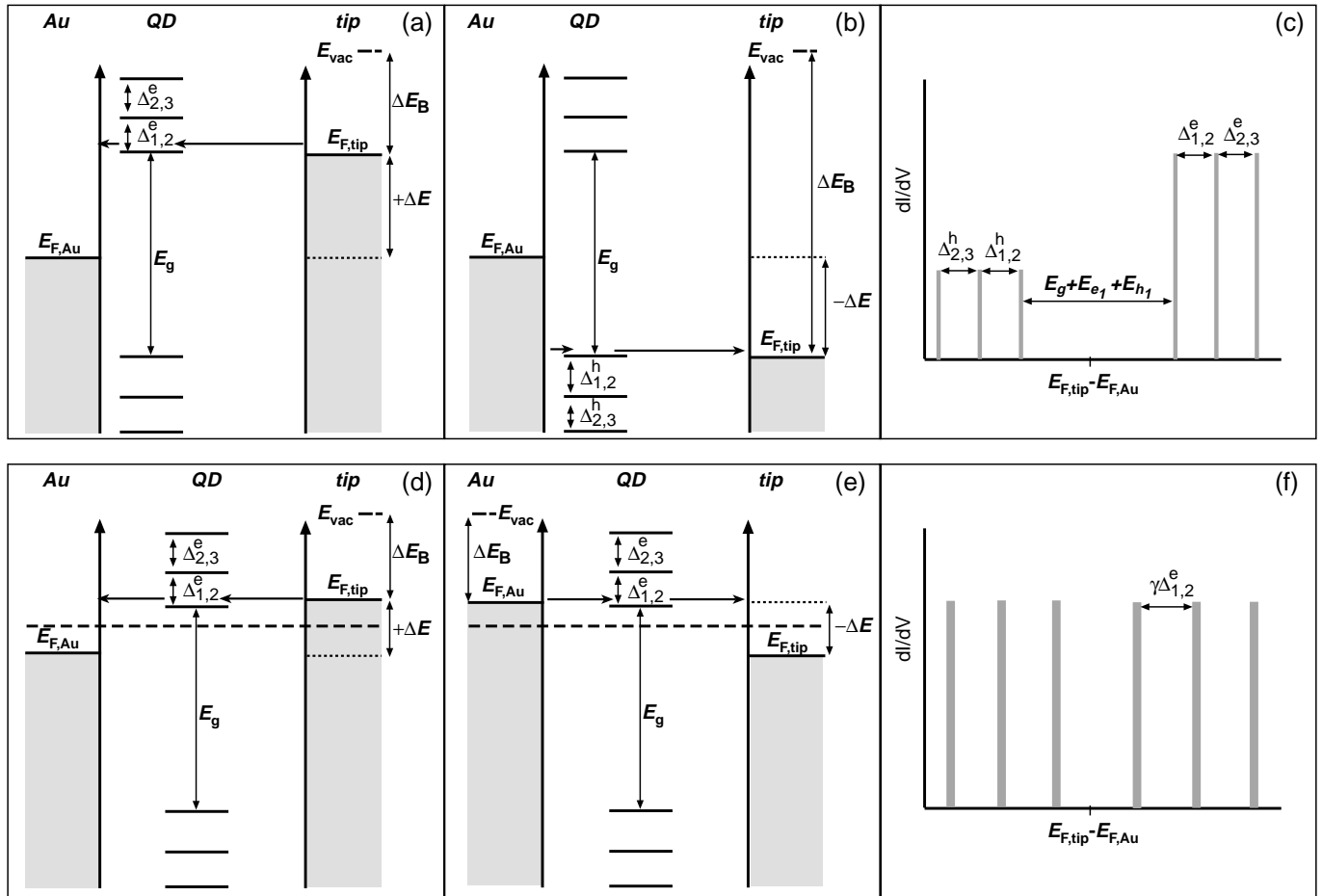


Figure 5.8 (a) and (b) show tunneling at (a) positive and (b) negative bias through the conduction band and valence band levels, respectively, for an **asymmetrical** DBTJ. ΔE is the bias ($E_{F,tip} - E_{F,Au}$), and ΔE_B is the effective barrier height ($E_{vac} - E_{F,tip}$ or $E_{vac} - E_{F,Au}$). In (c) a tunneling spectrum is shown with the characteristic features for an asymmetrical DBTJ. Figures (d) and (e) show the tunneling processes for a **symmetrical** DBTJ at positive and negative bias through the same conduction band level. The Fermi energy level at equilibrium is indicated by the dashed line; due to image charges in the tip and the substrate the energy of the dot is shifted to lower energies (see text). In Figure (f) the tunneling spectrum, characteristic for a symmetrical DBTJ is shown.

dot, such that $C_1 \cong C_2$. From equation (5.3) it follows that for a totally symmetrical DBTJ ($C_1 = C_2$) $\Delta\phi_1 = \Delta\phi_2 = 0.5(E_{F,tip} - E_{F,Au})$, and the bias is distributed equally over the two barriers. If the bias is changed, the Fermi level of the tip and that of the gold substrate will shift with respect to the energy levels of the dot. At positive bias, electrons tunnel resonantly from the tip via a conduction band level in the dot to the gold (Figure 5.8(d)), and at negative bias electrons tunnel via the same conduction band level in the dot, but then in the opposite direction, from the gold substrate to the tip (Figure 5.8(e)). The barrier height for tunneling from the tip to the conduction band level in the dot is the same as that for tunneling from the gold to the same level in the dot.

This means that the tunneling probabilities and hence the differential conductance are the same for both processes; the heights of the peaks in the tunneling spectrum are expected to be the same at positive and negative bias. When $C_1=C_2$, the width of the zero-conductance-gap in the tunneling spectrum does not correspond to the bandgap of the dot, but to four times the energy difference between the equilibrium Fermi level in the gold and the lowest level of the conduction band plus the polarisation energy of the electron (see Figure 5.8). The tip/dot capacitance, C_1 , depends on the tip-to-dot distance, while the dot/Au capacitance is constant and determined by the molecular structure of the barrier. Consequently, the distribution of the bias across the DBTJ depends strongly on the tip-to-dot distance. This effect agrees with the experimental results (see the tunneling spectra in Figure 5.5). The tunneling spectra in Figures 5.5(b) and 5.6(b) show that the equilibrium Fermi level lies very close to the first level of the LUMO of the dot. This experimental fact cannot be explained by the present model. A possible explanation is that the energy of the dot is shifted to lower energy by an electrostatic interaction between the crystal dipole of the dot and the image charges in the tip and the substrate. In Figure 5.8(f) a schematic tunneling spectrum is shown with the characteristic features expected for a symmetrical DBTJ. These features were experimentally observed in Figure 5.6(b).

The tip/dot capacitance, C_1 , was decreased by retracting the tip from the sample, making the DBTJ more asymmetrical as a result. In Figure 5.6(d) a spectrum is shown in which the tip was retracted from the colloidal quantum dot such that $C_2 \gg C_1$. At positive bias, the conduction band levels are probed and at negative bias the valence band levels as indicated by the higher conductance at positive bias. The measured width of the zero-conductance-gap was 2.5 eV, corresponding to $(E_{LUMO} - E_{HOMO}) + E_{e_1} + E_{h_1}$. The bandgap of the dot ($E_{LUMO} - E_{HOMO} = 2.28$ eV) is deduced from the optical bandgap (2.15 eV), observed from the absorption spectrum, by adding the electron-hole Coulomb interaction energy, which is ~ 125 meV (with $r = 2.15$ nm, and $\epsilon_{\infty, \text{CdSe}} = 10$). These results give a value for the sum of the polarisation energies, $E_{e_1} + E_{h_1} = 220$ meV. In Figure 5.6(b) the tunneling spectrum for a similar dot in a symmetrical DBTJ configuration is shown. The measured peak spacings between a-b, and a'-b' are 220 meV and 250 meV, respectively, and correspond to $\gamma\Delta_{1,2}$ ($\gamma = (C_1 + C_2)/C_2$, following from equation (5.3)). The measured peak width (FWHM) in Figure 5.6(d) is 60 ± 10 meV for all the peaks at positive bias, and in Figure 5.6(b), 120-150 meV for the peaks a, a', b, and b', all corresponding to

the first energy level of the conduction band; the measured peak width has doubled for the symmetrical DBTJ.

5.5 Conclusion

We studied resonant electron tunneling in Au/QD/tip configurations with CdS and CdSe quantum dots electrochemically grown on gold and with colloidal CdS and CdSe dots covalently anchored to a gold substrate via a hexanedithiol SAM. In junctions with electrodeposited dots, a change in the bias induces mainly a shift of the Fermi level of the tip with respect to the energy levels of the dot. In such an asymmetrical configuration, the bandgap and energy level spacing can be determined directly from the tunneling spectra. With the Au/SAM/QD systems, the spectra depend strongly on the tip-to-dot distance. With a small distance, a symmetrical spectrum is observed, indicating resonant tunneling via the levels of the conduction band at both positive and negative bias.

References

1. S. Datta, W. Tian, S. Hong, R. Reifenberger, J.I. Henderson, and C.P. Kubiak, *Phys. Rev. Lett.* **1997**, *79*, 2530-2533
2. S. Datta, W. Tian, S. Hong, R. Reifenberger, J.I. Henderson, C.P. Kubiak, *J. Chem. Phys.* **1998**, *109*, 2874-2878
3. P.J.M. van Bentum, R.T.M. Smokers, and H. van Kempen, *Phys. Rev. Lett.* **1988**, *60*, 2543
4. C. Schönenberger, H. van Houten, H.C. Donkersloot, A.M.T. van Putten, and L.G.J. Fokkink, *Physica Scripta* **1992**, *T45*, 289
5. R.P. Andres, T. Bein, M. Dorogi, S. Feng, J.I. Henderson, C.F. Kubiak, W. Mahoney, R.G. Osifchin, and R. Reifenberger, *Science* **1996**, *272*, 1323
6. Y. Kuk, M.F. Jarrold, P.J. Silverman, J.E. Bower, and W.L. Brown, *Phys. Rev. B* **1989**, *39*, 11168-11170
7. S. Ogawa, F.F. Fan, and A.J. Bard, *J. Phys. Chem.* **1995**, *99*, 11182-11189
8. B. Alpers, S. Cohen, I. Rubinstein, and G. Hodes, *Phys. Rev. B* **1995**, *52*, R17017-R17020

9. Miyaki, H. Matsumoto, M. Nishizawa, T. Sakata, H. Mori, S. Kuwabata, and H. Yoneyama, *Langmuir* **1997**, *13*, 742-746
10. U. Banin, Y. Cao, D. Katz, and O. Millo, *Nature* **1999**, *400*, 542-544
11. B. Alperson, I. Rubinstein, G. Hodes, D. Porath, and O. Millo, *Appl. Phys. Lett.* **1999**, *75*, 1751-1753
12. B. Su, V.J. Goldman, and J.E. Cunningham, *Science* **1992**, *255*, 313-315
13. C.B. Murray, D.J. Norris, and M.G. Bawendi, *J. Am. Chem. Soc.* **1993**, *115*, 8706-8715
14. PhD Thesis Jeroen Wildöer, Katholieke Universiteit Nijmegen and Technische Universiteit Delft, **1996**, chapter 2
15. Y. Golan, L. Margulis, G. Hodes, I. Rubinstein, J.L. Hutchison, *Surf. Science* **1994**, *311*, L633-L640
16. R. Wiesendanger, *Scanning Probe Microscopy and Spectroscopy* **1994**, Cambridge University Press, Great Britain
17. A. Franceschetti, A. Williamson, and A. Zunger, *J. Phys. Chem.* **2000**, *104*, 3398-3401
18. A. Franceschetti, and A. Zunger, *Appl. Phys. Lett.* **2000**, *76*, 1731-1733
19. L.E. Brus, *J. Chem. Phys.* **1984**, *80*, 4403-4409
20. L.E. Brus, *J. Phys. Chem.* **1986**, *90*, 2555

Single Electron Tunneling through a CdSe Quantum Dot

Abstract

The electronic structure of a single CdSe quantum dot was studied with Scanning Tunneling Spectroscopy. The STM tip was positioned above a colloidal CdSe nanoparticle, which was anchored to a gold surface, forming a Double-Barrier Tunnel Junction (DBTJ). By varying the tip-to-dot distance the symmetry of the DBTJ could be modified. This has two effects. First, the relative magnitude of the capacitances, which determines the distribution of the bias, is changed (see chapter 5). Second, the probability that a specific orbital of the nanocrystal is occupied with an electron depends on the rates of tunneling into and out of the quantum dot, and relaxation in the nanocrystal. For an asymmetrical DBTJ, the Coulomb charging effects can be neglected; the conductance peaks in the tunneling spectra reflect the set of discrete single-electron levels of the quantum dot. The degeneracy of the levels is not resolved with this configuration. In a more symmetrical DBTJ, the degeneracy of the levels is partly resolved by Coulomb charging of the dots. The electronic structure of a CdSe quantum dot was compared to that calculated for an electron in a cubic box.

6.1 Introduction

In the past decade, the electronic structure of semiconductor,¹⁻⁵ metal,⁶ and superconducting⁷ nanometer-sized crystals has been studied in great detail with electrical devices in which the dot is positioned between three electrodes on an integrated circuit (IC). The advantages of such devices are the robustness of the system and the presence of a third electrode, which can act as a gate electrode. A disadvantage is that parameters such as the tunnel resistances and the capacitances of the Double-Barrier Tunnel Junction are fixed, *a priori*. Another approach to study the electronic structure of a quantised system is to use Scanning Tunneling Spectroscopy (STS). For STS, a nanocrystal is adsorbed on a conducting substrate and the STM tip is positioned above a single particle, forming a Double-Barrier Tunnel Junction (DBTJ). Recently, incremental charging of metal particles, and the electronic properties of semiconductor quantum dots were investigated with STS.⁸⁻¹¹ The main advantage of STS is that the tip-particle distance, and thus the ratios of tunneling resistances and capacitances of the DBTJ, can be changed without changing the particle-substrate distance.^{12,13} The recent development of a scanning gate STM, which has two electrically independent tips, has made it possible to perform gated experiments; this approach has only been used for gold grains.¹⁴

Banin *et al.*¹⁵ and Alpers *et al.*^{16,17} reported on an STS study of colloidal InAs and electrochemically deposited CdSe quantum dots on a gold substrate, respectively. Banin *et al.* mentioned that in their measurements the tip was retracted and it was assumed that the resulting DBTJ was asymmetrical. In the tunneling spectra, a doublet and a sextet were observed. The doublet was assigned to an atomic-like '*s*-orbital' and the sextet to the (three-fold degenerate) '*p*-orbitals'. The authors concluded that the spin and orbital degeneracy was broken due to charging effects. In recent theoretical work, Zunger *et al.*^{18,19} have shown for an insulating nanocrystal, that there are different contributions to the charging energy. When the first electron (or hole) is added to the nanocrystal in the ground state, the energy of the dot is raised by the electron (or hole) polarisation energy. The physical origin of this type of charging energy was discussed in chapter 5. If the deviation from equilibrium is sufficiently large such that more pathways for resonant tunneling are available, electron-electron Coulomb interactions can form another contribution to the charging energy.

In this work, the electronic structure of individual colloidal CdSe nanoparticles was investigated with STS. The symmetry of the DBTJ was changed systematically by varying the tip-dot distance. The symmetry of the DBTJ has consequences not just for the potential distribution over the two barriers (see the previous chapter). In addition, we found that a change

in the tip-dot distance in such a configuration has a strong effect on the conductance spectra in the positive bias region, where electrons tunnel through the levels of the conduction band. It will be shown that in an asymmetrical configuration the electron-electron Coulomb charging effects can be neglected. The set of conductance peaks reflects the energy diagram of electron levels in the conduction band; degenerate energy levels are not resolved. This chapter presents the first STS study in which the electron occupation configuration of the nanocrystal, which may not be in equilibrium with the Fermi level of the source electrode (in this case the STM tip), is considered. In a symmetrical DBTJ Coulomb charging effects are important and the degeneracy is lifted.

6.2 Experimental

The colloidal TOPO-capped CdSe quantum dots were prepared according to the method described in chapter 5 for the CdSe(II) suspension. The TOPO-capping of the CdSe nanocrystals could be replaced by a pyridine capping.

Type (I) samples. The original suspension of TOPO-capped dots ($d=43\pm 4$ Å) was evaporated to dryness under argon and the particles were redissolved in pyridine, which replaces the TOPO. This pyridine capping could be subsequently replaced by hexanedithiol by adding a drop of hexanedithiol to the pyridine solution. The particles were interconnected by the hexanedithiol molecules forming 'supercrystals', which precipitated. These 'supercrystals' were destroyed by ultrasonic vibration; the individual dots could be redissolved in anhydrous methanol. A gold surface was provided with a submonolayer of quantum dots by placing a flame-annealed gold sample in the methanol solution for 16 hours. The samples were rinsed thoroughly with methanol.

Type (II) samples. The gold samples were annealed and provided with a SAM of compound **2**(4,4'-(tetrahydro-4H-thiopyran-ylidene)) as described in chapter 4. A submonolayer of TOPO-capped quantum dots was attached to this SAM as described in chapter 5.

All Scanning Tunneling Spectroscopy experiments described in this chapter were performed in vacuum at 4.2 K with the STM set up described in chapter 5.

6.3 Results

Figure 6.1 shows an STM image of hexanedithiol-capped CdSe quantum dots on Au(111) terraces obtained in vacuum at 4.2 K. The gold surface was covered with a sub-monolayer of

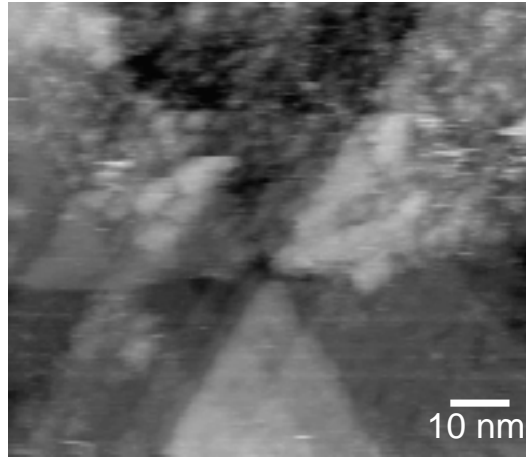


Figure 6.1 STM image of a Au(111) surface covered with a sub-monolayer of CdSe quantum dots (type I) sample) measured in vacuum at 4.2 K (20 pA at 1.4 V). The area shown is 99×85 nm.

nanoparticles. For STS, isolated dots were selected and for reference measurements tunneling spectra were recorded on the bare gold terraces.

In Figure 6.2, the tunneling spectra acquired above a single CdSe quantum dot are shown for an asymmetrical configuration ((a, c and d) set point 5 pA, 1.4 V). The dots used for Figures 6.2(a),(c) and (d) were capped with TOPO and deposited on a 2-SAM (see chapter 4) on gold. In Figure 6.2(b) a spectrum is shown (50 pA, 1.5 V) for a hexanedithiol-capped nanocrystal, anchored to a bare gold surface. The peaks at positive bias, corresponding to the conduction band levels of the quantum dot are shown in more detail in the insets. In all spectra five main peaks were observed at positive bias with peak spacings $\Delta_{1,2} = 188 \pm 8$ meV, $\Delta_{2,3} = 194 \pm 15$ meV, $\Delta_{3,4} = 150 \pm 20$ meV, and $\Delta_{4,5} = 92 \pm 12$ meV. The relative intensity of the peaks was different in spectra taken consecutively above a single dot. The peaks at negative bias, corresponding to the valence band levels, had a much lower intensity than the peaks at positive bias and were not well-resolved. The width of the zero-conductance-gap in Figures 6.2(a), (c), and (d) is 2.5 ± 0.1 eV.

In Figure 6.3, two consecutive tunneling spectra obtained above the same quantum dot at different tip-dot distances are shown. Spectrum (a) (1.4 V, 30 pA) shows 6 peaks in the positive bias region. The peak spacings in spectrum (a) were $\Delta_{1,2} = 181$ meV, $\Delta_{2,3} = 188$ meV, $\Delta_{3,4} = 100$ meV, $\Delta_{4,5} = 85$ meV and $\Delta_{5,6} = 167$ meV. The peak observed in spectrum (a) at a bias of 770 meV was absent in spectrum (b) (1.4 V, 10 pA); the relative intensity of the peaks did not reproduce.

Figure 6.4 shows tunneling spectra for single quantum dots after the tip is brought closer to the dot with respect to the spectra shown in Figure 6.2 and 6.3 (more symmetrical DBTJ). In all spectra the main peaks were followed by satellite peaks of decreasing intensity. The spacing between the main peaks in the spectra was $I = 316 \pm 13$ meV, $II = 207 \pm 8$ meV, and

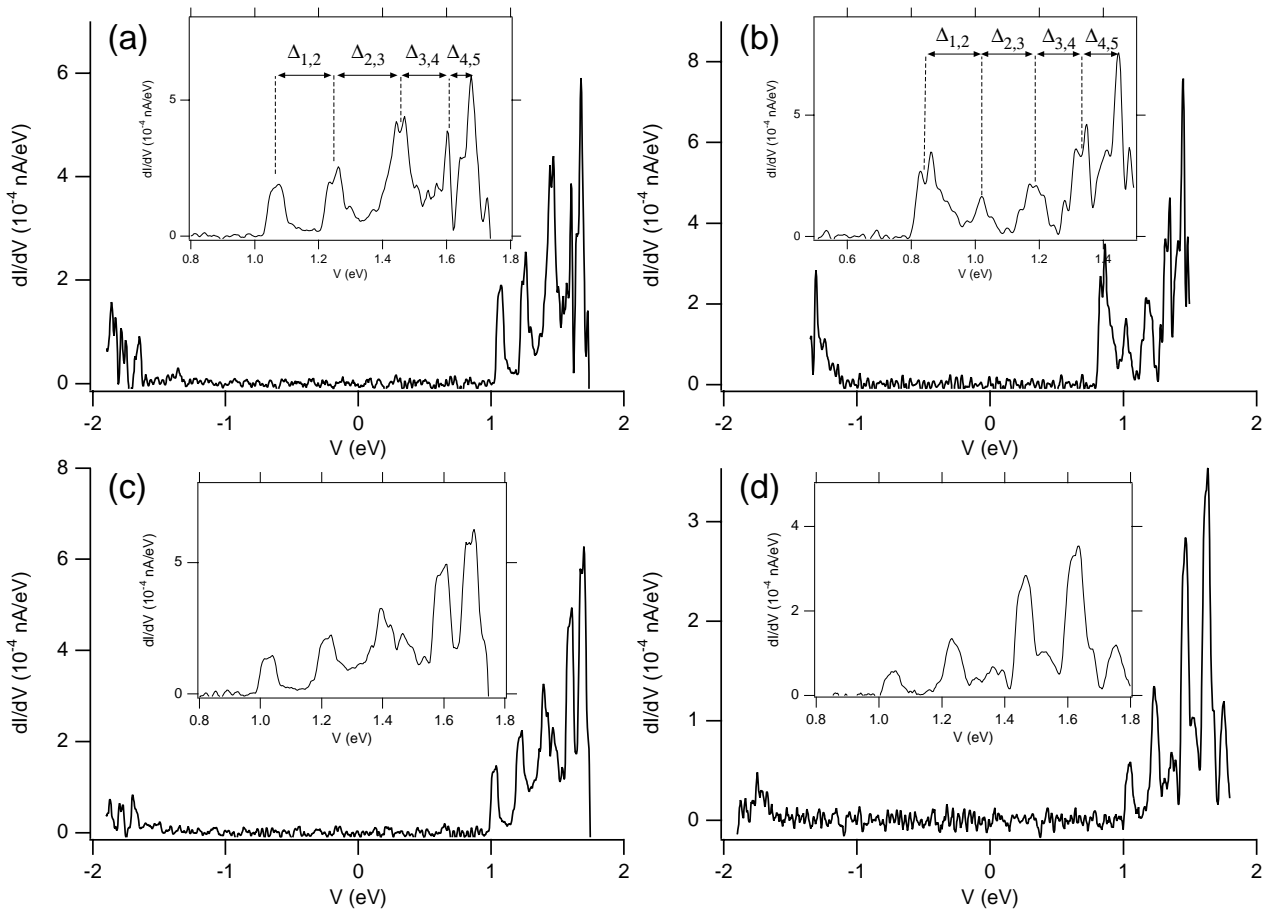


Figure 6.2 Tunneling spectra obtained on a CdSe quantum dot in vacuum at 4.2 K for Figures (a), (c), (d) TOPO-capped dots on a 2-SAM on gold with a set point current of 5 pA at 1.4 V, and (b) on a hexanedithiol-capped nanocrystal on bare gold with a current set point of 50 pA at 1.5 V. In the insets the peaks at positive bias are shown in more detail.

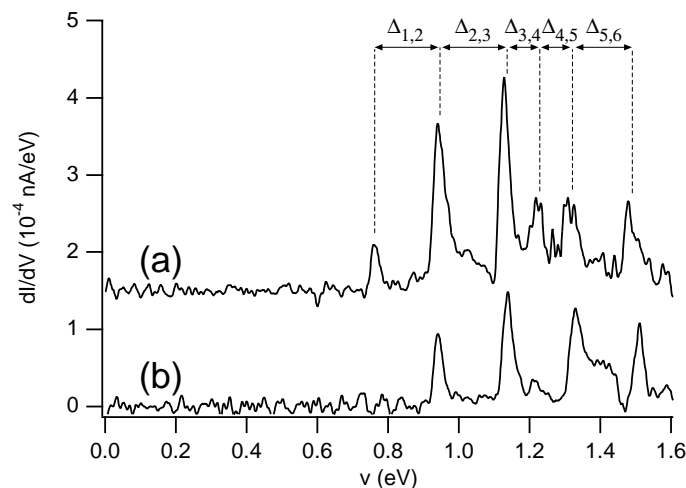


Figure 6.3 Consecutive tunneling spectra on a quantum dot at different tip-dot distances. Spectrum (a) (set point 30 pA at 1.4 V) shows six peaks in the positive bias region. The peak at 770 meV in spectrum (a) is absent in spectrum (b) (set point 10 pA at 1.4 V). The relative intensities of the peaks are different in both spectra.

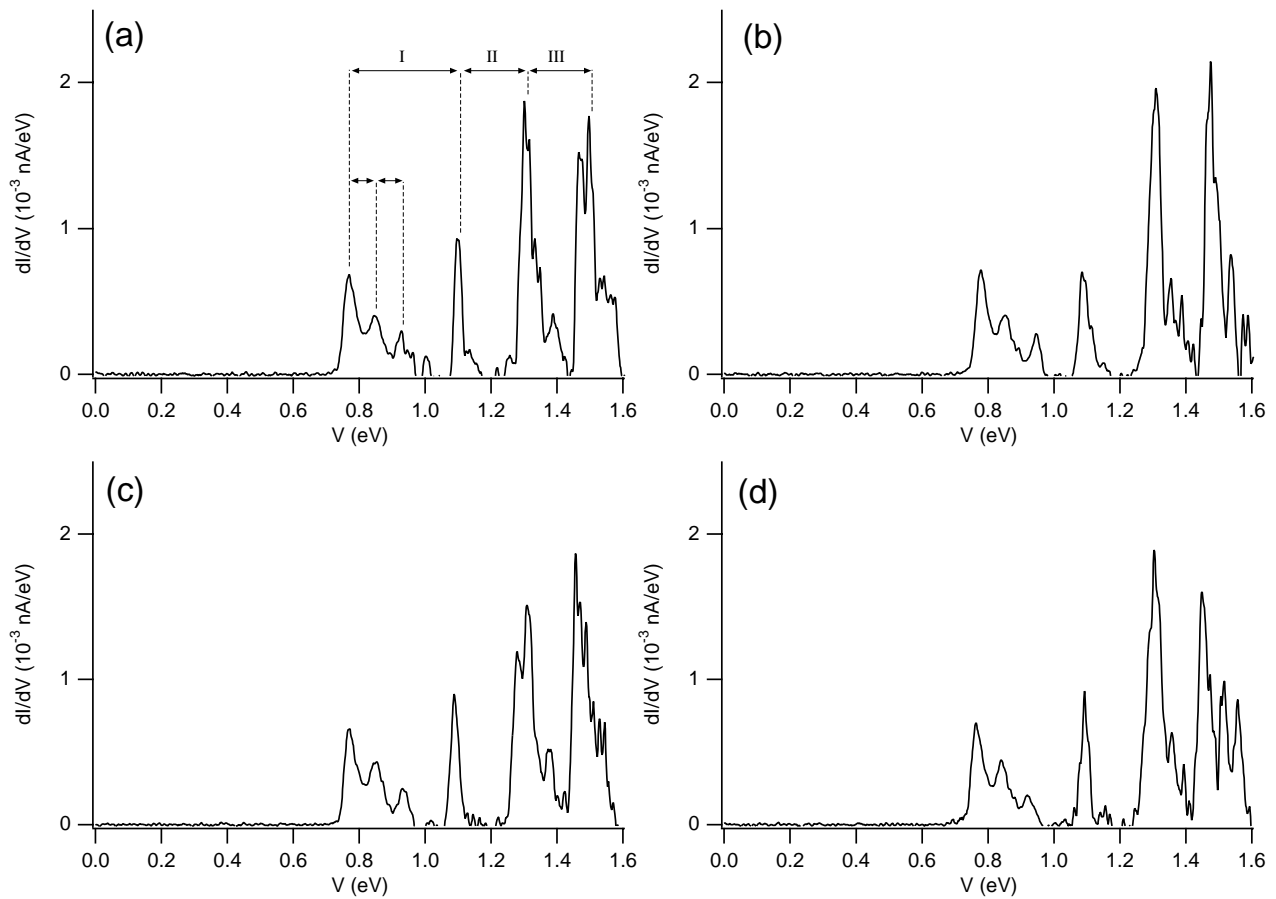


Figure 6.4 Tunneling spectra obtained on single CdSe quantum dots in a symmetrical DBTJ configuration in vacuum at 4.2 K (60 pA at 1.2 V).

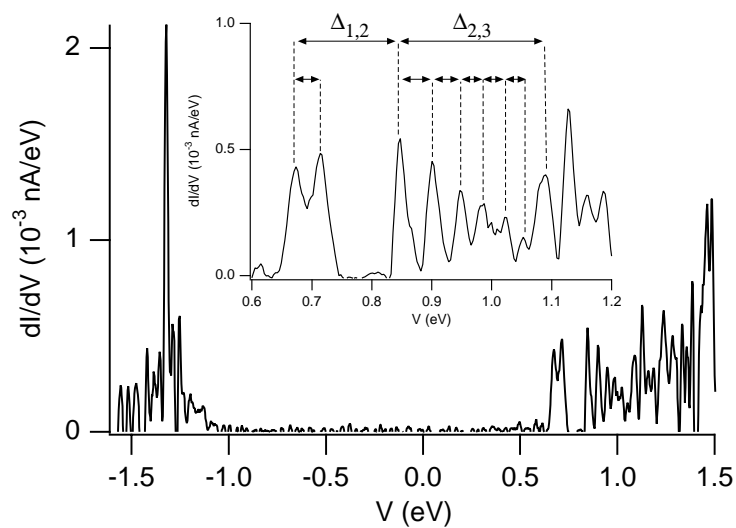


Figure 6.5 Tunneling spectrum obtained on a single CdSe quantum dot in a symmetrical DBTJ configuration in vacuum at 4.2 K (80 pA at 1.5 V).

$\Gamma=160\pm 10$ meV. The typical spacing between the satellite peaks was 75 ± 10 meV. After each set of peaks, there is a small regime with a negative differential conductance.

In Figure 6.5, a tunneling spectrum for an even smaller tip-to-dot distance is shown. In the positive bias range two peaks are observed, followed by a series of six peaks with decreasing intensity. In the inset the peaks are shown in more detail. The spacing between the main peaks was $\Delta_{1,2}= 173$ meV, and $\Delta_{2,3}= 247$ meV and the spacing of the satellite peaks was typically 40 ± 10 meV. The peaks at negative bias have an intensity similar to that of the peaks at positive bias. As discussed in chapter 5, this indicates that resonant tunneling involves the same levels of the nanocrystal at positive and negative bias.

6.4 Discussion

6.4.1 Energy levels for an electron in a cubic box

In section 1.2.2, the quantum size effect was explained by considering an electron in a spherical box with infinitely high walls. In this section we will use, for simplicity, the model of a particle confined in a rectangular volume of dimensions L_1 , L_2 , and L_3 in the x , y , and z -directions. The Schrödinger equation is given by equation (1.1); U , the potential energy of the electron, is zero everywhere in the box, except at the walls. The kinetic energy of the electrons is then given by,

$$E_{n_1, n_2, n_3} = \left(\left(\frac{n_1}{L_1} \right)^2 + \left(\frac{n_2}{L_2} \right)^2 + \left(\frac{n_3}{L_3} \right)^2 \right) \frac{h^2}{8m_e} \quad (n_1=1, 2, \dots; n_2=1, 2, \dots; n_3=1, 2, \dots) \quad (6.1)$$

with the independent quantum numbers n_1 , n_2 , and n_3 . The degeneracy of the energy levels and the energy level splitting are related to the symmetry and dimensions of the potential well. In Figure 6.6 the electron energy scheme for a cubic box ($L_1=L_2=L_3=L$) is shown. The first level is non-degenerate, whereas the following three levels are three-fold degenerate. The degeneracy of the first and second level is the same as for a spherical quantum box, where the orbitals are denoted by s and p (as for atoms).^{20,21}

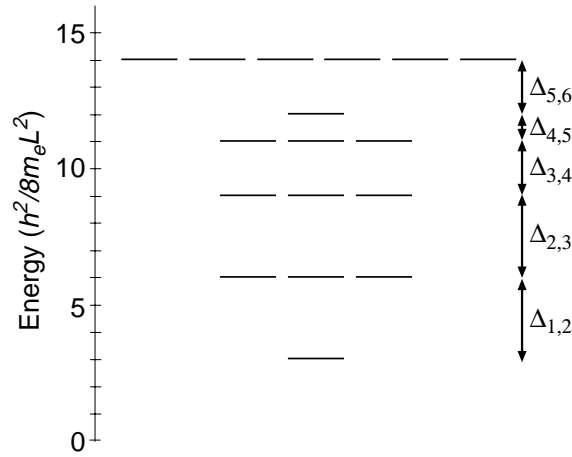


Figure 6.6 Energy scheme for an electron in a cubic box ($L_1=L_2=L_3=L$). The potential energy of the electron is zero everywhere in the box, except at the walls, where it is infinite.

6.4.2 The energy required to add electrons to an insulating nanocrystal

In a recent paper, Zunger and coworkers calculated the energy required to add electrons to the discrete levels of a semiconducting nanocrystal, taking into account the single-electron energy level spectrum and the charging energy.^{18,19} They estimated two different contributions to the charging energy: the polarisation energy and Coulomb interaction between electrons. The model of Zunger forms a basis for the interpretation of tunneling spectra. We consider a nanocrystal in the ground state (no electrons in the CB) and an electron reservoir (source electrode) with a reference Fermi-level, E_F^{ref} . We then consider how much this Fermi-level has to be increased to put one, two and more electrons into the discrete energy levels of the conduction band of the nanocrystal under conditions of electronic equilibrium. The shift of the reference Fermi-level required to put a first electron onto a quantum dot in the lowest discrete level in the energy region of the conduction band is

$$E_F^{(1)} - E_F^{ref} = e_1 + E_{e_1} \quad (6.2)$$

where e_1 is the energy of the electron level with respect to the reference energy and E_{e_1} the polarisation energy of the first electron added to the nanocrystal. E_{e_1} depends on the dielectric constant of the quantum dot, ϵ_{in} , and of the surrounding medium, ϵ_{out} . An analogous equation holds for the energy required to add the first hole to a nanocrystal in level h_1 with a polarisation energy E_{h_1} . The addition energy to put a second electron with opposite spin in the same energy level is

$$\Delta E_{1,2} = E_F^{(2)} - E_F^{(1)} = E_{e_2} + E_{e-e} \quad (6.3)$$

where E_{e-e} is the Coulomb interaction energy between the electrons. The polarisation energy for the second electron, E_{e_2} , is due to the interaction with the image charge of the first electron and is probably different from E_{e_1} . The addition energy to charge the dot with a third electron in the next level is

$$\Delta E_{2,3} = E_F^{(3)} - E_F^{(2)} = e_2 - e_1 + E_{e_3} + 2E_{e-e} \quad (6.4)$$

where E_{e_3} is the interaction energy of the third electron with the image charges of the other two electrons and e_2 is the energy level. The addition energy for placing the fourth electron on the particle can be considered in an analogous way. Here, the spin-spin energies are neglected, since they are much smaller than the Coulomb interaction energies.

6.4.3 Non-equilibrium dynamics in a metal/dot/metal device

In section 6.4.2, the energies involved in adding electrons to the degenerate and non-degenerate energy levels of a semiconducting nanocrystal are considered. In the model it is assumed that when an electron is added to a given energy level, the electrons which have already been added are all still present. It is hence assumed that the energy levels of the nanocrystal have an occupation that is in chemical (electronic) equilibrium with the source electrode (*i.e.* the electrode with the highest Fermi-level). In this work we only discuss tunneling through the conduction band levels of the nanocrystal; the source electrode then corresponds to the STM tip. In this section we will consider the possibility that the system is not in equilibrium.

The occupation of the energy levels in a nanocrystal during electron transport

The relative rates of electron tunneling into and out of the dot, and relaxation in the dot determine the probability that a given orbital is occupied. This probability determines the probability of interactions between (tunneling) electrons in the crystal, and hence the charging energy. For the interpretation of the charging effects it is necessary to define the probability that an orbital, i , is occupied with an electron,

$$\langle f^i \rangle = \frac{k_{in}^i}{k_{in}^i + k_{out}^i} \quad (6.5)$$

in which k_{in}^i and k_{out}^i are the rate constants for electron tunneling to and from the dot, respectively; k_{in}^i is the number of tunneling events per second from the source into the i^{th} orbital of the nanocrystal. These rate constants depend exponentially on the tunneling distance (equation (1.15)). For simplicity, relaxation of an electron from one orbital to another is not taken into account.²² For configurations in which $k_{out}^i \gg k_{in}^i$, the probability that an orbital is occupied with an electron is very small and Coulomb interactions between two electrons in tunneling transition located in the dot can be neglected. As a result, degenerate levels cannot be resolved. If the tip is brought sufficiently close to the dot, such that k_{in}^i is of the same order of magnitude or larger than k_{out}^i , the probability that a given orbital is occupied is non-zero. Under these conditions, interactions between two (or more) tunneling electrons become important. Due to these interactions the spin and orbital degeneracy lifts.

Equilibrium conditions

To reach electronic equilibrium between the nanocrystal and the source electrode (here the tip), tunneling from the tip into the nanocrystal must be faster than tunneling of electrons from the nanocrystal to the substrate, *i.e.* per orbital $k_{in}^i \gg k_{out}^i$. Under these conditions, the occupation of the orbitals in the nanocrystal is in equilibrium with the source electrode; this means that all energy levels below $E_{F,tip}$ are occupied. In order to load a second and third electron onto the nanocrystal, the addition energies $\Delta E_{1,2}$ and $\Delta E_{2,3}$ are required, respectively, and the spin degeneracy is removed; this situation is illustrated in Figure 6.7.

Non-equilibrium conditions

When $k_{out}^i \gg k_{in}^i$, the probability that an orbital i is occupied with an electron is low (see equation (6.5)). Hence, electron-electron Coulomb interaction is negligible. This means that the spin and orbital degeneracy is not resolved in the tunneling spectrum, and the spectrum reflects the single electron energy scheme of the nanocrystal (see Figure 6.9). In the non-equilibrium situation, electron relaxation to lower levels (rate constant k_r) is slower than electron tunneling from the dot to the gold ($k_{out}^i \gg k_r$); as a result, the occupation of the orbitals of the dot is not in

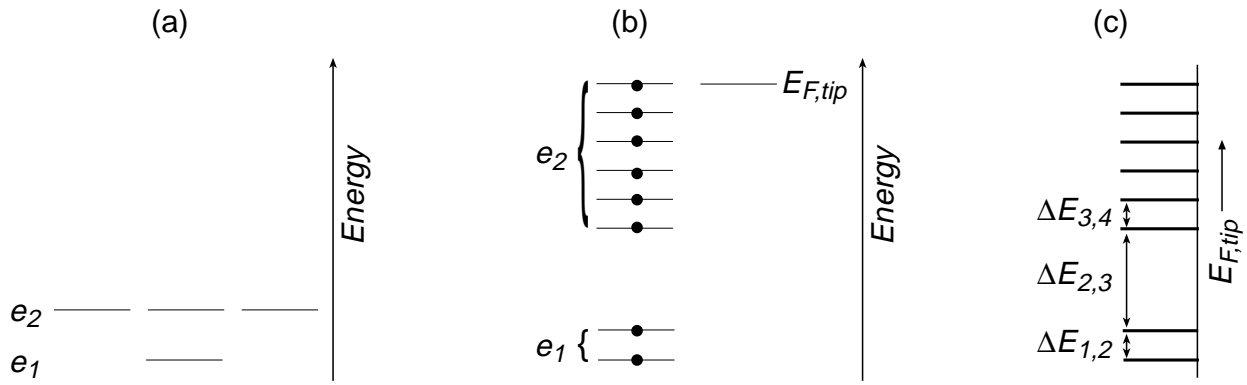


Figure 6.7 Schematic representation of the effects of electron-electron Coulomb interactions on the tunneling spectrum. In (a) the lowest two single electron levels of the conduction band are shown; e_1 is non-degenerate, and e_2 is three-fold degenerate. (b) shows the energy spectrum when the levels are fully occupied and electron-electron Coulomb interactions are strong. (c) shows the expected position of the peaks in the tunneling spectrum; it is clear that electron-electron Coulomb interaction lifts the spin and orbital degeneracy.

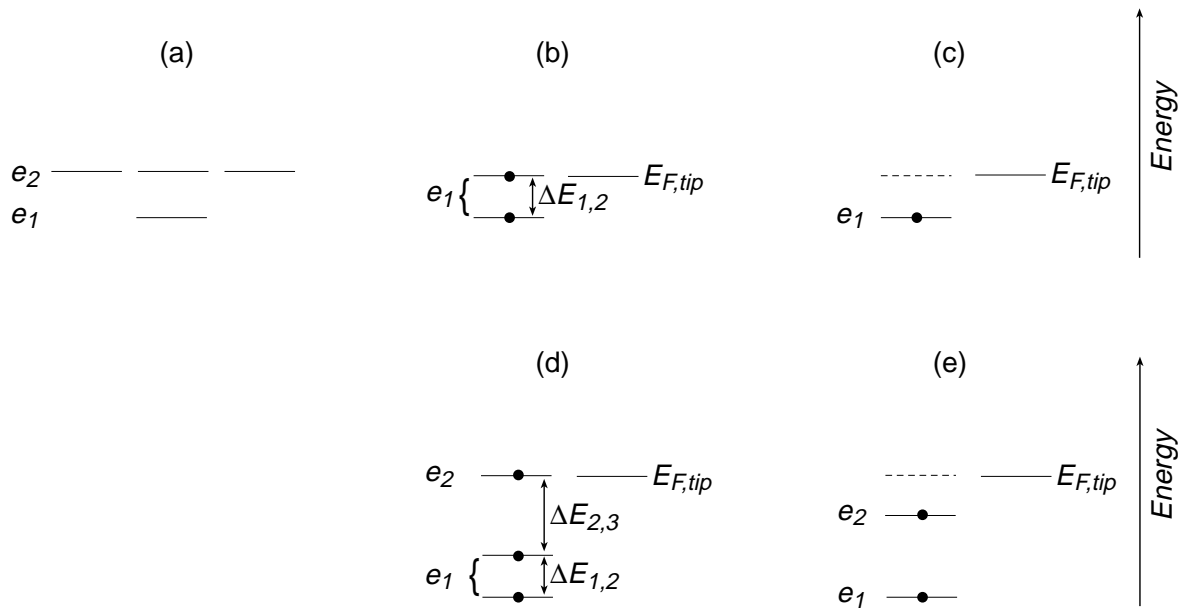


Figure 6.8 Possible occupation configurations of the electron levels during tunneling, compared to the full occupation. (a) shows the single electron level scheme, e_1 is non-degenerate and e_2 is three-fold degenerate. (b) and (c) show the situation where $E_{F,tip}$ is sufficiently high to overcome $\Delta E_{1,2}$; (b) full occupation: due to electron-electron Coulomb interaction the spin degeneracy is resolved. (c) only one electron is present in e_1 ; the spin degeneracy is not resolved. In (d) and (e) $E_{F,tip}$ is sufficiently high such that e_1 can be occupied with two electrons and e_2 with one electron. (d) shows the configuration where there is full occupation of e_1 and one electron is in one of the e_2 orbitals (equilibrium with the source electrode). (e) shows the situation that e_1 and e_2 are occupied by one electron. Due to the missing electron in e_1 , resonant tunneling through e_2 occurs at lower energy.

equilibrium with the source electrode. Alivisatos *et al.* have found a relatively long lifetime for spin relaxation in CdSe quantum dots (nanoseconds);²³ this might lead to non-equilibrium effects in STS. Tinkham *et al.*²² found that in metal grains different electron occupancy configurations are possible; the energy of the single-electron states will be shifted by a value, different for each occupancy configuration. The resulting tunneling spectra may consequently be very complex. Figures 6.8 (c) and (e) present possible configurations, in which the system is not in equilibrium.

6.4.4 Interpretation of the Tunneling Spectra

If the tip is retracted, the tip-dot distance may be much larger than the dot-substrate distance (Figures 6.2 and 6.3). For tip-to-substrate tunneling via the orbitals of the nanocrystal (positive bias), the rate constant for tunneling between the dot and the substrate, k_{out}^i , is much larger than that between the tip and the dot, k_{in}^i ; therefore the probability that the dot is occupied by an electron is nearly zero, and electron-electron Coulomb interaction can be neglected. In this case only the polarisation energy of the first electron and hole will be observed, contributing to the width of the zero-conductance-gap (see chapter 5). The zero-conductance-gap corresponds to the bandgap of the dots plus the polarisation energies of the electron and the hole, $E_g + E_e + E_h$. Since charging effects are insignificant, degenerate energy levels are not resolved. Very importantly, the tunneling spectrum reflects the single-electron spectrum of the nanocrystal (see Figure 6.9). For such an asymmetrical DBTJ ($C_2 \gg C_1$), the bias drops entirely over the tip-dot junction and consequently, the peak width and level spacing of the conduction band levels ($\Delta_{1,2}^e$ etc.) and valence band levels ($\Delta_{1,2}^h$ etc.) can be determined directly from the measured tunneling spectra (for $k_{out}^i \gg k_{in}^i$). In the spectra shown in Figure 6.2, five peaks were observed in the positive bias region. The relative peak spacings correspond fairly well to the energy level splitting calculated for a particle in a cubic box. From the peak spacing, we estimate $L = 60 \text{ \AA}$, which is in fair agreement with the TEM measurements ($d = 43 \pm 4 \text{ \AA}$). The fact that the peak spacing corresponds to dimensions larger than those found with TEM measurements, indicates that the extension of the electron wave functions should be taken into account. It is reasonable to assume that the first peak corresponds to the first non-degenerate electron level, the second peak to the three-fold degenerate level etc.. We remark that the peaks at negative bias, corresponding to the valence band levels, are not resolved. This is probably due to the complex electronic structure of the valence band of CdSe.²⁻⁴ Spectrum (a), shown in Figure 6.3, gives six peaks at positive bias, their position is in fair agreement with the electron energy levels calculated for an

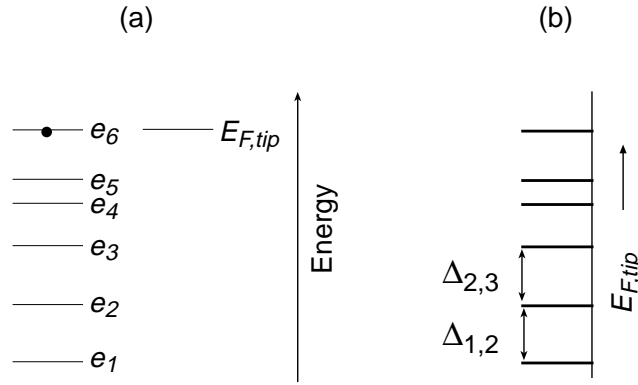


Figure 6.9 (a) The single-electron energy level spectrum and (b) the expected position of the conductance peaks in the tunneling spectrum for a minimum occupation of the dot ($k_{out}^i \gg k_{in}^i$). The spin and orbital degeneracy is not lifted due to electron-electron Coulomb interaction; (b) the peak position in the tunneling spectrum reflects to the single-electron level spectrum.

electron in a cubic box. For spectrum (b) the tip has been further retracted with respect to its position for spectrum (a) (tunnel resistance increased) and the intensity of the first peak has decreased. The probability density or spatial distribution of the orbital involved in tunneling may be important for the tunneling probability. The first level has an s -orbital character and the maximum of the probability density is in the centre of the dot. The next three-fold degenerate level has a p -orbital character and the probability of the electron wave function is distributed more uniformly over the dot. If the tunnel junction has a very high resistance, the wave function of the electron in the tip decays rapidly. Consequently, the orbitals with a low probability density at the surface, as the first s -type level, should have a low tunneling probability.

The spectra acquired with a more symmetrical DBTJ presented in Figure 6.4 give four main peaks at positive bias with satellite peaks. We assume that in this situation $k_{out}^i \cong k_{in}^i$ and charging effects become important. The first peak has at least two satellite peaks and therefore cannot correspond to the first non-degenerate level, which would give a main peak and one satellite peak, separated by $E_{e_2} + E_{e-e}$, the Coulomb charging energy and the polarisation energy for adding the second electron (see Figure 6.7). The value for E_{e_2} may be very small, since the second electron is not added to an insulator, but to a quantum dot which contains one electron and thus has a high free electron density. The first set of peaks might correspond to the second three-fold degenerate level, indicating that the first non-degenerate level is not observed in these experiments. The peak spacing of the satellites corresponds to the total charging energy, multiplied by a factor, which is due to the fact that the bias is distributed over two junctions. The charging energy is of the order of 40 meV, a value which was also observed by Alivisatos *et al.*

for CdSe nanocrystals of comparable size.²⁻⁴ By using $e^2/4\pi\epsilon\epsilon_0R$, with $R=60 \text{ \AA}$, a value for the charging energy of 48 meV was calculated, which is in reasonable agreement with the experiments; we obtained $L=60 \text{ \AA}$ from the single-electron energy level spectrum. The spectrum in Figure 6.5 was measured for a relatively small tip-dot distance and shows two peaks followed by a series of six peaks. The first two peaks correspond to the first non-degenerate level and are split by the Coulomb charging effect. The next six peaks correspond to the second three-fold degenerate energy level. The peak splitting of the main peaks was $\sim 170 \text{ meV}$ and that of the satellite peaks is $\sim 40 \text{ meV}$. The spectrum in Figure 6.5 agrees with the spectrum deduced in Figure 6.7 for full occupancy of the orbitals.

The decreasing intensity of the satellite peaks must be related to electron-electron interactions, and hence to the occupancy of the orbitals. For instance, the probability that a second electron tunnels into orbital $i+1$, when orbital i is occupied, is given by $\langle f^i \rangle \times \langle f^{i+1} \rangle$, hence

$$\frac{k_{in}^i}{k_{in}^i + k_{out}^i} \times \frac{k_{in}^{i+1}}{k_{in}^{i+1} + k_{out}^{i+1}} \leq 1.$$

6.5 Conclusion

It is shown that the symmetry of the Double-Barrier Tunnel Junction is a key factor for single electron tunneling in a semiconductor quantum dot. The probability that an orbital is occupied by an electron is determined by the rate constants for tunneling to and from the dot and hence by the distances between the tip and the dot, and between the dot and the substrate. For a very asymmetrical DBTJ ($C_2 \gg C_1$), the Coulomb interactions can be neglected and degenerate energy levels cannot be resolved. The tunneling spectrum reflects the single-electron energy spectrum of the nanocrystal, which can be understood in terms of the model for an electron in a cubic box. For a symmetrical DBTJ Coulomb charging effects become important and the degeneracy of electron energy levels can at least partly be resolved. The fact that Banin *et al.*¹⁵ and Alpers *et al.*¹⁶ resolved completely the degeneracies of the first two levels, indicates that the DBTJ in their experiments was symmetrical.

References

1. M.A. Kastner, *Nature* **1997**, 389, 667
2. D.L. Klein, R. Roth, A.K.L. Lim, A.P. Alivisatos, and P.L. McEuen, *Nature* **1997**, 389, 699

3. D.L. Klein, P.L. McEuen, J.E. Bowen Katari, R. Roth, and A.P. Alivisatos, *Appl. Phys. Lett.* **1996**, 68, 2574
4. H. Weller, *Angewandte Chemie* **1998**, 110, 1748-1750
5. M.A. Kastner, *Physics Today* **1993**, januari, 24-31
6. D.C Ralph, C.T. Black, and M. Tinkham, *Phys. Rev. Lett.* **1995**, 74, 3241-3244
7. D.C Ralph, C.T. Black, and M. Tinkham, *Phys. Rev. Lett.* **1997**, 78, 4087-4090
8. H. van Houten, and C.W.J. Beenakker, *Phys. Rev. Lett.* **1989**, 63, 1893-1896
9. P.J.M. van Bentum, R.T.M. Smokers, and H. van Kempen, *Phys. Rev. Lett.* **1988**, 60, 2543
10. R.P. Andres, T Bein, M. Dorogi, S. Feng, J.I. Henderson, C.F. Kubiak, W. Mahoney, R.G. Osifchin, and R. Reifengerger, *Science* **1996**, 272, 1323
11. C. Schönenberger, H van Houten, H.C. Donkersloot, A.M.T. van Putten, and L.G.J. Fokkink, *Physica Scripta* **1992**, T45, 289
12. D.V. Averin, K.K. Likharev, *Mesoscopic Phenomena in Solids* **1991**, edited by B.L. Altshuler, P.A. Lee, and R.A. Webb, Elsevier, New York
13. B. Su, V.J. Goldman, and J.E. Cunningham, *Science* **1992**, 255, 313-315
14. L. Gurevich, L. Canali, and L.P. Kouwenhoven, *Appl. Phys. Lett.* **2000**, 76, 384-386
15. U. Banin, Y. Cao, D. Katz, and O. Millo, *Nature* **1999**, 400, 542-544
16. B. Alpersn, I. Rubinstein, G. Hodes, D. Porath, and O. Millo, *Appl. Phys. Lett.* **1999**, 75, 1751-1753
17. B. Alpersn, S. Cohen, I. Rubinstein, and G. Hodes, *Phys. Rev. B* **1995**, 52, R17017-R17020
18. A. Franceschetti, A. Williamson, and A. Zunger, *J. Phys. Chem.* **2000**, 104, 3398-3401
19. A. Franceschetti, and A. Zunger, *Appl. Phys. Lett.* **2000**, 76, 1731-1733
20. P.W. Atkins, *Physical Chemistry* **1990**, Oxford University Press, Great Britain
21. S.V. Gaponenko, *Optical Properties of Semiconductor Nanocrystals* **1998**, Cambridge University Press, United States of America
22. O. Agam, N.S. Wingreen, B.L. Altshuler, D.C. Ralph, and M. Tinkham, *Phys. Rev. Lett.* **1997**, 78, 1956-1959
23. J.A. Gupta, D.D. Awschalom, X. Peng, and A.P. Alivisatos, *Phys. Rev. B* **1999**, 59, R10421-R10424

Samenvatting

Een 'quantum dot' is een kristallijne structuur waarvan de afmetingen in drie dimensies zijn beperkt, zodat de golffuncties van de elektronen opgesloten zijn in dit volume. De typische afmetingen van een dergelijke structuur zijn in de orde van enkele nanometers (10^{-9} m). Door de opsluiting van de elektrongolffunctie in een beperkt volume, treedt er 'size-quantisation' op. Dit effect is al in 1926 waargenomen, maar werd pas in de jaren tachtig juist geïnterpreteerd en beschreven. De elektronische structuur van metaal- en halfgeleiderkristallen verandert wanneer deze structuren extreem klein worden gemaakt. De continue energiebanden van een macroscopische halfgeleider worden opgesplitst in discrete energieniveaus, en de verboden zone of de 'bandgap', het energieverval tussen de geleidingsband en valentieband, wordt groter naarmate de afmetingen van het nanokristal afnemen. Dit 'size-quantisation' effect maakt deze quantum dots erg interessant voor fundamenteel onderzoek, maar ook voor technologische toepassingen.

Een metaal of halfgeleider quantum dot kan bijvoorbeeld worden gebruikt in een 'Single Electron Transistor', een elektronische schakeling waarin slechts één of enkele elektron(en) kunnen worden opgeslagen. Wanneer deze schakelingen reproduceerbaar op een geïntegreerd circuit kunnen worden gefabriceerd, kan dat leiden tot een verdere miniaturisering van de huidige elektronica. Halfgeleider nanokristallen kunnen ook worden toegepast in een 'Light Emitting Diode' (LED), een diode die licht uitzendt. De uitgezonden golflengte kan worden bepaald door de deeltjesgrootte of de chemische samenstelling van de gebruikte quantum dots te variëren.

Sinds 1960 zijn er allerlei technieken ontwikkeld om quantum dots te fabriceren. Gekwantiseerde structuren kunnen op vaste stof substraten worden opgedampt of van een éénkristal kan materiaal worden weggeëtst, zodat er een nanokristallijn materiaal over blijft. Quantum dots kunnen ook als colloïden op een nat-chemische manier worden bereid. Het afgelopen decennium hebben chemici de monodispersiteit in grootte en vorm van de deeltjes veel verbeterd. Aanvankelijk werden suspensies van deze nanokristallen bestudeerd met optische spectroscopie, zoals absorptie spectroscopie en fotoluminescentie. Met deze techniek kan alleen informatie over de collectieve eigenschappen van de deeltjes worden verkregen. Wanneer er een verdeling van deeltjesgrootte is, zijn de emissielijnen inhomogeen verbreed. Met de 'Scanning Probe' technieken zoals 'Scanning Tunneling Microscopy' of 'Scanning Near-Field Optical Spectroscopy' kunnen de elektrische of optische eigenschappen van individuele deeltjes worden bestudeerd, waarbij problemen, veroorzaakt door de polydispersiteit, kunnen worden voorkomen.

In dit proefschrift zijn de optoelektronische eigenschappen van halfgeleider quantum dots en de ladingsoverdracht tussen de nanokristallen en een geleidend substraat op een nieuwe manier bestudeerd. Hiervoor werd een (sub)monolaag van deeltjes afgezet op een vlak goud oppervlak. De optoelektronische eigenschappen zijn onderzocht met een tijds-opgeloste fotoelektrochemische techniek en de individuele elektronische structuur van de deeltjes is bestudeerd met 'Scanning Tunneling Spectroscopy' bij kamer temperatuur en onder kryogene omstandigheden.

Voor de fotoelektrochemische experimenten wordt een goud elektrode bedekt met een monolaag van deeltjes. Dit systeem wordt als werkelektrode in een fotoelektrochemische cel gebruikt. De spanning over het systeem is gedefinieerd ten opzichte van de referentie-elektrode, en de stroom tussen de werk- en tegenelektrode wordt gemeten. Elektrisch contact tussen de werk- en tegenelektrode wordt bewerkstelligd door het elektrolyt. Wanneer een halfgeleider wordt belicht met fotonen van voldoende energie kan een elektron worden geëxciteerd vanuit de valentieband naar de geleidingsband. Dit heeft als gevolg dat er een gat (elektronvacature) aanwezig is in de valentiebandniveaus en een elektron in de geleidingsbandniveaus. Deze ladingsdragers kunnen recombineren, waarbij een foton wordt uitgezonden. Wanneer een halfgeleider quantum dot, die in nauw contact staat met een metaal, wordt belicht, kunnen de ladingsdragers 'tunnelen' naar het metaal. In de hoofdstukken 2, 3 en 4 wordt respectievelijk het werk aan de licht-geïnduceerde ladingsoverdracht tussen CdS, PbS en CdSe quantum dots en een goud elektrode beschreven. Een voorwaarde voor de ladingsoverdracht tussen het nanokristal en het metaal is dat het elektron-gat paar niet te snel recombineert. In de literatuur wordt een langlevende aangeslagen toestand in CdS en CdSe nanokristallen beschreven. In een dergelijke toestand wordt minstens één van de ladingsdrager ingevangen (getrapt) in een gelokaliseerde plaats in of op de quantum dot. De precieze elektronische structuur van zo'n langlevende aangeslagen toestand kan niet worden bepaald met optische spectroscopie. Met fotoelektrochemische metingen, waarbij ladingsoverdracht tussen de halfgeleider deeltjes en het metaal plaatsvindt, is deze toestand bestudeerd voor de verschillende halfgeleidende nanokristallen. De resultaten waren in overeenstemming met de data verkregen met optische spectroscopie. In CdS en CdSe nanokristallen wordt het gat ingevangen in een niveau, gelegen in de bandgap, en het elektron blijft in de geleidingsband. In PbS quantum dots wordt juist het elektron gelokaliseerd in een bandgap niveau en blijft het gat in de valentieband. De resulterende toestanden hebben een relatief lange levensduur (milliseconden) en een lagere energie dan het oorspronkelijke elektron-gat paar. Een stationaire (constante) anodische of kathodische fotostroom werd waargenomen wanneer respectievelijk een reductor (tartraat) of oxidator

(ijzer(III)cyanide) aan het elektrolyt werd toegevoegd. In dat geval vindt er ladingsoverdracht plaats tussen de quantum dots en het redoxkoppel in het elektrolyt.

Met tijdsopgeloste fotoelektrochemie kunnen de snelheidsconstanten van de tunnelprocessen worden bepaald. In het CdS/Au en CdSe systeem was het tunnelen van het elektron in de geleidingsband van het deeltje naar de goudelektrode het snelste proces. In het PbS/Au systeem was het tunnelen van een elektron vanuit het goud naar het gat in de valentieband het snelste proces. Door de temperatuur te variëren, kan onderscheid worden gemaakt tussen tunnelprocessen en elektrochemische ladingsoverdracht. De snelheid van een tunnelproces is in principe onafhankelijk van de temperatuur, in tegenstelling tot een elektrochemische reactie. Een wiskundig model is opgesteld en vergeleken met de experimentele resultaten. De resultaten impliceerden dat niet-getrapte ladingsdragers een grotere tunnelwaarschijnlijkheid hebben dan getrapte ladingsdragers; een mogelijke verklaring hiervoor zou kunnen zijn dat de niet-getrapte ladingsdragers vrij kunnen bewegen en enkel tunnelen bij een minimale tunnelafstand. De gemiddelde tunnelafstand is dan kleiner voor de niet-getrapte dan voor de getrapte ladingsdragers.

Het doel van het onderzoek dat wordt beschreven in hoofdstuk 4 is het bestuderen van de afstandsafhankelijkheid van tunnelprocessen. Hiervoor werd een monolaag van CdSe deeltjes afgezet op een laag geordende organische moleculen. Er werd een serie niet-rigide dithiol- en een serie rigide disulfidemoleculen gebruikt. De afstandsafhankelijkheid werd bestudeerd door de dikte van de organische laag te variëren en met tijdsopgeloste fotoelektrochemie de snelheidsconstanten van de tunnelprocessen te bepalen. Een groot voordeel van dergelijke systemen is dat de lichtgeïnduceerde ladingsoverdracht niet thermisch wordt geactiveerd. In het algemeen is thermische activatie een groot probleem voor de interpretatie van afstandsafhankelijke ladingsoverdracht. Wanneer de afstand tussen donor en acceptor wordt gewijzigd, veranderen in de meeste andere systemen de moleculaire- en omgevingseigenschappen en daarmee ook de (vrije) reactie- en activeringsenergie. Met de niet-rigide dithiolmoleculen waren de gemeten snelheidsconstanten afhankelijk van de potentiaal, maar niet van de ketenlengte van de dithiolmoleculen. Waarschijnlijk vervormt de organische laag wanneer een spanning wordt aangelegd, waardoor de afstand tussen de quantum dots en het goud verandert en dus niet goed is gedefinieerd. Met de rigide disulfidemoleculen werd een exponentieel verband gevonden tussen de tunnel snelheidsconstanten en de tunnel afstand. Een waarde van 0.5 \AA^{-1} werd gevonden voor β , de parameter die de afstandsafhankelijkheid beschrijft. Deze waarde was laag vergeleken met

waarden gevonden voor metaal/vacuüm/metaal systemen (2.0 \AA^{-1}). Zeer waarschijnlijk zijn de elektron golf functies in de CdSe quantum dots gekoppeld aan die in het metaal via de σ -orbitalen van de cyclohexylidenen en de π -orbitalen van de dubbele bindingen in de spacer moleculen. Met fotoelektron spectroscopie is aangetoond dat de vrije π -type orbitalen van de terminale sulfide groepen een sterke interactie met elkaar hebben.

In de hoofdstukken 5 en 6 wordt 'Single Electron Tunneling' door CdSe en CdS quantum dots bestudeerd met behulp van 'Scanning Tunneling Spectroscopy'. De STM tip wordt boven een individuele dot geplaatst, waardoor een Dubbele-Barriere Tunnel Junctie (DBTJ) wordt gevormd; de DBTJ bestaat uit de tip/dot en de dot/substraat overgangen. In hoofdstuk 5 is de invloed van de elektronische koppeling tussen het deeltje en het substraat op de resulterende tunnel-spectra bestudeerd. Door gebruik te maken van verschillende depositiemethoden was het mogelijk om de elektronische koppeling tussen de dots en het substraat te variëren. Er was een veel sterkere koppeling tussen elektrochemisch gegroeide dots en het substraat dan tussen de dots en de tip (asymmetrische DBTJ); de aangelegde spanning tussen de tip en het substraat valt dan voornamelijk over de tip/dot junctie. Het Fermi niveau van het substraat is constant ten opzichte van de energieniveaus in de quantum dot. In dit geval vindt er resonante tunneling plaats door de valentiebandniveaus bij negatieve potentiaal en door de geleidingsbandniveaus bij positieve potentiaal. Het energiegebied waarin het geleidingsvermogen heel laag is, correspondeert met de verboden zone van het halfgeleiderdeeltje. De grootte van dit energiegebied was onafhankelijk van de tip/dot afstand. Als colloïdale halfgeleiderdeeltjes op een organische laag op het goud worden afgezet, is de dot/Au koppeling vergelijkbaar met de tip/dot koppeling (symmetrische DBTJ). In dit geval wordt de spanning verdeeld over beide juncties en geschiedt resonante tunneling door de geleidingsbandniveaus voor zowel positieve als negatieve spanningen. De resulterende tunnelspectra zijn symmetrisch en de grootte van het energiegebied waarin het geleidingsvermogen heel laag is, hangt sterk af van de tip/dot afstand.

In hoofdstuk 6 is de elektronische structuur van individuele quantum dots onderzocht bij kryogene temperaturen. De symmetrie van de DBTJ is niet alleen van belang voor de spanningsverdeling over het systeem, maar ook voor de verhouding tussen de snelheidsconstanten van tunneling vanuit en naar het deeltje. Deze verhouding tussen de snelheidsconstanten bepaalt de bezettingswaarschijnlijkheid van een orbitaal van het nanokristal met een elektron. De snelheidsconstante voor tunneling tussen de tip en de dot is exponentieel afhankelijk van de tip/dot afstand. Wanneer elektrontunneling van de dot naar het substraat veel

sneller is dan tunneling van de tip naar de dot, is deze waarschijnlijkheid zeer laag; Coulomb opladingseffecten spelen dan nauwelijks een rol. De elektron niveaus van de geleidings- en valentieband kunnen worden gemeten, maar de ontarding van de niveaus kan niet worden opgelost. De gemeten elektronische structuur voor colloïdale CdSe deeltjes kan worden beschreven met het model voor een elektron in een kubische doos. Wanneer de tunnelsnelheden ongeveer gelijk zijn, is de waarschijnlijkheid dat een niveau bezet is door een elektron niet nul, en worden Coulomb opladingseffecten belangrijk. Door de oplading worden de spin- en orbitaal-ontarde niveaus opgesplitst.

List of Publications

G.H. Schoenmakers, E.P.A.M. Bakkers, J.J. Kelly, 'Electroless Etching of ZnSe in Aqueous Ferricyanide Solutions', *J. Electrochem. Soc.* **1997**, *144*(7), 2329-2335

E.P.A.M. Bakkers, E. Reitsma, J.J. Kelly, D. Vanmaekelbergh, 'Excited State Dynamics In CdS Quantum Dots Adsorbed on a Gold Electrode', *J. Phys. Chem. B* **1999**, *103*, 2781-2788

H. Kuiken, E.P.A.M. Bakkers, H. Ligthart, J.J. Kelly, 'The Rotating Ring-Ring Electrode: Theory and Experiment', *J. Electrochem. Soc.* **2000**, *147*(3), 1110-1116

E.P.A.M. Bakkers, J.J. Kelly, D. Vanmaekelbergh, 'Time-Resolved Photoelectrochemistry on PbS Quantum Dots on Gold', *J. Electroanal. Chem.* **2000**, *482*, 48-55

E.P.A.M. Bakkers, A.W. Marsman, L.W. Jenneskens, D. Vanmaekelbergh, 'Distance-dependent Electron Transfer in Au/Spacer/Q-CdSe-Assemblies', *Angew. Chem. Int. Ed.* **2000**, *39*, 2297-2299; 'Abstandsabhängiger Elektronentransfer in Au/Spacer/Q-CdSe-Anordnungen', *Angew. Chem.* **2000**, *112*, 2385-2388

E.P.A.M. Bakkers, A.L. Roest, A.W. Marsman, L.W. Jenneskens, L.I. de Jong-van Steensel, J.J. Kelly, D. Vanmaekelbergh, 'Characterization of Photoinduced Electron Tunneling in Au/SAM/Q-CdSe Systems by Time-Resolved Photoelectrochemistry', *J. Phys. Chem. B* **2000**, *104*, 7266-7272

E.P.A.M. Bakkers, D. Vanmaekelbergh, 'Resonant Electron Tunneling Through Symmetrical and Asymmetrical Double-Barrier Tunnel Junctions', accepted for publication in *Phys. Rev. B*, *62*(7) (rapid communication)

E.P.A.M. Bakkers, L. Canali, L. Gurevich, M. Janus, L.P. Kouwenhoven, D. Vanmaekelbergh, 'Single Electron Tunneling Through CdSe Quantum Dots', to be submitted

Dankwoord

Nu dit boekje bijna klaar is, moet het belangrijkste stukje nog geschreven worden. Ten eerste wil ik mijn promotoren John en Daniel bedanken voor hun uitstekende begeleiding. Daniel, altijd even ambitieus en enthousiast, wist alvorens er ook maar een letter op papier stond (of soms voordat er een meting was verricht) naar welk tijdschrift een manuscript moest worden gestuurd. Ik sta er nog steeds versteld van hoe jij als electrochemicus, fysici van fysisch-onorthodoxe theorieën kunt overtuigen. Hiernaast heb je me ook nog wat kennis over onze zuiderburen bijgebracht; Belgen schijnen 'belgenmoppen' zelf het meest te waarderen. John was niet alleen een meester op het wetenschappelijke gebied maar ook op het sportieve vlak; uiteindelijk is het me dan toch een keer gelukt om met squashen van je te winnen. Mede dankzij jullie flexibele instelling is van mijn oorspronkelijke onderzoeksvoorstel niets terechtgekomen; het werk aan de nanokristallijne halfgeleiderdeeltjes bleek toch uitdagender.

Hans Ligthart, het technische genie van de vakgroep, had voor elk probleem een gepaste oplossing. Hij was niet alleen onontbeerlijk op de vakgroep, maar ook op het sportveld en zelfs bij ons thuis wanneer er een vloertje opgekrikt of gelegd moest worden. De andere technicus, Paul Jurrius, zorgde voor een humoristisch onderhoud tijdens het bewerken van een goudplakje. En mede dankzij Stephan Zevenhuizen werd het werken met een Macintosh een stuk makkelijker.

De (toenmalige) studenten Leon Coulier, Eric Reitsma, Aarnoud Roest, Floris van Driel en Didi Derks wil ik bedanken voor hun inspanning tijdens hun hoofd- of bijvak en de bijdragen aan dit proefschrift. Aarnoud is toch wel een bijzonder geval; na je studie werd je niet alleen een collega, maar ook nog kamergenoot op de meest rumoerige kamer van het Ornstein. Helaas heb ik gisteren onze weddenschap verloren, want je hebt nu een keer gewonnen en gelijkgespeeld met squashen; eigenlijk moeten we een nieuwe weddenschap aangaan met verhoogde inzet! Naast de sportieve bezigheden vond ik de wederzijdse bemoeienissen met elkaars werk erg nuttig en inspirerend. Floris en Didi, jullie wens ik veel plezier in Rome en Parijs, respectievelijk. De keuzepacticum studenten Iris Borkent, Mara Teerink, Jan-Jaap de Roo en Bert van Vugt hebben de basis gelegd voor het 3^e hoofdstuk van dit proefschrift en ik ben ze daar dan ook zeer erkentelijk voor.

Peter Bressers ben ik dankbaar voor de verkennende experimenten met de quartz micro balans en Ben Ern  voor de XPS metingen. Hoewel deze experimenten het idee over onze monolagen versterkten, zijn de resultaten niet opgenomen in dit proefschrift.

Het STM werk, dat zeker achteraf erg belangrijk voor dit proefschrift is gebleken, had zijn oorsprong in het Forschungszentrum (KFA) te J lich. I would like to thank Renate Hiesgen and

Dieter Meissner for the time they have spend with me, doing the STM measurements. Dit STM werk werd voortgezet in Utrecht bij de sectie Chemie aan Grensvlakken; ik ben Liesbeth van Steensel en Hilde Rinia dan ook erg dankbaar voor het feit dat ik regelmatig gebruik mocht maken van de overbezette opstelling. In combinatie met Alwin (Albert?) Marsman en Leo Jenneskens moet ik Liesbeth van Steensel nogmaals noemen voor het leuke werk aan de SAM's, waar uiteindelijk veel resultaten uit gekomen zijn. Hoewel we sinds een jaar in onze eigen sectie een STM opstelling voorhanden hebben, ben ik voor de Tunneling Spectroscopie experimenten uitgeweken naar de TU in Delft. Ik vond het erg leuk en leerzaam om enkele maanden in de groep van Leo Kouwenhoven met Leonid Gurevich, Luca Canali en Michael Janus samen te werken op dit grensgebied van chemie en fysica.

Omdat er naast de 'Science' ook nog een leven is, wil ik Leon, Mark, Emile, Monique en Carola vermelden voor de vele squashpartijtjes, maar ook voor de steeds luxer wordende weekendjes weg; eerst in een gammele stacaravan op Ameland, vervolgens met een leuke tent kamperen in de Ardennen en de laatste keer in een enorm huis in het Geuldal; wat gaan we dit jaar doen? Graag wil ik ook Arjan, en de gebroeders Kramer noemen voor de gezellige badminton en unihockey avondjes. De Cruiffiaanse wedstrijdanalyses van Arjan zijn echt onverbeterlijk. Ik weet eigenlijk nog steeds niet wie van ons tweeën nu vaker in slaap is gevallen tijdens al die videomarathons.

Naast alle reeds genoemde leden van de vakgroep wil ik ook Andries, Xinghua, Paul, Francois, Willem, Freek, Marcel, Ageeth, Koert, Jeroen, Otto, Gijs en oudleden Ferry, Stefan, Addy (Sandokan), René en alle andere (oud)collega's bedanken voor de prettige sfeer in het Ornsteinlaboratorium.

Mijn (recentelijk aangewonnen) familie wil ik bedanken voor de interesse en de belangstelling; ik heb mijn best gedaan om de samenvatting leesbaar te maken. Na een feest komt altijd nog een feest!!

En tot slot bedank ik natuurlijk Liesbeth. Het leven met jou in sneltreinvaart is een intens avontuur. Ik hoop dat we voor ons 65^{ste} de overige 174 landen bezocht hebben!!

Curriculum Vitae

De auteur van dit proefschrift werd op 18 december 1972 geboren te Kaatsheuvel. Het VWO diploma werd in juni 1991 behaald aan het Dr. Möllercollege te Waalwijk.

In augustus 1991 begon hij aan de studie Scheikunde aan de Universiteit Utrecht en in augustus 1996 werd het doctoraal diploma behaald. Tijdens de doctoraalfase werden bijvakken bij de secties Moleculaire Massaspectrometrie (Prof. dr. Haverkamp, Universiteit Utrecht) en Anorganische Chemie (Prof. Geus, Universiteit Utrecht) verricht. Het afstudeeronderzoek werd uitgevoerd bij de sectie Gecondenseerde Materie onder begeleiding van Prof. dr. J.J. Kelly. Tijdens zijn studie was hij actief als bestuurs- en commissielid van de studievereniging van de Faculteit Scheikunde, U.S.S. Proton.

September 1996 trad de auteur als assistent in opleiding in dienst van de Universiteit Utrecht bij de sectie Gecondenseerde Materie. De meeste resultaten van het onderzoek zijn beschreven in dit proefschrift. Tijdens het promotieonderzoek werd een bijdrage aan het onderwijs geleverd door het begeleiden van practica voor eerste-, tweede- en derdejaars studenten. Tevens is de auteur is twee jaar lid geweest van de Debye AiO commissie.

Tijdens het promotieonderzoek werden de volgende conferenties bezocht: 'The Joint International Meeting of the Electrochemical Society and the International Society of Electrochemistry' in Parijs (Frankrijk) in augustus 1997, 'The 194th Meeting of the Electrochemical Society' in Boston (Verenigde Staten) in november 1998, en 'The European Materials Research Society Conference' in Straatsburg (Frankrijk) in juni 1999. Per 1 oktober 2000 treedt de auteur in dienst van het Philips Natuurkundig Laboratorium te Eindhoven.